Generation and applications of carrier-envelope phase stable mid-infrared femtosecond pulses at high repetition rates

Marcel Neuhaus

München 2022

Generation and applications of carrier-envelope phase stable mid-infrared femtosecond pulses at high repetition rates

Marcel Neuhaus

Dissertation
an der Fakultät für Physik
der Ludwig–Maximilians–Universität
München

vorgelegt von
Marcel Neuhaus
aus Berlin

München, den 01.07.2022

Gutachter: Prof. Matthias Kling
Zweitgutachter: Prof. Emiliano Cortés
Tag der mündlichen Prüfung: 11.08.2022

Contents

List of Figures

Abstract

Parametric processes can be used to amplify broadband spectra as well as shift their frequency range. Optical parametric chirped pulse amplification (OPCPA) systems are used in the generation of broadband femtosecond pulses with high intensities over many frequency ranges. In the mid-infrared, a region where classical mode-locked laser systems are not as easily available, they offer the chance to generate broadband carrier-envelope phase-stable pulses. This allows to make use of the advantages of the mid-infrared range for applications from strong-field physics to time-resolved spectroscopy.

In this thesis, for both of these applications, OPCPA systems are developed and their usefulness is demonstrated by studying ultrafast carrier dynamics in semiconductors.

One demonstrated system generates high average power in the 10 W range with sub-three cycle pulses around 2 μm at a repetition rate of 100 kHz. This enables studies in a previously less accessible frequency range with high intensity and with good statistics over short measurement times. Among other strong-field experiments, it was used to study high harmonic generation from silicon under ambient conditions.

Another system was developed to measure the field-resolved changes to the dielectric properties of materials following an ultrashort pump excitation. This expands such experiments to higher, previously unobtainable THz probe frequencies (up to 100 THz). The laser system combines octave spanning field-resolved spectroscopy from 3 to 6 μm with a sub-10 fs temporal resolution, 2 MHz repetition rate, and a high dynamic range. These capabilities are demonstrated on studies on photoexcited carrier dynamics in gallium arsenide and germanium. The field-resolved measurement proved useful to reveal scattering dynamics and the previously often neglected initial thermalization dynamics. The high pump intensity permitted studying these materials under strong excitation conditions which allowed to investigate the saturation of the scattering rate with intensity.

The work presented in this thesis demonstrates that mid-infrared OPCPA systems are a flexible tool for many scientific applications and can be used to gain new insides into even extensively investigated materials such as bulk semiconductors.

Kurzzusammenfassung

Parametrische Prozesse können benutzt werden, um breitbandige Spektren zu verstärken sowie ihren Frequenzbereich zu verschieben. Optisch-parametrische gechirpte Pulsverstärker (engl. optical parametric chirped pulse amplifier: OPCPA) Systeme werden dazu benutzt, breitbandige Femtosekundenpulse mit hohen Intensitäten in vielerlei Frequenzbereichen zu erzeugen. Im mittleren Infraroten, einer Region wo klassische modengekoppelte Lasersysteme schlechter verfügbar sind, erlauben sie es, breitbandige Pulse mit stabiler Träger-Einhüllendenphase zu erzeugen. Dies ermöglicht, die Vorteile des mittleren Infraroten Frequenzbereiches für Anwendungen von Starkfeldphysik bis zur zeitaufgelösten Spektroskopie zu nutzen.

In dieser Doktorarbeit wurden für diese beiden Anwendungen OPCPA Systeme entwickelt und ihre Nützlichkeit dadurch demonstriet, dass ultra-schnelle Ladungsträgerdynamiken in Halbleitern untersucht wurden.

Eines der entwickelten Lasersystem erzeugt Pulse mit hoher Durchschnittsleistung im 10 W Bereich mit weniger als drei optischen Zyklen um 2 μm mit einer Wiederholrate von 100 kHz. Dies erlaubt es, Experimente in einem vorher wenig zugänglichen Frequenzbereich mit hohen Intensitäten und guter Statistik bei kurzer Messzeiten durchzuführen. Das Lasersystem wurde für Starkfeldexperimente eingesetzt, inklusive der Erzeugung hoher Harmonischer in Silizium.

Ein weiteres Lasersystem wurde entwickelt, um feldaufgelöst Änderungen der dielektrischen Materialeigenschaften durch einen ultraschnellen Anregungspuls zu messen. Dieses System erweitert solche Experimente zu höheren, vorher unerreichten THz Abtastfrequenzen. Es kombiniert ein oktavenbreites Spektrum von 3 bis 6 μm mit einer zeitlichen Auflösung unter 10 fs sowie einem hohen Dynamikbereich. Diese Vorzüge werden an Messungen von photonenangeregten Ladungsträgern in Germanium und Galliumarsenid demonstiert. Die feldaufgelösten Messungen waren dabei hilfreich, um Streudynamiken und die oft vernachlässigte anfängliche Ladungsträgerthermalisierung zu enthüllen. Die hohe Pumpintensität erlaubte es, Sättigungseffekte der Streurate zu beobachten.

In dieser Arbeit wird gezeigt, dass OPCPA Systeme im mittlern Infrarot ein vielseitiges Werkzeug sind, dass in vielen wissenschaftlichen Anwendungsgebieten neue Erkenntnisse liefern kann, selbst in hinreichlich untersuchten Materialien wie in kristallinen Halbleitern.

Chapter 1

Introduction

Ultrafast laser spectroscopy allows to study materials on the shortest time scales as well as under high intensity conditions. While in previous decades ultrafast spectroscopy often has been performed in the visible to near-infrared (NIR), for both of these applications longer wavelengths in the MIR can be highly beneficial.

For strong field applications the ponderomotive energy of excited electrons scales with the laser intensity but also with the wavelength squared $E_p \propto I \cdot \lambda^2$. The ponderomotive energy in both the generation of high harmonics as well as in electron spectroscopy is proportional to the cut-off energy [1, 2]. Often the intensity cannot be increased arbitrarily, as this can lead to damage in solids or to detrimental plasma generation in gases. For example, in high harmonic generation (HHG) in gases the intensity can lead to the generation of plasma that is highly detrimental to the phase matching and therefore prohibits efficient conversion. An increase in wavelength can permit an increase in ponderomotive energy and therefore push these processes into higher energy ranges.

For time-resolved applications MIR and terahertz fields can be beneficial as these fields can be sampled directly by electro-optical sampling (EOS) [3–5]. This is possible due to the waveform stable fields commonly achieved in this spectral range. While field-resolved detection can also be achieved in attosecond metrology [6], these setups require complex vacuum systems. While attosecond systems offer excellent temporal resolution, the ionizing nature of the attosecond XUV pulses can induce changes in the sample [7]. Detection methods therefore often rely on electron spectroscopy, where the maximal number of detected particles can be limited by space charge effects and thereby also limit the achievable statistics. For long wavelengths MIR to THz pulses the excitation energy is mostly below the band gap and the probe does not affect the target and also offers access to a different energy regime to study processes such as interband dynamics in semiconductors or vibrational modes in bio-medical samples[8].

While this type of field-resolved spectroscopy has traditionally been performed at lower frequencies in the THz domain [9, 10], the long cycle duration of the THz-transients can be limiting for the temporal resolution. Shorter wavelengths in the MIR do therefore not just open the window to a new frequency range, but also allow to increase the temporal resolution of these kinds of measurements. The other advantage of longer wavelength

systems is that the photon energy is typically far away from electronic transitions in the samples. This is important to investigate off-resonant strong field excitation. For strong-field effects, two-photon absorption from visible wavelengths might be above the bandgap in many semiconductors and can therefore lead to damage of the sample.

While in the visible and NIR range different mode-locked laser sources exist, for the longer wavelengths in recent years ultrafast thulium and holmium based systems have seen significant advancements. These systems operate at around 1.95 and 2.1 μm and can now achieve 100 W power level and approaching the mJ level pulse energies [11]. While commonly sub 100 fs pulses are achievable by these systems, the amplification bandwidth limits the pulse duration so that the few cycle regime is still not easily reached. To achieve shorter pulse durations, these systems employ spectral broadening. Often this is done in gas-filled hollow-core fibers (HCF). The thus obtained pulse duration is however often longer than 40 fs or around 6 optical cycles [12]. Continuing this process often proves to be challenging as the temporal compression required between any broadening stage can only compensate for lower order spectral phase components which are not exceedingly complex. Higher order phases or phase ripples can often prove to hinder further spectral broadening.

To achieve few-cycle MIR pulses with high pulse energy, systems that rely on optical parametric chirped pulse amplification (OPCPA) are therefore still the method of choice [13, 14]. In these systems, non-linear optical phenomena are used to generate a broadband seed, converting the frequency to the desired range. Finally, the so generated broadband MIR-pulses can be amplified by one or more optical parametric amplification (OPA) stage [15]. Additionally, if CEP stability is required in NIR systems, these systems have typically to rely on active stabilisation which, although commercially available, increases the technical complexity of these systems. MIR pulses generated by a DFG process in an OPCPA can be passively CEP-stable as a beneficial side-effect without further effort.

OPCPA systems offer a range of additional benefits. They can not only reach spectral regions where no laser material is available [16]. The process can also be tuned with relative ease to different spectral windows as well as bandwidths or shape of the spectrum, which can be a crucial benefit in some experiments. This is also important for the difference frequency used to generate the MIR radiation as this allows to shape the generating spectrum to have intensity at the edges of the spectrum that contribute to the frequency mixing, unlike in spectrally broadened systems in which the spectrum is often peaked around the fundamental in the middle of the spectrum which does not contribute to this process.

OPA systems can also operate at different repetition rates that are just limited by the available lasers. As amplified laser sources do not require a cavity they are available at any repetition rate below the oscillator repetition rate. This is important for experiments on solid state targets, where the intensity is limited by the damage threshold of the material. On the other side the laser intensity and fluence needs to be sufficient to drive the non-linear processes or to excite sufficient number of carriers. Oscillators at multiple tens to hundred MHz are mostly not capable of reaching the necessary pulse energy and intensity to drive OPCPA systems with μJ-level output. On the other hand, traditional amplified Ti:Sa systems that are operating below 10 kHz suffer from a reduced statistics which necessitates long measurement times over which laser parameters are more challenging to keep stable.

Different high power narrow band laser systems based on Yb:YAG or Ytterbium fibers are nowadays commercially available with multiple 100 W output powers and repetition rate in the 0.1-10 MHz range [17–19]. These systems are ideal to drive high intensity OPCPA systems that achieve broadband μJ-level pulses.

In this thesis I will demonstrate OPCPA based laser systems in the lower MIR-range for strong-field as well as for time- and field-resolved spectroscopy. I will then also show how these lasers can be utilized in experimental setups and discuss some of the new insides these systems have generated in semiconductors.

I will first discuss the fundamentals of optical parametric amplification systems. In chapter 2 the theory behind OPCPA systems are discussed. The physics of second order optical parametric processes and especially difference frequency generation and its application in optical parametric amplification is explained.

This allows to discuss the different elements of OPCPA systems and the conversion of a narrow-band pump into a broadband OPA seed pulse by supercontinuum generation in bulk crystals in chapter 3.

The first OPCPA system presented in chapter 4 is a high average power OPCPA system generating carrier envelope stable pulses around 2 μm. Special focus is then given to challenges associated with the high average power of the system especially in regards to selection of the non-linear crystal in the power amplification OPA. An experiment performed with this system is presented in which high harmonic are generated from silicon. The influence of different intensities, ellipticity and crystal orientation is studied.

The next parts of the thesis are concerned with measuring fast photo-induced dielectric changes over the octave spanning spectral range of $3 - 6\,\mu$m. In chapter 5 the NIR-OPCPA system used as MIR driver, sample pump and EOS gate is presented. The use of these pulses in a field-sensitive transient reflectometry pump-probe setup and associated techniques and improvements are discussed.

In chapter 6 measurements on highly excited direct and indirect semiconductor on the examples of GaAs and Ge are discussed.

Finally, I will summarize the findings of the previous chapter in chapter 7 and give an outlook on further development of MIR-OPA systems.

Afterwards, in Appendix A, I will shortly discuss a microscopy setup using the NOPA laser from Chap. 5 and show some results from biological microscopy in studying the metabolism of irradiated cancer and fibroblast cells.

Publications

- Neuhaus, M., Fuest, H., Seeger, M., Schötz, J., Trubetskov, M., Rusbueldt, P., Hoffmann, H., Riedle, E., Major, Z., Pervak, V., Kling, M. F. , and Wnuk, P. "10 W CEP-stable few-cycle source at 2 μm with 100 kHz repetition rate". *Opt. Exp.* 26, 16074–16085. (2018)

- Neuhaus, M., Schötz, J., Aulich, M., Srivastava, A., Kimbaras, D., Smejkal, V.,

Pervak, V., Alharbi, M., Azzeer, A. M., Libisch, F., Lemell, C., Burgdörfer, J., Wang, Z. , and Kling, M.F ,Transient field-resolved reflectometry at 50–100 THz. *Optica* 9, 42–49 (2022)

- Wnuk, P., Fuest, H., Neuhaus, M., Loetscher, L., Zherebtsov, S., Riedle, E., Major, Z., and Kling, M. F. Discrete dispersion scanning as a simple method for broadband femtosecond pulse characterization. *Optics Express* 24, 18551–18558 (2016).

- Schötz, J., Mitra, S., Fuest, H., Neuhaus, M., Okell, W. A., Förster, M., Paschen, T., Ciappina, M. F., Yanagisawa, H., Wnuk, P., Hommelhoff, P., and Kling, M. F. "Nonadiabatic ponderomotive effects in photoemission from nanotips in intense midinfrared laser fields". *Phys. Rev. A* 97, (2018).

- Kubullek, M., Wang, Z., von der Brelje, K., Zimin, D., Rosenberger, P., Schötz, J., Neuhaus, M., Sederberg, S., Staudte, A., Karpowicz, N., Kling, M. F., and Bergues, B. "Single-shot carrier–envelope-phase measurement in ambient air". *Optica* 7, 35–39, (2020).

- Barbiero, G., Wang, H., Graßl, M., Gröbmeyer, S., Kimbaras, D., Neuhaus, M., Pervak, V., Nubbemeyer, T., Fattahi, H. , and Kling, M. F. Efficient nonlinear compression of a thin-disk oscillator to 8.5 fs at 55 W average power. Optics Letters 46, 5304–5307, (2021).

- Saleh, A., Li, W., Alqahtani, H., Neuhaus, M., Alshehri, A., Bergues, B., Alharbi, M., Kling, M. F., Azzeer, A. M., Wang, Z. and Alharbi, A. F. Fifth-order nonlinear optical response of Alq3 thin films. *Results in Physics* 37, 105513, (2022)

- Zhang, W., Dagar, R., Rosenberger, P., Sousa-Castillo, A., Neuhaus, M., Li, W., Khan, S. A., Alnaser, A. S., Cortes, E., Maier, S. A., Costa-Vera, C., Kling, M. F., and Bergues, B. "All-optical nanoscopic spatial control of molecular reaction yields on nanoparticles". *Optica* 9, 551–560 (2022)

- Rosenberger, P., Ritika, D., Zhang, W., Sousa-Castillo, A., Neuhaus, M., Cortes, E., Maier, S., Costa-Vera, C., Alharbi, M., Kling, M. F., and Bergues, B. "Imaging elliptically polarized infrared near-fields on nanoparticles by strong-field dissociation of functional surface groups". *The European Physical Journal D* 76, 109 (2022)

Chapter 2

Optical Parametric Amplification Theory

The underlying theory of OPAs has been known for some decades and studied in more detail than it would be feasible to describe here [20–22]. The purpose of this chapter is to focus on the essential results and their practical meaning. Besides laying down a theoretical groundwork for the reader to understand the following chapters it is mainly to provide easy to understand insights into the design criteria for building OPA and DFG based systems. The emphasis is given on the systems with a broad bandwidth in the few-cycle regime. The purpose here should not be to just provide the essential formulas but also to fill them with meaning by providing the reader with numerical values as these are often helpful to gain a better understanding on the magnitude of effects and to differentiate between different regimes.

First, a general introduction to second-order nonlinear processes is given and necessary conditions such as phasematching are explained. Then the governing equation for parametric amplification and their influence on the small gain are discussed. The next section will then focus on how to maximize the amplification bandwidth before discussing the effects on saturation. Then the temporal and spatial effects are discussed before finally discussing the effects of the pump beam on the amplified beam.

2.1 Field mixing

Optical parametric processes are defined by their property that the initial state and final state of the atomic system are the same. Therefore, no energy is transferred to the atomic system and no heat is deposited in the crystal. Optical nonlinearity arises from the fact that the separation in the lattice is not parabolic but rather the resulting polarisation in the material must be expressed as a power series of the electric field:

$$P = \epsilon_0 \chi_i^{(1)} E_i + \epsilon_0 \chi_{ij}^{(2)} E_i \cdot E_j + \chi_{ijk}^{(3)} E_i \cdot E_j \cdot E_k + ... \tag{2.1}$$

The χ^n are the (nonlinear) susceptibilities and depend on the crystal and the electric field polarisation The terms of at least quadratic order are refered to as nonlinear polarization

P^{NL}. This results in a modified version of the propagation equation:

$$\frac{\partial^2 E}{\partial z^2} - \frac{\partial^2 E}{\partial t^2} = \frac{1}{\epsilon_0 c^2}\frac{\partial^2 P^{NL}}{\partial t^2} \tag{2.2}$$

The nonlinear polarisation then serves as a source of newly generated light.

For OPAs we need only understand lowest nonlinear expansion order which corresponds to second order processes that can be expressed as

$$P^{(2)} = \epsilon_0 \chi^{(2)} \frac{1}{2} E_1 \cdot E_2. \tag{2.3}$$

We can insert the real electric fields $E_1 = A_1 cos(k_1 x - \omega_1 t + \phi_1)$ and $E_2 = A_2 cos(k_2 x - \omega_2 t + \phi_2)$ with the angular frequency ω and the magnitude of the wave vector $k = |\vec{k}|$. Using the addition theorem $cos(x)cos(y) = \frac{1}{2}cos(x-y) - cos(x+y)$ we gain:

$$\begin{aligned} P = &\frac{1}{4}\epsilon_0 \chi^{(2)}\left(\omega_1, \omega_2, \omega_1 \pm \omega_2\right) A_1 A_2 \Big[\\ &\underbrace{cos\Big((k_1 - k_2)x - (\omega_1 - \omega_2)t + (\phi_1 - \phi_2)\Big)}_{DFG} \\ &- \underbrace{cos\Big((k_1 + k_2)x - (\omega_1 + \omega_2)t + (\phi_1 + \phi_2)\Big)}_{SFG} \Big] \end{aligned} \tag{2.4}$$

The second cosine expression represents sum frequency generation (SFG). When $\omega_1 = \omega_2$ it corresponds to the important special case of second harmonic generation (SHG). The other case corresponds to the difference frequency generation (DFG), which we will focus on as it also explains the OPA. The higher frequency component $\omega_1 = \omega_p$ is called the pump and the lower component $\omega_2 = \omega_s$ is called the signal. The resulting difference frequency $\omega_i = \omega_p - \omega_s$ is also called the idler in analogy to electric amplifiers. Due to energy conservation the remaining energy must be transferred into a signal photon. Hence, the process amplifies the signal. The simplest way to visualise the OPA process is as a photon splitter. A pump photon is transformed (i.e. split) into two photons with lower frequency as can be seen in Fig. 2.1 (a). In the following the main questions to answer are, how the photon energy is distributed after the splitting and what the efficiency of the OPA process is.

2.1.1 Phase matching

To answer the first question we can move to a reference frame that is co-moving with the phase velocity of the idler and therefore have to subtract the phase $k_i x - \omega_i t$. We then see that the newly generated components move out of phase with the idler with the frequency mismatch

$$\Delta\omega = \omega_p - \omega_s - \omega_i \tag{2.5}$$

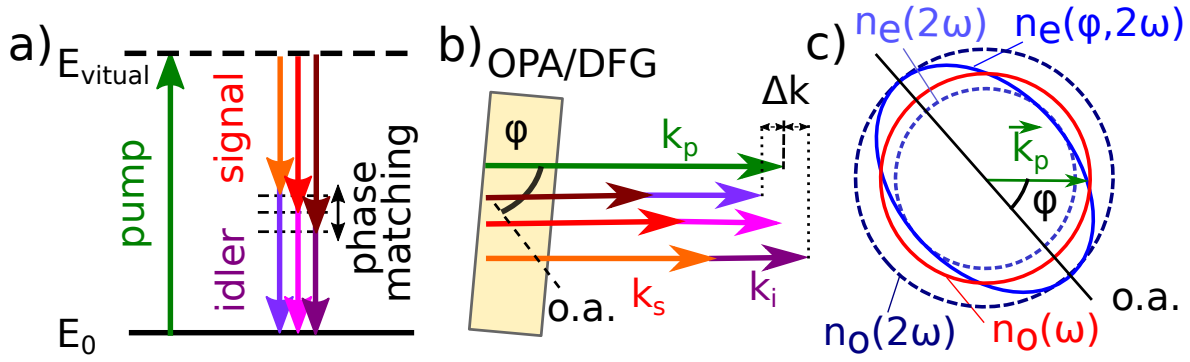

Figure 2.1: Working principle of an OPA. a) Energy picture showing how a pump photon is split into a signal and idler photon. b) Wave-vector matching in an OPA/DFG. c) Critical phasematching in a degenerate OPA. The crystal must be rotated in a way, so that the resulting phasematching angle ϕ between optical axis (o.a.) and the pump propagation $\vec{k_p}$ is such, that the refractive index of the pump (blue) $n_e(\phi, 2\omega)$ is the same as the refractive index of seed and idler $n_0(\omega)$ (red).

and the wave-vector mismatch

$$\Delta k = k_p - k_s - k_i. \tag{2.6}$$

that is shown in Fig. 2.1 (b). Once the newly generated components are out of phase with the initially generated components by about $\Delta\phi = \pi$ they would interfere destructively and therefore lead to a decrease of effective amplification. We can deduce the helpful condition $L \cdot \Delta k < \pi$ for the crystal length L. This is analogous to a photon picture, where we obtain from the Heisenberg uncertainty principle $\Delta x \cdot \Delta p = L \cdot \Delta k \hbar < \pi\hbar$.The uncertainty in frequency is often ignored in this discussion since the time needed to pass through a roughly mm thick crystal is in the $10^{-11}s$ range and the resulting frequency mismatch can be neglected in comparisson to optical frequencies in the $10^{14}Hz$ range.

We also see from Eq. 2.4 that the phase term of the idler is given by

$$\phi_i = \phi_p - \phi_s + \left(\frac{\pi}{2}\right) \tag{2.7}$$

which is important for passive CEP stabilisation as we will discuss later. The extra $\frac{\pi}{2}$ comes out from a more detailed treatment than is presented here but has little influence in practice and can be disregarded for the following discussion.

2.1.2 Birefringent crystals

As the wave vector k is given by

$$k = n\frac{2\pi}{\lambda} \tag{2.8}$$

and in normally dispersive media the refractive index is increasing in frequency or $n(\omega_p) > n(\omega_s, i)$, in thick isotropic crystals, the phase-matching condition cannot be achieved.

The most common solution is to overcome this problem is by using so called critical phase matching in birefringent crystals. In these crystals the refractive index for different directions is slightly different.

In so called uniaxial crystals the refractive index in one direction varies from the two other ones. This direction is called the optical axis. Beams that are partially polarized along this axis are called extraordinary (e-polarized) while beams that are polarized perpendicular to it are called ordinary (o-polarized). The extraordinary refractive index of a partially along e-polarized beam can then be calculated by

$$n = \left(\left(\frac{cos(\phi)}{n_o} \right)^2 + \left(\frac{sin(\phi)}{n_o} \right)^2 \right)^{-\frac{1}{2}} \tag{2.9}$$

where $n_e = n_e(\phi = 0°)$ and ϕ is the phase matching angle or the angle between the pump k-vector k_p and the optical axis as can be seen in Fig. 2.1 (b) and (c).

In most commonly used crystals the extraordinary refractive index is smaller ($n_e(\omega) < n_o(\omega)$), which are then referred to as negative uniaxial crystals. To compensate for the higher refractive index, the highest frequencies involved in the conversion process (typically the pump in a DFG/OPA or the sum frequency) are e-polarized. If the other two components, e.g. signal and idler, are both o-polarized this is called type 1 phase-matching. In type 2 either idler or signal are also e-polarized but this configuration is not used within this work and we will therefore focus on type 1 in the following.

2.2 Manley-Rowe Equation

The main equations governing the evolution of the three relevant fields of pump, signal and idler are the Manley Rowe equations which are given by [20]:

$$\frac{\partial A_p}{\partial z} = -i \frac{\omega_p d_{eff}}{n_p c} A_i A_s e^{i\Delta k z} \tag{2.10}$$

$$\frac{\partial A_s}{\partial z} = -i \frac{\omega_s d_{eff}}{n_s c} A_i^* A_p e^{-i\Delta k z} \tag{2.11}$$

$$\frac{\partial A_i}{\partial z} = -i \frac{\omega_i d_{eff}}{n_i c} A_s^* A_p e^{-i\Delta k z} \tag{2.12}$$

z describes the propagation in the crystal and d_{eff} is the effective nonlinearity of the crystal. How d_{eff} is obtained depends on the symmetry group of the crystal. We can see that the equations 2.11 and 2.12 governing the change in seed and idler are symmetrical. Indeed, the only difference between the two in an OPA is that the seed is provided with a

certain initial field, while the idler is amplified from vacuum fluctuations. If additionally no signal field is provided to seed the process, this is referred to as optical parametric oscillator (OPO). These sources are often used in a cavity and are used to produce more narrow-band sources with wavelengths that are tunable over a wide range. These pulses are temporally synchronised to the source which is used as a pump but have no fixed phase relation to the pump as both signal and idler phase are not fixed by a seed.

2.2.1 Passive CEP stabilisation

An important factor in the DFG is the previously mentioned phase relationship in Eq. 2.7. This can be used in what is called passive CEP stabilisation. The phase of a pulse is given by $\phi = (kx - \omega t + \Delta\phi + \phi_{CEP})$ where $\Delta\phi$ represents the constant phase off-set of each pulse and ϕ_{CEP} is the carrier envelope frequency. If one uses two pulses originating from the same source with the same ϕ_{CEP}, the carrier envelope frequency of the pulses cancel each other out. As for nonlinar processes the phase is multiplied by the order of the nonlinear process as can be seen in Eq. 2.4. For example, the CEP of the second harmonic is doubled $\phi_{CEP,SHG} = 2 \cdot \phi_{CEP}$. Therefore, for the CEP cancellation to occur, both pulses must be of the same harmonic order, e.a. if one of the pulses was frequency doubled or originated from a DFG, the other pulse must do so as well.

2.3 Small gain

Under the assumption that the gain $G = I_s(L)/I_s(0)$ of the seed intensity I_s is small, one can derive a simple formula for the gain. This is assuming that the pump power is not significantly depleted and that therefore the pump intensity $dA_p/dz = 0$ is unchanged. It can be shown that after an interaction or crystal length of L (typically the crystal length, unless it is limited by temporal or spatial walk-off as we will discuss later in section 2.7), this leads to a gain of

$$G = \frac{I_s(L)}{I_s(0)} \approx 1 + \frac{\Gamma^2}{g^2} sinh^2(gL) = \frac{\Gamma^2}{g^2} exp(2gL) \tag{2.13}$$

with the gain coefficient

$$g = \sqrt{\Gamma^2 - \left(\frac{\Delta k}{2}\right)^2} \tag{2.14}$$

and the nonlinear coefficient

$$\Gamma^2 = \frac{8\pi^2}{\epsilon_0 c} \frac{d_{eff}^2}{n_p n_s n_i} \frac{I_p}{\lambda_i \lambda_s}. \tag{2.15}$$

The second fraction denotes the part that depends on the crystal. As the dispersion is small, especially for phase-matched processes, we have $n \approx n_s \approx n_i \approx n_p$. Instead of comparing crystals by effective non-linearity, it is better to use $d_{eff}/n^{3/2}$ instead. Often

crystals with a higher d_{eff} also have a higher refractive index, such as many crystals used in the MIR, so that the refractive index partially mitigates the higher non-linearity. Typically values for Γ are in the $1/mm$ range, e.g to amplify a seed around $800\,nm$ in a BBO pumped by a $515\,nm$ beam with an intensity of $60\,GW/cm^2$ we obtain $\Gamma = 3.7/mm$.

Due to the inverse wavelength dependence of the crystal-independent part $\frac{I_p}{\lambda_i \lambda_s} \propto I_p \omega_s(\omega_p - \omega_s)$ the process typically becomes less efficient for longer wavelengths, but is most efficient at the point of degeneracy as the condition for the maximum $\frac{d}{d\omega_s}\omega_s(\omega_p - \omega_s) = 0$ directly leads to the degeneracy definition of $\omega_s = \frac{1}{2}\omega_p$.

A higher intensity also increases the first term of Eq. 2.14 compared to Δk. Therefore, using higher intensities can lead to broader amplification spectra. It is therefore important to understand the limitation of the pump intensity as it is not only limited by the damage threshold of the crystal as well as the crystal coating. As the damage threshold of crystals increases with shorter pulses (scaling as $I_{damage} \propto \frac{1}{\sqrt{t_p}}$ for avalanche ionization damage, which is however strictly speaking not valid anymore in the sub-picosecond range [23]), crystals can often withstand quite high intensities for (sub-)picosecond pulses. The pump intensity in an OPAs can also be limited by the nonlinear phase represented by the B-integral:

$$B = \frac{2\pi}{\lambda} \int_0^L n_2 I(x, y, t)\, dx. \tag{2.16}$$

This can under realistic condition reach values around unity (e.g in a $4\,mm$ long BBO with $5 \cdot 10^{-20} \frac{m^2}{W}$ and $I = 100\,\frac{GW}{cm^2}$ we obtain $B = 1.2\,rad$). Besides destroying the beam quality of all involved beams as they temporally overlap with the intense pump beam, the spatially dependent phase also affects the phase matching. As the effect is more pronounced in the center of the beam, where the intensity is higher, it cannot easily be compensated for by e.g. adjusting the phase matching angle and should therefore be kept below about unity. The intensity should therefore typically be kept to values below $100\,\frac{GW}{cm^2}$, especially for thicker crystals.

The scaling of this nonlinear phase with increased intensity given by $L \cdot I_p$ is stronger then in the exponent of the gain with $L \cdot \sqrt{I_p}$ when comparing it with the crystal length L. In order to keep the B-integral low and achieve sufficient gain, it is therefore better to use longer crystals instead of higher intensities. This is however limited by the phase-mismatch where we have seen the opposite is required for broadband, amplification e.g. using shorter crystals and higher intensities.

2.4 Broadband amplification

To achieve a broad amplification Δk should be small over a large bandwidth. Taylor expanding $\Delta k = k_p - k_s - k_i$ with respect to signal frequency reads

$$\Delta k = \Delta\omega \left.\frac{\partial \Delta k}{\partial \omega_s}\right|_{\omega_0} + \frac{1}{2}(\Delta\omega)^2 \left.\frac{\partial^2 \Delta k}{\partial \omega_s^2}\right|_{\omega_0} + \frac{1}{6}(\Delta\omega)^3 \left.\frac{\partial^3 \Delta k}{\partial \omega_s^3}\right|_{\omega_0} + ... \tag{2.17}$$

where $\Delta\omega = \omega_s - \omega_0$ is the deviation from the center frequency ω_0. We will now discuss the different orders of expansion coefficients $\frac{\partial^n \Delta k}{\partial \omega^n}|_{\omega_0}$. We will limit the discussion here to case where the spectral range of pump laser is narrow. Then we can assume that k_p and ω_p are independent of the signal frequency and therefore $\partial^n k_p / d\omega_s^n = 0$ and $d^n w_p / dw_s^n = 0$. Using this, we can see from energy conservation $w_s = w_p - w_i$ that $\partial/\partial w_s = -\partial/\partial w_i$. [15].

The linear term then becomes

$$\frac{\partial \Delta k}{\partial \omega_s} = \frac{\partial k_p}{\partial \omega_s} - \frac{\partial k_s}{\partial \omega_s} - \frac{\partial k_i}{\partial \omega_s} = -\frac{\partial k_s}{\partial \omega_s} + \frac{\partial k_i}{\partial \omega_s} = \frac{1}{v_{g,i}} - \frac{1}{v_{g,s}} \tag{2.18}$$

The pump only enters these considerations insofar as it determines the idler frequency, the dispersion at the pump wavelength is therefore not affecting the amplified bandwidth. This also shows that for broadband amplification the group velocity v_g of the signal at the center frequency $v_g(\omega_0)$ and the idler at $v_g(\omega_i = \omega_p - \omega_0)$ need to be identical. There are different ways to achieve this which we will discuss in the following.

2.4.1 Degenerate OPA

The most straight forward way for the degenerate case involves $\omega_s = \omega_i$. As the signal and idler frequencies are identical, the condition is then trivially fulfilled. Due to the previously mentioned wavelength dependence in the OPA, under this condition the highest gain is also achieved. Therefore even if additional methods are used to minimize the group velocity mismatch, operating an OPA at least close to the degeneracy point is often beneficial. As the seed or idler wavelength are often determined by the target parameters, one way to achieve this condition is to choose an appropriate pump source.

2.4.2 Zero crossing point

Another option can be used for signal and idler wavelengths at opposite sides of the zero dispersion point [15]. This means that $v_g = \partial\omega/\partial k$ has a maximum and therefore the group velocity starts do decrease on both sides. There are then pairs of signal and idler wavelengths on opposite sides of the zero dispersion point that have the same group velocity typically requiring that the pump has about twice the frequency of the zero dispersion frequency. For BBO for example, it is at $1488\,nm$ which means that for pump wavelengths around $744\,nm$ broad amplification can be achieved.

2.4.3 NOPA

If these options are not available due to the combination of available pump wavelength and required amplification spectrum the so-called noncollinear OPA or NOPA can be used as a flexible way to achieve the necessary spectral bandwidth. By introducing a noncollinear angle α between pump and seed beam one introduces an additional degree of freedom to phase match a broader spectrum. The phasematching angle ϕ is in this case defined as the angle between the optical axis and the pump wave vector. By this technique the

projection of the group velocity of the idler and signal beam can be adjusted so that it is equal and therefore fulfill Eq. 2.18. As the idler is amplified from virtual photons it will automatically have an angle $\alpha_i = -\frac{\lambda_i}{\lambda_s} * \alpha_s$ due to momentum conservation. As we can see, for a broadband spectrum the idler is emitted with a severe angular dispersion and is therefore typically not usable. The phase matching angle for a given amplified center frequency thereby becomes larger. In negative uniaxial crystals, increasing the noncollinear angle also leads to an increase in the signal center-wavelength as well as a required increase in the phase-matching angle.

2.5 Higher order dispersion

After one of the techniques just mentioned has been used to reduce the first order term of Eq. 2.18, it is necessary for broadband amplification to understand the next order terms to achieve the broadest possible amplification spectrum. The effects of the different Taylor orders can be seen in Fig. 2.2 (a), where they are shown together with the resulting small gain spectra (b) and the resulting temporal profile of the Fourier- limited pulses (c).

Similarly to Eq. 2.18, the second derivative in the Taylor expansion is given by

$$\frac{\partial^2 \Delta k}{\partial \omega_s^2} = -\frac{\partial^2 k_p}{\partial \omega_s^2} + \frac{\partial^2 k_p}{\partial \omega_i^2} = \gamma_i - \gamma_s \tag{2.19}$$

.

Here we use the group velocity dispersion $\gamma = GVD = \frac{\partial^2 \Delta k}{\partial \omega^2}$. We can also define the difference in group velocity mismatch $\Delta\gamma = \gamma_i - \gamma_s$. The full second term can then be simplified to

$$\Delta k^{(2)} = \frac{1}{2}\Delta\gamma\, \Delta w^2 - k_0. \tag{2.20}$$

It should be noted that the group velocity missmatch $\Delta\gamma$ is on the order of $100\, fs^2/mm$ and therefore for few mm thick OPA crystals this term only becomes relevant for bandwidths in the $0.1\, PW$ range, corresponding to a Fourier-limit of about 10 fs . This emphasises why OPAs could be used to amplify bandwidth corresponding to few cycle pulses.

The minimal point of the parabola $\Delta k_0 = \Delta k(\omega_0)$ can be further adjusted by changing the phase matching angle. As $\Delta k \cdot L$ should be smaller then a certain $\phi_{max} \approx \pi$ the bandwidth is given by

$$\left(\Delta\gamma \cdot d\omega^2 - \Delta k_0\right) \cdot L < \phi_{max}. \tag{2.21}$$

If we first consider $\Delta k_0 = 0$ or the case where the maximum amplification is in the center of the spectrum, the resulting bandwidth is

$$2\Delta\omega_{max} = 2\sqrt{\frac{L}{\Delta\gamma \cdot \phi_{max}}}. \tag{2.22}$$

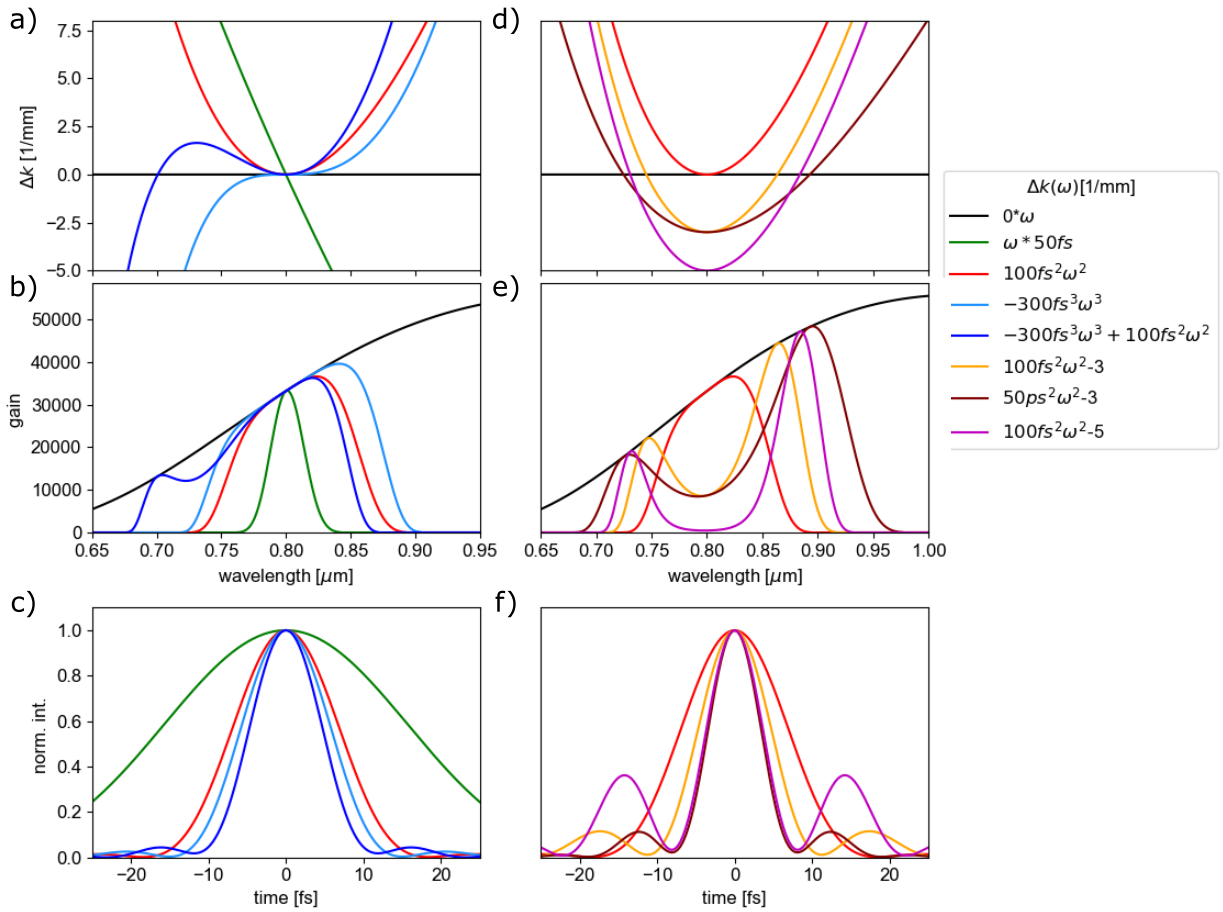

Figure 2.2: The influence of different $\Delta k(\lambda)$,the assosiated small gain ((b),(e)) and the resulting Fourier-limited temporal pulse shape (c),(f)).The example here is for an OPA $2\,mm$ thick crystal pumped by $515\,nm$ with an intensity of $60\,GW/cm^2$. a)-c) show the effect linear, quadratic and third order terms. d)-f) show the effect of shifting the phase matching. A deep dip can give a FWHM temporal profile of a lower dispersive crystal but at the cost of stronger side pulses (compare magenta vs. dark red).

The bandwidth is therefore dependent on$\sqrt{L}$ while the gain increases with e^L. A slightly thicker crystal can therefore lead to more absolute amplification at the edge of the amplification spectrum provided that saturation is not yet the limiting factor.

In practice it is often advantageous to tune Δk_0 so that the parabola crosses the zero line on two points as can be seen in Fig. 2.2 (d)-(f), where it can also be seen that this leads to a broader spectrum as

$$\Delta\gamma \cdot \Delta\omega^2 - \Delta k_0 < \phi_{max} \tag{2.23}$$

is fulfilled for a wider range. The center frequency ω_0 is then not amplified the strongest but only to a level determined by ϕ_{max}. This will regularly lead to a spectrum consisting of two humps as the amplification is strongest at the zero crossings as can be seen in the orange and purple curve in Fig. 2.2 (d) and (e). Indeed, if we would put $\Delta k_0 = -\phi_{max}$, e.g. have as much amplification in the middle as at the cut-off at the edge, the spectral bandwidth is then broader by a factor of $\sqrt{2}$. Although this might at first seem not that significant, achieving the same by a thinner crystal would lead to an $exp(-\sqrt{2}) = 1/4.1$ lower gain. The dip in the spectra results in a Fourier limited temporal profile with a main peak that has approximately the same duration as a spectrum without the dip but with increasd pre- and post-pulses as can be seen by comparing the dark red and purple temporal profiles in Fig. 2.2 (f). The minimum in the center is however often somewhat compensated for as the temporal Gaussian pump profile maximum overlap with the middle of a linearly chirped seed pulse and leads to a stronger amplification in the middle of the spectrum.

Finally, we should shortly discuss the third-order Taylor expansion term of Eq. 2.17, that is then given by

$$\Delta k^{(3)} = \frac{1}{6}(TOD_s - TOD_i)\Delta w_s^3 \tag{2.24}$$

with the third order dispersion $TOD = \frac{\partial^3 \Delta k}{\partial \omega^3}$. In the typically used transparent crystals, away from absorption the TOD is always positive and in many crystals often of similar magnitude so that the TOD of signal and idler at least partially cancels. In most cases it can be ignored. In some cases, it can lead to an additional zero crossing and can lead to an increased amplification bandwidth as can be seen in the dark blue curve in Fig. 2.2(a).

2.6 Saturation

From the small gain approximation we have seen that gain factors in the millions are achievable. In practice, this is however, mostly not the case. As soon as the seed reaches a sufficient level, pump depletion becomes relevant and Eq. 2.13 is no longer valid. A full treatment of the saturation becomes quite complex and basically impossible in the case of phase mismatch. For high gains and perfect phase matching, the transformed number of photons N_p to the number of seed photons N_s can be calculated as [22]:

$$N_s(z) = N_p \left(1 - sn^2\Big(N_p \frac{\omega_p d_{eff} E_p(0)}{cn}(z - z_0), \sqrt{\frac{N_p(0)}{N_p(0) + N_s(0)}}\Big)\right), \tag{2.25}$$

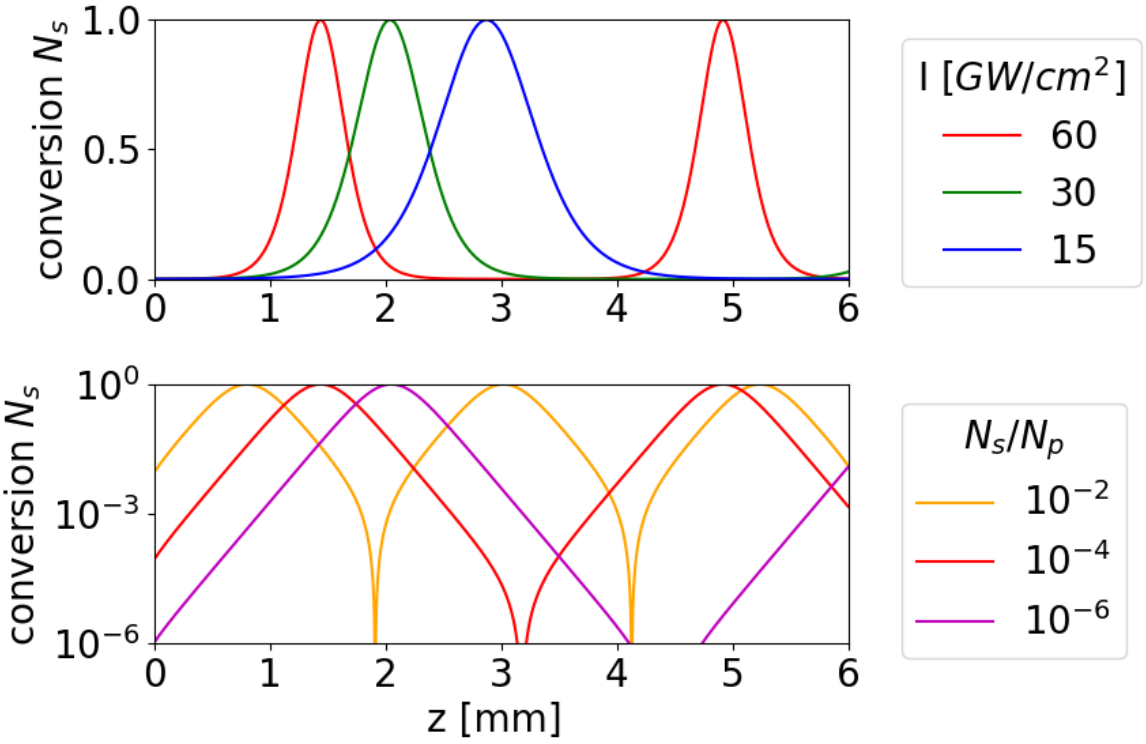

Figure 2.3: Saturation in a 1030nm pumped BBO crystal. The conversion efficiency according to Eq. 2.25 is plotted for a) different intensities and a starting ratio of $\frac{N_s}{N_p} = 10^{-4}$ and b) different initial seed photon numbers $\frac{N_s}{N_p}$ and a starting intensity of $60GW/cm^2$.

where $sn(\zeta, \kappa)$ is the sinusoidal Jacobi elliptic function. This function is a periodic function which means the process reverse after a certain distance. The factor z_0 is used to shift the function so that $N_s(0)$ matches the correct value and is mostly close to half a period. The $sn^2(\zeta, \kappa)$ function is similar to a $sin^2(\zeta)$ that is flattened at the top the more $\kappa \sim 1 - \frac{N_s}{2*N_p}$ approaches 1 such as for a seed that is much weaker compared to the pump, i.e. in a high gain stage. On the rising edge the function approaches a $tanh^2(\zeta)$ for $\kappa = 1$.

The full Eq. 2.25 leads to periodic peaks in conversion as shown in Fig. 2.3. From this equation it seems that a total transfer of power from the pump to seed and idler could be reached. That this is typically not observed in practice has many reasons. For one in a broad spectrum the condition of $\Delta k = 0$ can not be achieved for all wavelengths. Furthermore the spatial and temporal profile of the beam means that at different positions different intensities are present. As can be seen in Fig. 2.3 (a) the maximal conversion is reached after different distances for the different intensities at different spatio-temporal pump beam positions. This means that at the center, the process starts to reverse, which is referred to as oversaturation, while at the wings of the pulse the pump power is not fully converted. However due to temporal and spatial walk-off effects the same seed does

not experience the same pump intensity over the entire propagation in the crystal. This in essence reduces the back-conversion and can lead to a better overall conversion efficiency.

In Fig. 2.3 (b) we can see, that a higher seed input leads to a shorter period, meaning that to reach saturation for a low gain OPA stage, shorter crystals are required. The saturation peak also gets thinner, that only slightly better overlap between the different gain spectra for different powers can be achieved (not shown).

It should be mentioned that most of the pump depletion occurs at the end of the propagation. If there is temporal walk-off in the crystal the most of the initial propagation in the crystal can be ignored and only the position at the end of the crystal is important if the crystal is of an appropriate length. These effects will be discuessed in the next section.

2.7 Spatial and temporal effects

As the pump beam is propagating partially along the extraordinary axis the $\vec{k}$- vector is due to the birefringent nature of the crystal not completely parallel to the propagation direction. The pump is therefore propagating away from the optical axis as can be seen in Fig. 2.4. The angle δ_{wo} at which this effect occurs can be estimated by [22]:

$$\delta_{wo} = \frac{n_e - n_o}{n_e} sin\,(2\phi) \tag{2.26}$$

In BBO for example the effect is typically on the order of 50 mrad or about 3°. As an example, in a 4 mm crystal one would expect significant effects on the $\omega_0 = 100\,\mu$m range. This corresponds to pump energies of about $10\,\mu$J if a picosecond beams is focused to an intensity of about 100GW/cm^2. Only if less pump power is used or available this effect needs to be taken into account.

A process where this becomes especially important is the NOPA. Here, the three beams are already propagating in different directions. One can now orient the crystal in such a way that the walk-off is in the direction of the signal or the idler. If the walk-off is in the signal direction it is called walk-off (WO) compensation geometry while the other orientation is called tangential phase matching orientation (PO) as can be seen in Fig. 2.4.

It should be noted that the overlap of the pump with signal and idler is important for efficient amplification. As the idler angle is often larger than that of the signal, the PO orientation often leads to higher gains. The beam moving in the opposite direction to the pump might however become elongated as the amplification on the side of the pump is stronger. The WO orientation can there sometimes lead to a better beam profile.

In practice, a change of the different configurations can be achieved, either by rotating the crystal 180° around the propagation direction and tuning the phase matching angle difference to the cut angle in the other direction or turning the crystal so that input and output surface are changed and similarly adjusting the phase matching. An orientation where the optical axis and therefore the walk-off is perpendicular to the noncollinar angle should not be used as this suffers only the negative sides without any advantages.

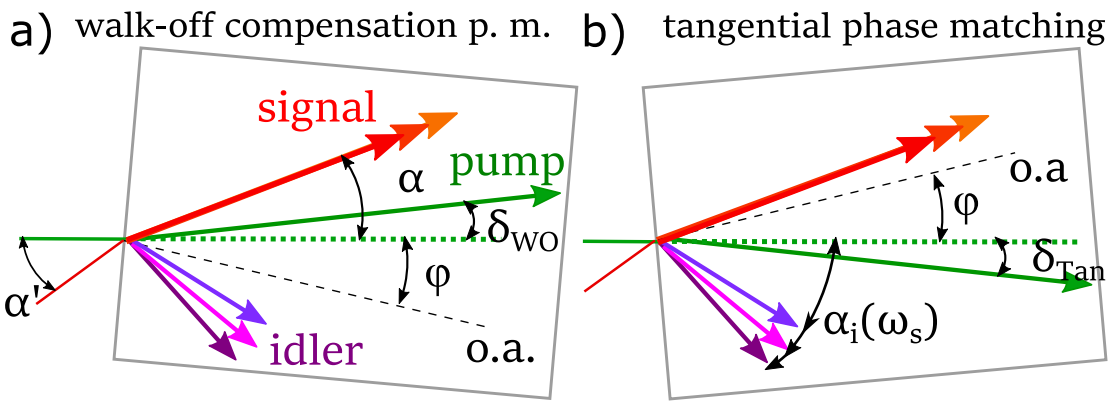

Figure 2.4: Phasematching orientation for a NOPA a) walk-off compensation orientation b) tangential phase matching orientation.

Another effect to consider is the temporal walk-off due to the difference in group velocity between pump, signal and idler the beams become temporally separated over propagation in a crystal. These differences are typically on the order of 100 fs/mm. This effect becomes therefore important if few-fs pulses are used as is commonly the case in intrapulse DFG. The effect has also to be considered for (sub-)ps pump pulses in OPCPAs, where few mm thick crystals are used.

2.7.1 Phase matching and angular divergence

Additionally, one needs to consider that a focused Gaussian beam consists of different k-vector components. As we have seen in Eq. 2.19 there is typically a quadratic wavelength dependence of Δk for broadband OPAs. As the amplification is strongest where Δk is smaller, the different k components of the seed might be more efficiently amplified at slightly different angles. This effect can lead to a spectrum that varies with the propagation angle or so called angular dispersion. In the far field this angular dispersion will then transform into a spatial dispersion. As this effect is quadratic in frequency, on one side of the beam one will find the center frequencies while on the other the short and long wavelength components can be found. Due to this, it is also not easy to compensate this effect, as the most common method of compensating angular chirp by prism wedges introduces linear angular dispersion and therefore is not useful in this case. The effect is however often not as problematic as it might appear. As the OPA is often close to the focus, in all subsequent focuses this effect will also be angular while in a collimated beam the effect is turned into a spatial effect. As further nonlinear stages are normally also placed in or close to the focus and this effect will be predominantly angular dispersion so that the different wavelengths will overlap in space and therefore are able to produce a short pulse.

2.8 Influence of the pump beam size

We will now consider the influence of the pump beam size and shape on the seed beam. The Rayleigh-length is typically much longer than the crystal, therefore we will here assume that the beam size of the pump is independent of the propagation direction. The pump intensity in a Gaussian beam scales as

$$I\left(r\right) = I_0 exp\left(\frac{-2r^2}{w_p^2}\right). \tag{2.27}$$

Since the nonlinear coefficient scales with intensity as $\Gamma(r) = q\sqrt{I(r)}$, we can combine this into the gain equation 2.13. Assuming perfect phase matching ($\Delta k = 0$) this yields:

$$G(r) = exp\left(2Lq\sqrt{I_0}exp\left(-\frac{r^2}{w_p^2}\right)\right) = exp\left(ln\left(G_0\right)exp\left(-\frac{r^2}{w_p^2}\right)\right) \tag{2.28}$$

where $G_0 = G(r = 0)$ is the gain for the center intensity. Let us now inspect where the gain drops to $\frac{1}{e^2}$ of the center gain to compare it to the beam size of the pump:

$$\frac{1}{e^2} = \frac{exp\left(ln(G_0)\, e^{-\left(\frac{r}{w_p}\right)^2}\right)}{exp\left(ln\left(G_0\right)\right)} = exp\left(ln\left(G_0\right)\left(e^{-(\frac{r}{w_p})^2} - 1\right)\right) \tag{2.29}$$

By taking the logarithm we can simplify this to

$$e^{-(\frac{r}{w_p})^2} = \frac{-2}{ln(G_0)} + 1 \tag{2.30}$$

which can be further reduced to give the final result:

$$\frac{r}{w_p} = \sqrt{-ln\left(\frac{-2}{ln\left(G_0\right)} + 1\right)} \approx \sqrt{\frac{1}{log_{10}G_0}} \tag{2.31}$$

In the case that the seed beam is sufficiently larger than the pump beam ($w_s > w_p$), the beam size of the amplified seed $w_{s,out}$ is dominated by the gain and therefore by the pump beam. The condition for r where $I(r) = \frac{1}{e^2} I_0$ here is analogous to the amplified output beam waist $w_{s,out}$ although the amplification shape is not Gaussian. The approximation made at the end of Eq. 2.31 is not derived analytically but a numerical finding. For example for a center gain of $G_0 = 100$ the beam size of the output $w_{s,out} = 0.75 w_p$ is only slightly smaller then the pump. This factor might be even closer to unity when the saturation limit is reached as then the pump pulse shape is the limiting factor. In this case the beam shape will then also become more like a Gaussian. As the output seed beam position is dominated by the pump, the OPA can have a stabilisation effect on pointing differences between the beams e.g. if the seed beam drifts or changes its focal position due to instabilities in the supercontinuum generation or air fluctuation.

Up to now the discussion was limited to collinear amplifiers. In a NOPA this effect is somewhat mitigated in the noncollinear direction as the position of signal and idler is not constant with respect to the pump. This can also lead to a slightly elliptical output beam profile of the NOPA.

2.8.1 Pump divergence

However not just the beam size in the crystal can be influenced by the pump but also the divergence of the beam. As the phase matching determines the k vectors of the amplified beam, the spread of k vectors in the amplified signal and idler beams are limited by the spread in k-vectors in the pump beam and therefore the divergence of the signal beam will be modified by the divergence of the pump. If the signal has a larger k-vector spread than the pump, the amplified output divergence will be limited by phase matching. On the other hand, if the seed beam has a much smaller divergence and therefore a narrow k-vector spread, the spread in pump k-vectors will broaden the seed and idler wave-vector

components. So that in both cases the divergence of the amplified output will be strongly modified by the pump divergence and not just the seed beam as is initially thought.

We can estimate the transverse k-vector component by the divergence angle. $\Delta k_d = 2 \cdot k \cdot \phi_d = 2 \cdot \frac{n2\pi}{\lambda} \cdot \frac{\lambda\sqrt{n}}{\pi w_0} = \frac{4n^{3/2}}{w_0}$. Therefore, the tighter the beam is focused the more pronounced this effect will become. But even for relatively loosely focused beams in the few 100s of μm, $\Delta k_d \cdot L$ can easily approach unity and can therefore have a significant impact on the amplification.

As beam size and divergence uniquely determine the beam parameters at any following position, we see that the output seed beam is under the correct conditions determined by the pump beam instead of the input beam.

Chapter 3

OPA architecture

With the fundamental knowledge about the OPA process, we can now give a short overview over design considerations of OPCPA systems. A typical system consists of a few components that need to work together, which will be discussed in the following:

- pump laser
- broadband seed generation
- frequency conversion stages
- power amplifier stage

3.1 Pump laser source

There are only a few parameters that are important for the pump laser source: the maximal pulse energy and repetition rate together give the average power. The central bandwidth together with the spectrum determines the Fourier-limited pulse duration. For narrowband sources the exact spectrum is of less importance except that the bandwidth limits the pulse duration as these pulses are often ideally compressed very close to the Fourier-limit. Other parameters such as beam size can easily be adjusted by a telescope. While in principle beam quality is also a parameter that varies between laser sources, nowadays at least most available laser sources have decent enough beam quality, i.e. an M^2 - parameter that is close to unity. For the OPA stages themselves this is not of much significance, as the beam diameter is much larger than the diffraction limit. Therefore, beam quality can be adjusted for by choosing different focusing conditions.

3.2 Broadband seed

One can already start with a broadband laser source. These are often Ti:Sa lasers. These sources can be identical with the pump laser. However, they are limited in average output

power, and therefore in pulse energy in high repetition rate laser systems. As often higher pump pulse energies are required, one option is to temporally synchronize such a broadband source to a narrowband high pump power laser [24]. This can, however, lead to temporal jitter between the pulses. It also requires investment in a second laser source, demanding significant table space and increasing the complexity of the system.

An advantageous approach is therefore to directly produce a broadband seed pulse from the pump laser. There are many broadening techniques available. Many of them are less feasible for high average power pump sources with pulse durations in the picosecond range due to the high broadening required as well as the high average power needed to compensate for the reduced intensity due to the longer pulses.

Broadening can be achieved in different fibers. However, to achieve significant broadening with narrowband ps pulses can be challenging to achieve due to the high average power in hollow-core fibers [25]. In photonic crystal fibers [26, 27] similar problems are present to achieve sufficient broadening for some broadband OPA applications. Furthermore, the broadening is predominantly to the red side of the fundamental due to dispersion which is often not as useful. Only ANDi (all-normal dispersion) fibers [28] can achieve significant broadening to the blue side of the spectrum but are are still limited in the maximal achievable broadening.

One broadening mechanism that has reached attention in recent years is the broadening in thin plates. The approach is to achieve sufficient broadening in multiple thinner plates to avoid a critical self-focusing to a filament. To achieve this, often focusing geometries such as multipass cells are used [29, 30]. Ideally, the pulses need to be compressed between the different thin plates. Highly specialised chirped mirrors are then needed for the focusing mirrors.

Besides the intensity limitations, OPA systems require the beam paths to have the same length so that the beams overlap in time. Both fiber based broadening systems and multipass cells often require long beam path. The pump beams then needs also to propagate over the same distance making it less viable to be used for OPCPA systems. As both these techniques achieve significant broadening with high power throuputs, they are often not used for OPCPA systems, but used on their own. However, this then does not provide passive CEP stability.

A method to avoid these problems is supercontinuum generation by a filament in bulk material. As this is the main method used in this thesis, Sec. 3.6 will discuss this in detail.

3.3 Wavelength conversion

One main advantage of the OPA is that it not only allows to achieve a broadband spectrum but also to shift the wavelength to a different region by a DFG process [16]. While in principle the idler can be at shorter wavelengths than the seed, most often the seed is closer to the pump beam. Therefore, the idler is often at longer wavelengths in the mid-infrared. As we have seen in Sec. 2.2, the CEP of the idler is the difference between the CEP of pump and seed. This also allows to achieve passively stable CEP if the pulses are

of the same harmonic order, e.g. a seed generated by the fundamental of the laser and a DFG pumped by the fundamental of the same laser or seed and pump both originate from the second harmonic of the laser.

For reaching higher frequencies, it is also possible to use the sum frequency between the broadband seed and the pump source, which would destroy the CEP stability, or generate the SHG of the mid-infrared pulse which would keep the CEP stable. This can for example be used to convert a passively CEP stable idler in the SWIR range back toward the NIR range [31, 32].

3.4 Power amplification stage

As power OPA or main amplification stage in some systems the last (few) amplification stage is referred to. It is typically characterised by using the main part of the power from the laser source(s). Often, these stage only have a low gain as this allows to use a thinner crystal to achieve a larger amplification bandwidth [33].

As broadband pump sources need to be stretched to fit to the already stretched seed, these setups are called optical parametric chirped pulse amplifier (OPCPA) [16]. In more modern systems, where narrowband lasers that give a high output power are used, the pump is already in the picosecond range and therefore does not need to be stretched, the name OPCPA is still kept.

3.5 Limitations

The power limitations arising in achievable OPA systems are not so much fundamental as they are given by the pump laser used. OPAs are not fundamentally limited in output energy. While some crystals might not be able to be grown in sufficient sizes to increase the beam size to keep the intensity limited, there are nowadays crystals for most ranges that are commercially available with sufficient apertures and thicknesses.

For average power the scaling is less favourable. As it is not easy to cool the OPA crystals, thermal effects might become limiting. This can be avoided by splitting the amplification in multiple crystals, for example. As in practice it is challenging to achieve pump efficiencies in an OPA above 10-20%, the available pump laser power limits the maximum output.

The achievable bandwidth is limited by the stage with the least broadband output. It is therefore important in designing an OPCPA system that all stages are sufficiently broadband and achieve the correct spectral range. Approaches to overcome this limitation however exist. They focus on amplifying different parts of the spectrum in different crystals either in serial or parallel [34] to each other. One approach of the latter is to split the spectrum by dispersive optics into wavelength components and building several amplification stages in the Fourier-plane of a 4-f setup. This is known as Fourier-plane OPA or FOPA [35].

It is however important to point out, that the more complex a system is, the more work is required to maintain it. The same is often also true for pushing for the best parameters. OPA systems are in the end a tool to perform experiments with. Reliability and ease of use are often more important to ensure that as much time for the experiment is available.

3.6 Supercontinuum generation

3.6.1 Self-focusing and self-phase modulation

Under normal conditions, the maximal B-integral in a material is limited by the maximal intensity due to the damage threshold of the material as well as the maximal interaction length. The latter is limited as the tighter focusing results in a larger divergence and therefore a short interaction at this higher intensity. One of the main prerequisites for supercontinuum generation in bulk is therefore self-focusing. This non-linear focusing occurs as the nonlinear phase due to the Kerr effect leading to a higher phase distortion in the center of the pulse, where intensity is higher compared to the wings. This phase profile serves as a lens. As the effect scales linearly with intensity I_{peak} but is reduced in larger beams with effective area A the effect actually scales with the pulse power $P = \frac{I_{\text{peak}}}{A} = \frac{E_{\text{pulse}}}{t_{\text{pulse}}}$. To have a long interaction it is required that the self-focusing exceeds the natural divergence of the beam at which point the beam will collapses into a filament. This happens under the condition that the power exceeds the critical power

$$P_{crit} = \frac{0.15\lambda^2}{n_2 n_0}. \tag{3.1}$$

The distance at which a collimated beam with pulse power P will collapse can be calculated to [36]

$$d_{SF} = \frac{2.36w^2}{\lambda\sqrt{\left(\sqrt{\frac{P}{P_{\text{crit}}}} - 0.852\right)^2 - 0.219}}. \tag{3.2}$$

This typically results in a long distance that often exceeds the crystal length. It can however be shortened by using a focused beam. If the beam is focused by a focal length f, the distance at which the filament sets in is then reduced to

$$\frac{1}{d} = \frac{1}{d_{\text{SF}}} + \frac{1}{f}. \tag{3.3}$$

In practice it can be even shorter if the crystal surface is close to the focus of the initial beam, which results in a filament that can form around a mm into the crystal. In theory the filament would continue to collapse. In practice however the high intensity will lead to multi-photon absorption in the material which will lead to an equilibrium beam size until other processes become dominant.

In this high filament due to the high intensity many non-linear interactions can take place. The dominant process however typically is self-phase which we will discuss now. This is in some respect the temporal equivalent to the spatial self-focusing. As the Kerr effect scales with intensity, the temporal profile of the pulse will lead to a temporally varying phase

$$\phi(t) = \omega_0 t - \frac{2\pi}{\lambda} \cdot z \cdot n\left(I(t)\right). \tag{3.4}$$

As a phase of the light field is defined as $\phi = \omega t$, such phase fluctuations are synonymous with generation of new frequencies

$$\omega(t) = \frac{d\phi(t)}{dt} = \omega_0 - \frac{2\pi L}{\lambda}\frac{dI(t)}{dt}n_2. \tag{3.5}$$

On this side the effect is also much stronger due to the normal dispersion of the crystal. In the temporal center of the pulse the intensity is highest. The group velocity v_{g} also becomes intensity dependent by

$$v_g = \frac{\partial\omega}{\partial k} = \frac{c}{n_0 + n_2 I - \lambda \underbrace{\frac{dn}{d\lambda}}_{<0}}. \tag{3.6}$$

Therefore, the pulse compresses towards the trailing edge, where the blue components of the supercontinuum are located. This can lead to a temporal pulse splitting of the blue components. The new spectrum is also strongly chirped.

A typical supercontinuum spectrum consists of exponentially decaying components on the red side of the spectrum while on the blue side a plateau forms, that can reach down to about 450 nm. For shorter wavelengths the two-photon absorption in the crystal starts to become important which also limits the broadening due to plasma defocusing.

3.6.2 Experimental realization and characterization

Supercontinuum generation (SCG) was performed with lasers with two different pulse durations of 0.5 and 1.1 ps. To establish optimal conditions for SCG two commonly used materials, YAG and sapphire, were tested. For our experimental conditions, especially for the 1 ps pulses, only YAG provided stable generation conditions. In sapphire the SC covers mostly the range from 500 to 600 nm with an order of magnitude less intensity in the region of interest compared to YAG, and was extremely prone to damage.

A big difference was observed in the achievable spectra. With the 1 ps a bump in the spectra between 500-800 ps was visible as shown in Fig. 3.1 (a). For a 0.5 ps pulse on the other hand, this dip around 800 nm was not present and the transition was smooth. Another difference could also be observed in the stability due to the required power to generate the spectra. If a picosecond duration was used, pushing the crystal a few tens of microns closer to the input side in relation to the position where the supercontinuum became most stable resulted in damage in the crystal. Even after moving the crystal back

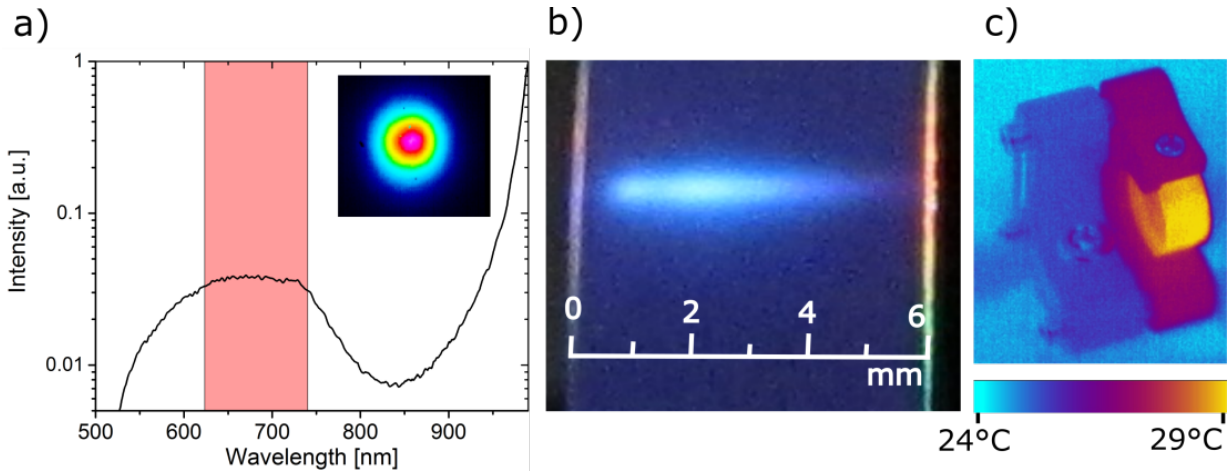

Figure 3.1: a) Spectrum of the supercontinuum generated with 1.1 ps pulses centered at 1030 nm in a 6 mm YAG crystal. The colored area marks the spectral bandwidth of the successive NOPA stage. The inset shows the spatial profile of the generated supercontinuum. b) Picture of the filament through the side of the crystal. c) Thermal image of the YAG crystal during SC generation.

to the original position, the supercontinuum was much weaker, less broad and much more unstable with fluctuations of multiple %. A sleigh rotation of the crystal to a new position was however enough to gain stable operating conditions back.

To seed the OPCPA system with a spectral bandwidth supporting ultrashort pulses, the narrowband (2 nm FWHM) pump pulses needed first to be significantly broadened. Supercontinuum generation (SCG) in a bulk material, like sapphire or YAG is a commonly used technique in the femtosecond regime [36, 37]. When the pulse duration increases to the picosecond range [38], the power required for significant broadening approaches the damage threshold of the material making the generation of supercontinua more challenging. Although SCG with picosecond pulses has recently been achieved [39, 40], its properties are still less studied than in the femtosecond range, and application with CEP stable sources are scarce [41].

For the optimal case in YAG the resulting spectrum and output beam profile are shown in Fig. 3.1(a). To monitor the position of the filament it is useful that the filament was visible as white glow through the side of the crystal, as seen in Fig. 3.1(b). It typically started around 1 mm behind the input face with a length of 4.5 mm. Accordingly, a 6 mm long crystal was used. Stable SC could be achieved with fundamental pulse energies in the range of 8-15 μJ depending on the focusing lens and crystal position relative to the focus. In our case, the most stable results for white light generation with the 1 ps long pulses could be achieved for an input energy of 11 μJ focused with a $f = 75$mm lens to a diameter of around 20 μm. The crystal did not have to be continuously moved. For the shorter 0.5 ps pulses, stable conditions could be achieved with much less input power around 2 μJ and a much wider range of input parameters. In both cases, occasionally

(50-100 operation hours) a sudden deterioration of the filament was observed, which was solved by small translation of the crystal.

It was also noticed, using a thermographic camera, that the temperature of the YAG crystal increased slightly over the first few minutes, leading to 5-7° C temperature rise with respect to ambient temperature, cf. Figure 3.1(c), indicating some residual absorption of the pump beam, most likely by avalanche ionization or multi-photon absorption. For optimal conditions, the position of the YAG crystal needed to be carefully adjusted, corresponding to a position approximately 1 mm behind the focus. This was important to avoid multiple filamentation, visible by eye as two subsequent filaments through the side of the crystal or by spectral modulations.

Furthermore, the focus position was also crucial, within few tens of μm, for output stability, in particular with respect to CEP fluctuations. After placing the crystal, the output spectrum was stable without need of movement of the crystal to avoid damage. While it was at the time believed that supercontinua generated with picosecond pulses are not stable enough, especially to be used directly as a seed for a system with passive CEP stabilization [42], here, it could be confirmed that this is not the case. In the meantime this has been more commonly established.

3.6.3 Stability and shot correlations

To study the properties of the supercontinuum, a train of supercontinuum pulses was recorded with a photodiode behind a bandpass filter transmitting a band of 40 nm centered around 700 nm. This closely corresponds to the central band of the following NOPA amplifier discussed in the next Chap. 4. Figure 3.2(a) shows a histogram of the energy distribution of the generated light. As can be seen, the generated SC is highly stable with a distribution width below 0.9% but with an asymmetric energy distribution. This indicates intensity clamping, which is expected for supercontinuum generation [43], limiting the energy of the generated white light. It was further confirmed as increasing the energy of the driving pulse (and readjusting the focusing condition) did not lead to an increase of the spectral density of the SC. To investigate the temporal correlation between pulses the Pearson correlation [44]

$$\gamma(E_i, E_i + j) = \frac{\sum_{i=1}^{N} \left(E_i - \overline{E}\right) - \left(E_{i-j} - \overline{E}\right)}{\sum_{i=1}^{N} \left(E_i - \overline{E}\right)} \tag{3.7}$$

was evaluated with $E_{i,j}$ and $\overline{E}$ are pulse energy and its average value, respectively, and $N = 10,000$ the number of pulses. As can be seen in Fig. 3.2(b), there is only 27% correlation between two consecutive shots and almost no correlation for further separated pulses. This proves that the source has similar characteristic as white noise, and thus its stability should improve with pulse averaging, as shown in Fig. 3.2(c). This, together with the small value of the rms noise, promises good stability of the system. In addition this shows that no material modification takes place in the observed frequency range.

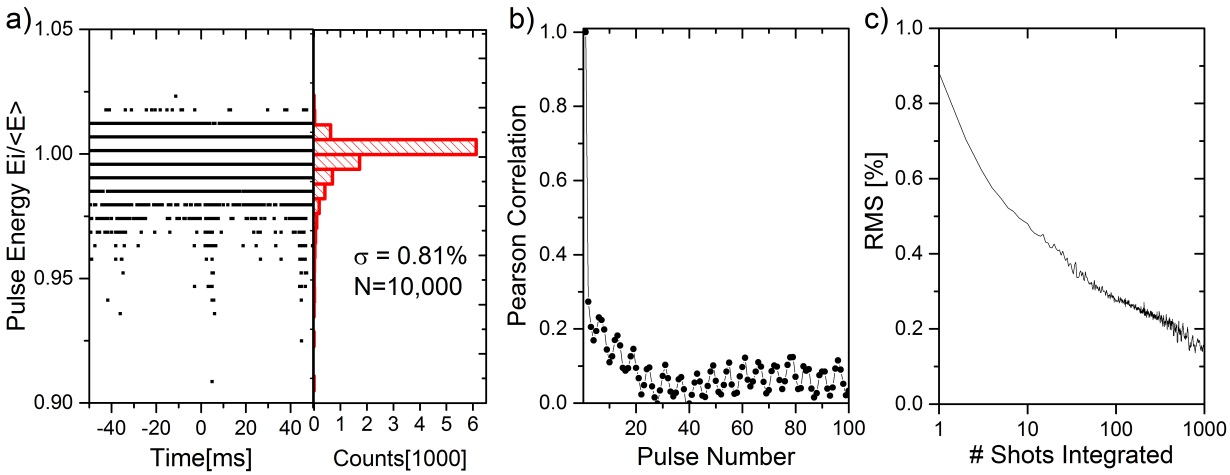

Figure 3.2: Noise characteristic of the generated supercontinuum; a) Pulse energy fluctuation of consecutive pulses with power histogram b) Pearson correlation; c) Rms value for different number of accumulated shots.

Chapter 4

High average power SWIR laser

The results presented here in Section 4.3-4.9 have been published in [45].

In this chapter a few-cycle laser system operating in the $1.7 - 2.5\,\mu$m wavelength range is described. This system is combining CEP-stable sub-three cycle pulses with $100\,\mu$J pulses at a repetition rate of 100 kHz is presented. Parts of the system, especially the generation of a phase-stable seed beam have been partially discussed elsewhere [46, 47]. Therefore, this chapter will focus on the novel aspects that have been developed as part of this thesis. After the description of the setup, results on harmonic generation in silicon will be presented as an example for its application.

4.1 Motivation

The spectral region between the NIR and MIR around 1.4-3 μm is sometimes called the Short-Wave Infrared (SWIR). Although not part of the MIR-region by traditional considerations, some authors from the ultrafast community consider it as part of the MIR-region [48, 49]. This originates from the fact, that the traditional border of the spectral regions stems from biological vibrational modes and is therefore not that applicable to strong-field science.

The SWIR range is especially useful for strong-field experiments, since the previously discussed ponderomotive energy scales with λ^2, longer wavelengths provide a significant increase of the ponderomotive cut-off energy. A prime example of potential of SWIR laser sources is high harmonic generation, where the energy of the rescattered electrons directly translates into the cut-off energy of the generated harmonics. This can be used to reach harmonics in the so-called water-window between 284–543 eV. In this range water becomes transparent, and the harmonics can thus be used to probe the carbon K-edge at 284 eV as well as other common organic constituencies such as oxygen and can thus probe organic materials, previously not accessible. Since in high-harmonic generation the ponderomotive energy scales with λ^2, longer wavelengths provide a significant increase of the cut-off energy and thus enable to cover the water window range [24, 50].

However, as the yield from rescattered electrons in HHG scales with λ^{-5} to λ^{-6}, which

makes systems in the MIR (above 3 micron) often struggle with the generated XUV-flux. Compared to a classically employed Ti:Sa system around 800 nm, a system at around 2000 nm would suffer from a reduction of photon yield around 10^2 while an even longer wavelength of e.g. 3000 nm would already decrease the yield by a factor of around 10^3. In the 2 μm system, the losses in photon yield could be compensated by increasing the repetition rate from 1 kHz typically used in Ti:Sa amplifiers to 100 kHz. For a system above 3μm this is not feasible, as the increase to MHz repetition rates would decrease the available pulse energy too much. A system around two micron therefore constitutes a reasonable compromise for high harmonic generation. The range also allows to generate harmonics in solids as will be demonstrate later in this chapter.

OPCPA systems operating around 2 μm have a wavelength range around the degeneracy range of Ytterbium-based laser systems where high powers are readily available. This allows to achieve broadband spectra necessary for few-cycle pulses which are therefore harder to achieve at longer wavelengths further away from the degeneracy point. Furthermore, the amplification is in this range more efficient due to the increased efficiency from the degeneracy but also due to the lower photon mismatch between pump wavelength and amplification window.

In spite of their usefulness, only few systems operating at high repetition rates exist worldwide. A short overview can be seen in Fig. 4.1. The figure shows the central wavelength on the x-axis, and on the y-axis a figure of merit $FOM = P_{\mathrm{av}}/t_{\mathrm{pulse}} \propto P_{\mathrm{peak}} * f_{\mathrm{rep}}$ compares the systems by their peak power P_{peak} weighted by the repetition rate f_{rep}. Figure 4.1 shows that only few other systems exist that are comparable to the system presented here. Around 2 μm there is no system that is capable of reaching a higher FOM and that could show CEP stability, which is especially important for strong-field experiments with few-cycle pulses.

Some publications which have a seed generation mechanism that should facilitate CEP stable pulses were not able to demonstrate its stability [24, 51]. At the time of publishing, the system presented in [45] (and in this thesis) was indeed one of the systems with the highest FOM that could show CEP stability. Only few systems in the SWIR range existed at the time of publication, but in recent years additional systems have been published, partially with higher power. Some of these works were inspired by the findings which are presented in [45], that will also be discussed in this thesis.

4.2 Pump laser system

Parts of the system, especially the generation of a phase-stable seed beam have been partially discussed elsewhere [46, 47]. Therefore, in the following discussion, especially related to the pump laser and chirped pulse amplification of the setup will only be discussed insofar as it is necessary for the following points or relates to improvements and changes to the previous setup.

The CPA system is seeded by a Ytterbium-based fiber oscillator (Active Fiber Systems) at 100 MHz. The pulses are then stretched by a Martinez stretcher in a folded single grating

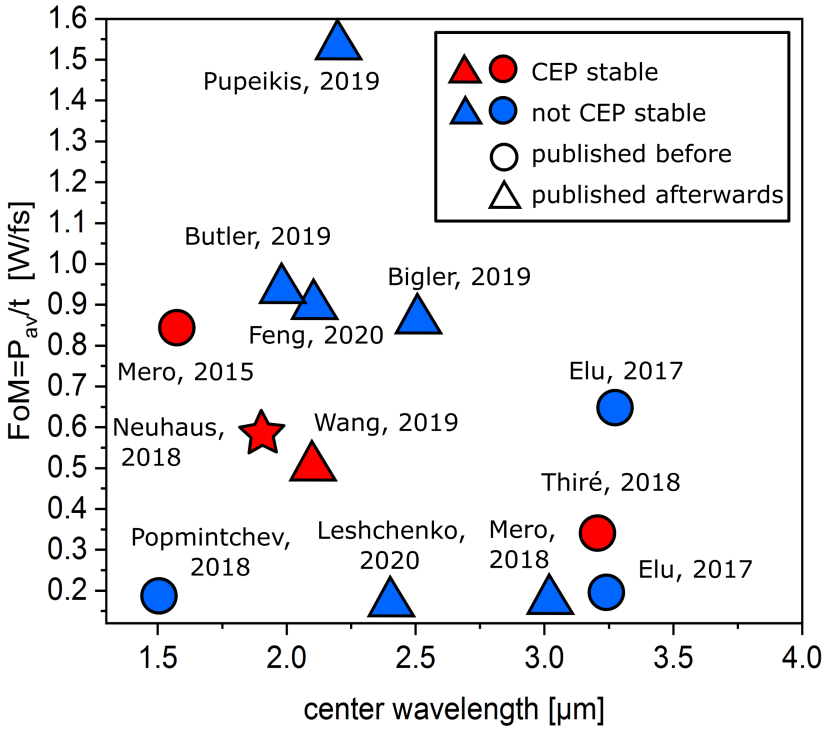

Figure 4.1: A comparison of high average power OPCPA systems in terms of the FOM [24, 41, 49, 51–58]. Publications that show CEP stability are marked in red, others in blue. Publications that were released before [45] are marked with circles and later ones as triangles.

geometry [59] that uses a grating with 1740 lines/mm (Jenoptik) to about 0.33 ns/nm. The pulses are then pre-amplified in a fiber amplifier (Active Fiber Systems) to 1.2 μJ. To protect the following laser chain, the fiber amplifier had a required threshold under which the laser interlock would activate and it would switch off. However, the in-coupling into the fiber drifted over hours and could trigger the interlock. These drifts occurred in the same direction every day and are therefore likely linked to temperature drifts in the setup. To mitigate this problem 5% of the in-coupled power was monitored on a power meter and the in-coupling could be re-adjusted using a 3-dimensional stage every few hours to avoid triggering the interlock.

The pre-amplified pulses were then sent to the main amplifier, a Yb:YAG based InnoSlab amplifier [17, 60](built at ILT Aachen). The system is able to reach 400 W of output power, and in daily operation the output power was reduced to 170 W for improved long term stability. In this laser system, a build-in beam-pointing stabilisation system (Algina, TEM) avoids the beam hitting the sensitive side-wall cooling mounting of the InnoSlab crystal. This stabilization system in addition to the stable fiber laser output and the near-resonator geometry of the Innoslab amplifier resulted in a beam with good pointing stability and stable output power that did not drift over the day. In total the system could be switched on within about 10 minutes. However, warming up of following components made a 1 hour warm-up time advisable to gain a stable and reproducible output.

The amplified 1030 nm pulses were compressed to 1.1 ps in a transmission grating compressor with a single-grating Treacy-configuration with the same type used for the stretcher with a total efficiency of 66% (110 W). The distance from the grating to the folding mirror was 0.95m and the resulting beam path in the compressor was about 4 m. A substantial part of the losses from in the compressor originated from the zero order or higher diffraction orders from the grating. To avoid excessive heat build-up in the compressor enclosure, these Watt-level beams were redirected by mirrors on a cooled beam dump. Without these measures the pulse duration was not completely stable and could change from 1.1-1.3 ps within a day due to thermal drifts which could be reduced during this work to some extent. However, the following stages of the OPCPA system proved to be nominally affected by slight fluctuations in the pulse duration.

A beam attenuator (based on $\lambda/2$-waveplate and a TFP) could redirect the power on a cooled power-head was placed between the Innoslab amplifier and compressor to allow quick power reduction to check for thermal effects due to the high average laser power.

In an inititial test version a lower power of only 21 W was used. This version will be referred to as the low power version and could be used to infer the influence of thermal effects.

Due to the input from the low-power version, a beam pointing stabilization unit was placed after the compressor to avoid drifts in beam pointing that could be observed at high powers. Most of these drifts occurred in the first hour of operation and occurred predominantly in horizontal direction. The 2° regulation range of the beam stabilisation was not quite enough to compensate for the drift of the entire day, however it reached the operation window after approximately an hour the system remained within this window

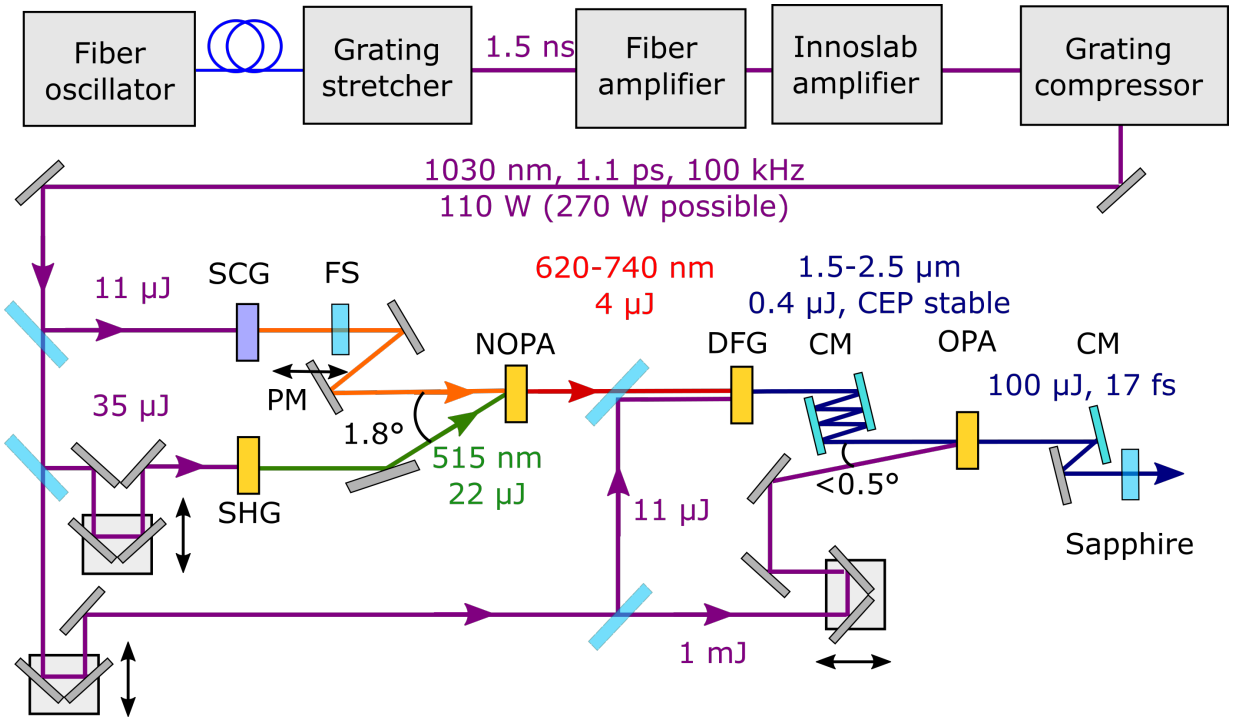

Figure 4.2: Sketch of the mid-infrared laser system; SCG: supercontinuum generation, SHG: second harmonic generation, FS: fused silica, CM: chirped mirrors, PM: piezo mirror.

for the rest of the day. As it was anyway advisable to let the other components of the system warm up for some time as well as to wait until the lab temperature has stabilized this did not constitute a loss of usable operation time.

Still some smaller pointing, also predominantly in horizontal direction, could be observed behind the beam stabilisation that typically saturated after 3-4 hours. This drift could be linked to an increase in the lab temperature, as the lab was not temperature controlled. The stretcher, compressor as well as all beam parts as well as the entire OPA were enclosed by aluminium housing to avoid air fluctuations. Hands off operation of the laser could be achieved with a day-to-day stable operation.

4.3 OPCPA layout

The following is a short overview over the system which will then be discussed in detail in the following sections. The entire setup including the CPA system is shown in Fig 4.2. The beam was divided into 4 different parts:

- Supercontinuum seed
- Second harmonic generation
- DFG pump beam

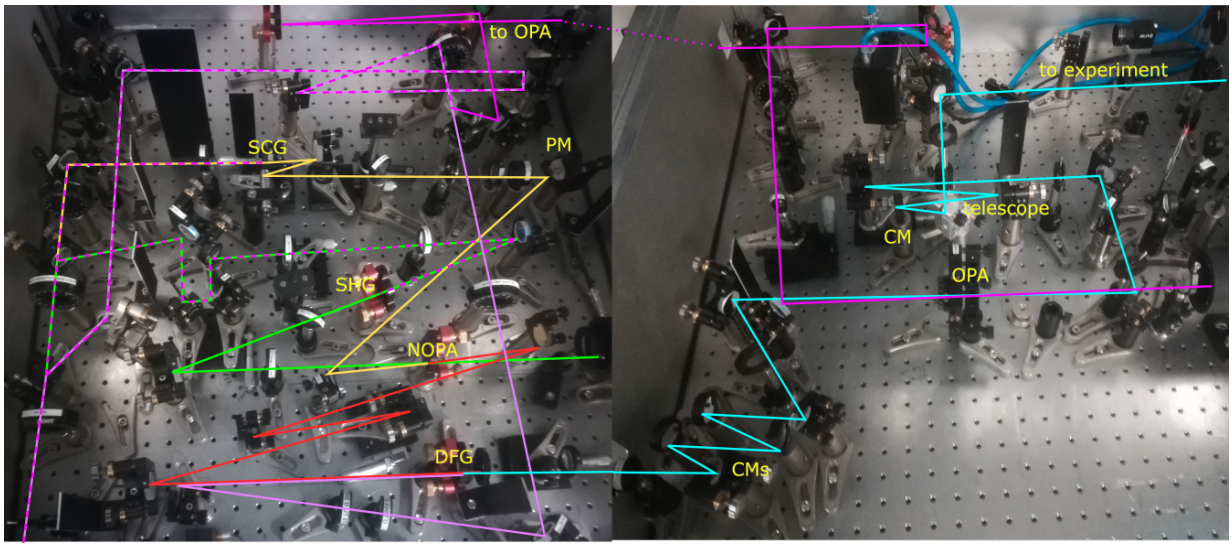

Figure 4.3: Pictures of the OPCPA system with sketched beam paths indicating the wavelength and intended use (dashed purple) of the beam . The left picture shows the seed generation box and the right picture the power-OPA box; laser fundamental (purple), SCG: supercontinuum generation (yellow), SHG: second harmonic generation (green), NOPA (red), DFG seed (light purple), PM: piezo mirror, CM(s): chirped mirror(s).

- Power-OPA pump beam

A picture of the setup with the approximate beam paths can be seen in Fig. 4.3. After the supercontinuum was generated, as described in Sec. 3.6, it was combined into a NOPA stage together with a beam that was beforehand frequency doubled in a SHG crystal. In this NOPA, the wavelength range around 620-740 nm was amplified. This amplified beam served as the pump for the DFG process. It was overlapped with a small part of the laser fundamental serving as the DFG seed. The so produced CEP-stable seed around 2 μm was then amplified by the main fraction of the pump laser fundamental in a power-OPA stage.

To split the power between the different nonlinear processes, a combination of adjustable $\lambda/2$- waveplates and thin-film polarizers (TFP) was used. This offered flexible adjustability as well as a well-defined polarization state. It is also important where exactly the split of the power is done to minimize the distance between the split beam parts to also minimize the relative pointing and phase fluctuations between this beams. Considerations need also to be given to the temporal delays. There needs to be one stage for each of the OPA stages. Adjusting one delay should have minimal impact on the other nonlinear stages. In the NOPA, the temporal delay of the spectral components is determined by the supercontinuum. For this reason the delay was implemented in the SHG to have the option to shift the temporal amplification window without affecting the delay in the later stages.

It was beneficial to have the delay of the DFG seed and the OPA pump coupled together and thereby adjusted by the same delay stage. Most of the changes in temporal delay could occur in the NOPA beam path while the 1030 nm pump beam could be kept fixed. By this

way only one delay needed to be adjusted when a path length change before the NOPA was introduced e.g. by adding dispersive material, changes in the NOPA noncollinearity angle or changes in the supercontinuum. This also served the added benefit that the delay path for both the DFG seed and the OPA pump needed to be set up only once, reducing the footprint and relative pointing fluctuations between the beams.

One also needs to take into account, that delay stages typically only consists of two mirrors at 90° to each other. Unlike a corner cube, a two-mirror delay stage reverses the pointing fluctuations only in the direction of the mirror orientation. In our case it was observed that a horizontally oriented delay-mirrors are beneficial in the DFG in order that have pointing fluctuations of the pump and seed beam going into the same direction while the normal vertical orientation was better for the NOPA delay-stage.

4.4 NOPA

In this section the generation of the NOPA pulse that serves as the pump of the DFG is discussed. The generation of the supercontinuum and the second harmonic generation that seed and pump the process will be explained before the NOPA itself will be discussed.

Around 11μJ from the laser fundamental was used to generate a supercontinuum in a 6 mm YAG crystal as has been discussed in Sec. 3.6. The supercontinuum was refocused into the NOPA crystal with a single $f = 50$ mm focusing mirror that was placed directly behind the SCG with a small angle of incidence. As this mirror was needed to re-collimate the strongly divergent SCG output, moving the mirror slightly further away from the SCG crystal resulted in a focused beam and thereby avoided an additional element for focusing the beam into the crystal. Placing this mirror on a stage to control the distance to the SCG crystal did result in a focus position after the mirror set to approximately 200 cm. This allowed for a low divergence of this beam in the crystal, which is desirable for the NOPA amplification. Mirrors had to be used for the broadband beams, as tests have shown that spherical singlet lenses introduces too much chromatic aberrations and achromatic lenses are thick and therefore cause dispersion. Mirror telescopes, on the other hand, use up considerable space. This elongates the beam path and introduce an additional element that can introduce aberrations. Therefore, the use of a single re-focusing mirror was beneficial.

The second portion of the compressed laser pulses, about 35μJ, was frequency doubled in a 2 mm BBO crystal at an intensity of 60 GW/cm^2. This resulted in 22 μJ of second harmonic radiation at 515 nm. The corresponding conversion efficiency of 63% is quite high for SHG with ultrashort pulses. In spite of this efficiency, no detrimental effect in the SHG output could be detected. After splitting off the fundamental wavelength with a dichroic mirror, the generated second harmonic beam was focused as a pump beam for the NOPA seeded by the supercontinuum.

The intended bandwidth of the NOPA should cover a spectral range of 620-740 nm. A 4 mm thick BBO crystal was used with phase-matching angle of $\phi = 23.3°$ and a non-collinearity angle of $\alpha = 1.8°$ between pump and signal. Output exceeding 4 μJ could be

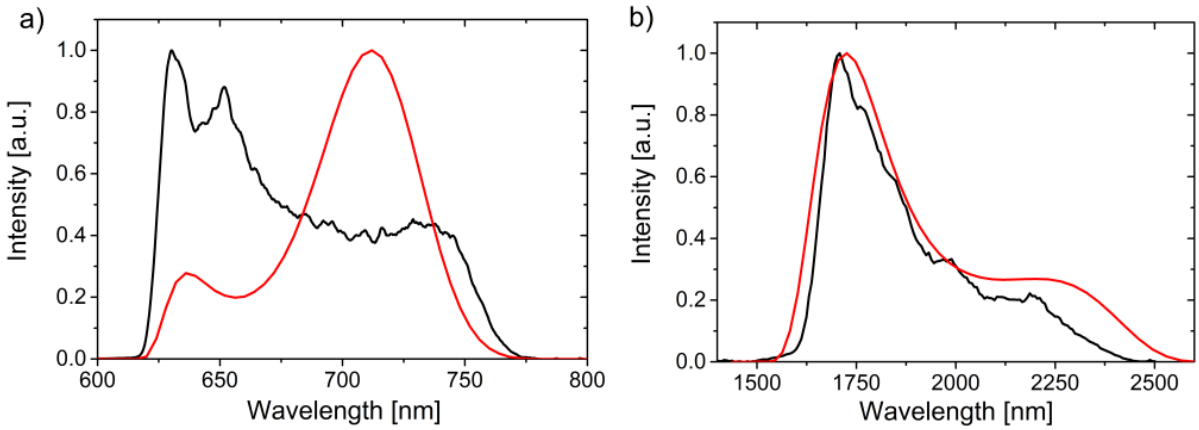

Figure 4.4: Spectra of a) the NOPA and b) DFG output pulses. Black lines: measured spectra, red lines: calculated small signal gain profiles.

achieved which corresponds to an efficiency of about 20 % and is in line what has been reported elsewhere in this region [16, 61].

As can be seen in Fig. 4.4(a), the bandwidth of the amplified pulses (black line) corresponds well to the calculated small gain profile (red line), but the calculation underestimates the short wavelength components. The discrepancy between the spectra could be due to the simplified model used in the calculation, not including spatial properties of the supercontinuum (different spectral components have different divergence) and its spectral chirp. The spectral chirp of the supercontinuum (mostly due to material dispersion), beside a quadratic term, possesses a significant third order term as was determined by a SHG-FROG measurement of the NOPA. This revealed a pulse duration of around 400 fs, which has mostly the same dispersion as the supercontinuum. This causes smaller temporal stretching of the longer wavelengths portion of the supercontinuum as compared to short wavelengths. This, together with the saturation effects in the NOPA, could lead to lower extraction of the pump energy of the less chirped (i.e. the longer wavelength) part of the spectrum, explaining the observed discrepancy. To increase the final power of the mid-IR output, an additional NOPA amplification stage could be added before the DFG stage. However, this would increase the overall path length of the pump and seed arm before DFG, where any length variations between two arms would directly transfer into CEP fluctuations. Therefore, the DFG was placed immediately after the single-stage NOPA and the post-amplification of the mid-IR pulses. As described in Sec. 2.7, the beam showed an angular chirp in phase-matching direction that was however reduced in the following nonlinear stages.

4.5 DFG

The output of the NOPA was then refocused to to a size of about $w = 80\,\mu$m by a telescope consisting of $f_1 = 50\,$mm and $f_2 = 100\,$mm lenses. First tests revealed that even a small non-collinear angle between the beams of about 0.5° still led to some residual chirp in the idler. To avoid this the two beams needed to be combined using a dichroic mirror that reflected the 1030 nm and transmitted the NOPA wavelengths. A custom-fabricated optic designed for a similar purpose by V. Pervak (another member of this research chair) was used that transmitted the NOPA output and reflected the 1030 nm beam.

The collinear beams were focused in a 1 mm thick BBO crystal in such a way that both had similar intensities of $50\,\mathrm{GW/cm^2}$. This was to ensure a minimal nonlinear distortion in the crystal while simultaneously giving the highest output power. The power for the 1030 nm pulse was set to about $0.8\,\mu$J at which the maximum DFG output could be achieved. The result was that the DFG was operated beyond saturation level to such a degree, that an increase of the 1030 nm power lead to a decrease in DFG output. As the visible part served as a pump, the output scaled linearly with the NOPA output. As a result, CEP-stable mid-IR pulses were generated with energies of $0.4\,\mu$J and bandwidths covering a range of $1.5 - 2.5\,\mu$m (see Fig. 4.4(b)). The spectrum closely resembles the theoretical gain curve.

The entire setup to generate the seed was placed in a $80 * 70\,\mathrm{cm^2}$ box, which included most of the delay stages for the power-OPA as can be seen in Fig 4.3. This is quite compact considering the four nonlinear processes were involved, each requiring focusing optics to adjust the beam sizes as well as temporal-delay adjustments. The compact setup could be achieved by folding the beam by mirrors between the stages to reduce the lateral dimension and placing the elements close to each other as well as an efficient use of space.

4.6 Power-OPA

In many setups [24, 41, 49, 61] the main amplification is split into different amplification stages. In this section I will demonstrate that the amplification can also be done with good efficiency and with a broad spectrum in a single stage. This has the added benefit of a smaller footprint on the optical table. Furthermore, it reduces the amount of optical elements needed and therefore also decreases potential sources of instability. As the beam is often refocused between stages there are more chances for cumulative aberrations. If multiple stages are used the intensity in each stage cannot be significantly reduced when compared to a single stage. The increased total length from multiple crystals leads then to a higher total B-integral than in a single crystal.

The required amplification factor needs to be as large as 1000 for certain wavelengths. As we can see in Fig. 4.5 from the small gain such amplification is not the limiting factor. The limiting factor then is pump depletion. As discussed in Sec. 2.6, the crystal thickness has only a small effect on amplification bandwidth, especially for highly saturated beams. It is then possible to use thicker crystals in which sufficient amplifications can be achieved.

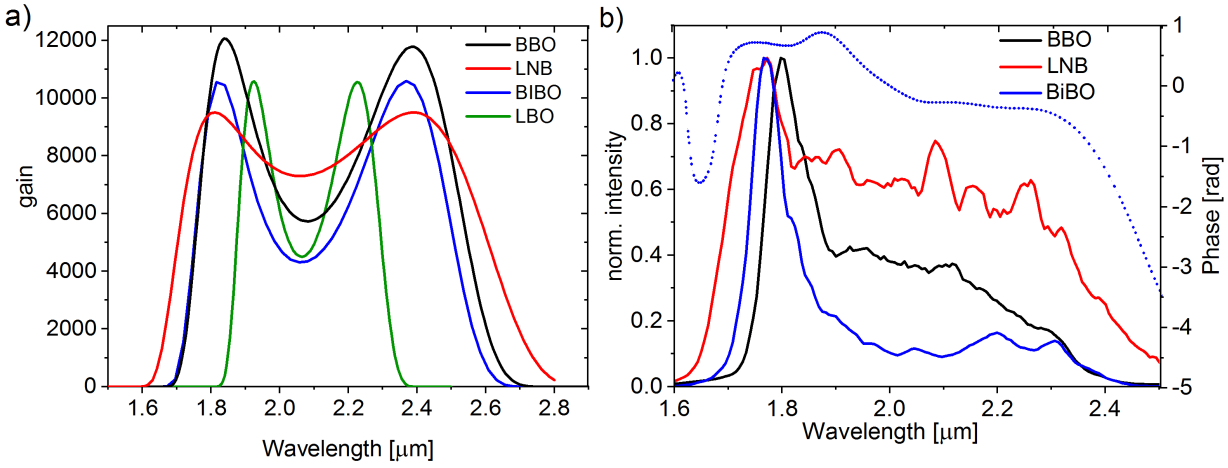

Figure 4.5: a) Small gain spectra for different amplification crystals. b) Experimentally achieved spectra optimized on pulse duration. The dotted blue line shows the phase (right axis) for a compressed pulse amplified in BiBO.

The mid-IR beam was amplified in an OPA stage pumped by the 1030 nm beam with 1 mJ energy. The pump was focused to an intensity of $80\,\mathrm{GW/cm^2}$ and the seed was adjusted to a similar beam size. In order to separate signal and idler after amplification (as they spectrally overlap and have the same polarization) pump and seed needed to be aligned under an angle of about 0.5°. The high gain and therefore high average pump power required to reach amplification in a single stage led to various challenges, which will be discussed in the following. Moving forward the power-OPA stage will simply be referred to as OPA.

As mentioned previously, in the first low power iteration of the OPA, the system was set up with a lower pump power of about 10 W with a corresponding pulse energy of $100\,\mu\mathrm{J}$. Increasing the power to the full 100 W pump and keeping the intensity constant by increasing the beam diameter led to thermal and other pump-dependent issues in different amplification crystals. In our experiments, three different nonlinear crystals were tested.

4.6.1 Amplification Crystals

The main determining factor for an implementation of an OPA stage is the choice of amplification crystal. The main parameters to consider beside the resulting output power is the achievable spectrum . These parameters are also affected by the respective phase-matching angle used. One way to compare parameters under a fair condition is to tune the process such that the shortest pulses can be achieved. Besides these parameters it is important that the amplification is operated under a stable condition as well as a good beam quality. The discussion of the advantages and issues with the three suitable amplification crystals BBO, Lithium niobate (LNB) and BiBO will be a central topic of this section.

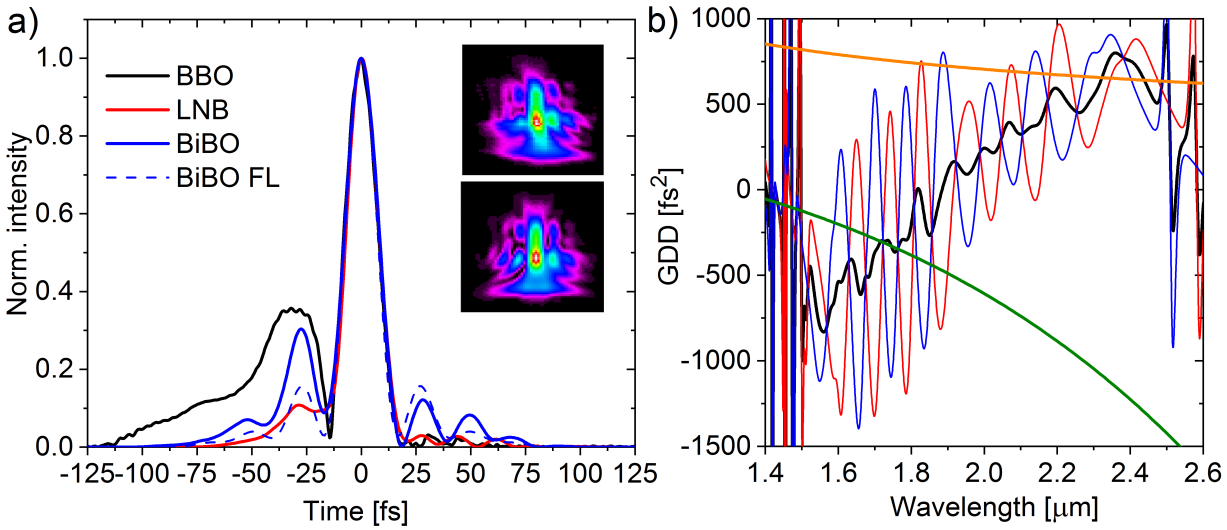

Figure 4.6: Temporal characterization of the mid-IR pulses with THG-FROG; a) retrieved temporal profile for different crystals and calculated Fourier-limited pulse (dashed line) for BiBO, inset: measured (upper) and retrieved (lower) FROG traces for BiBO. b) GDD introduced by 1 chirped mirror (design curve, red at 5°, blue at 23° AOI, black – average value), by 5 mm of sapphire (green) and GDD introduced in the mid-IR beam by placing 15 mm of UV fused silica in the supercontinuum output (orange).

The small gain bandwidth of these three crystals together with another commonly used crystal, LBO can be seen in Fig. 4.5 (a). For a more fair comparison, the length of the crystals are adjusted to give the same maximal gain and the phase-matching is adjusted to give similar center wavelengths. It can be seen that while LBO shows an insufficient gain spectrum, the other three crystal have a similar bandwidth while LNB shows the broadest bandwidth.

4.6.2 BBO

First, a 4 mm thick BBO was tested. Using this crystal, up to 120 μJ of output energy could be achieved in the mid-IR. However, the crystal was heated by more than 100 °C, which was associated with absorption of the idler beam (the temperature rise from the pump beam alone was negligible). This led to thermal stress in the crystal, which made it very prone to shattering. Most of the heating inside of the BBO crystal occurred close to the output surface where the majority of the idler was generated ,due to the exponential nature of the amplification process. Simulations using a finite element method indicated that the thermally induced stress for the same temperature gradient in a 1 mm thick crystal is two times smaller than for a 4 mm thick crystal. For that reason, the 4 mm crystal was divided into two thinner ones with thickness of 3 mm followed by a 1 mm BBO. This way, the thermal load was mostly located in the thinner crystal. The crystals were placed within a distance of less than 1 cm to keep the spatial beam separation caused by the nonlinear

angle smaller than the beam size. Although this approach avoided crystal cracking, still the high temperature of the second crystal as well as the spatial separation between beams lead to an unfavorable beam profile as well as pointing fluctuations.

4.6.3 Lithium Niobate

In the second attempt a Lithium Niobate (LNB) crystal was tested in the OPA stage. With crystal thickness of 4 mm the pump intensity had to be reduced to below 50 GW/cm^2. Higher intensities led to deterioration of the beam by the photo-refractive effect. This led to a stronger focused beam which in turn led to a stronger photo-refractive effect so that a feed-back loop emerged that would eventually damage the crystal. Even below critical focusing, this effect led to a slow thermalization and power stabilization on the time scale of hours. In this configuration, the average output power was limited to 8 W, but with a broader spectrum than for BBO as can be seen in Fig. 4.5(b).

4.6.4 BiBO

In the final configuration, a 4 mm thick BiBO crystal [62], cut in the XZ-plane, was used. Unlike the other crystals used, BiBO is not a biaxial crystal and therefore has different refractive indexes in each of the three cardinal directions. If the crystal is cut close to the phase-matching angle as is the case here the behavior should be similar to a bi-axial crystal as one of the axis is in the propagation direction and does therefore not contribute. In this crystal, output pulse energies of 100 μJ could be achieved. Due to impurities in the crystal, its temperature was elevated by about 30°C partially by the pump beam and partially by the amplified idler and seed beam. A slightly different behavior was seen in crystals from different manufacturers how much the pump and seed beam contributed to the heating of the crystal. This change in temperature influenced the phase-matching in the crystal more than was observed in BBO or LNB. This is to be expected as the refractive index is more affected by temperature compared to the other crystals [63–65]. As the crystal thermalized over the course of about two minutes, this was not problematic for the normal operation of the system, but could make interpretations of thermal effects on following elements more difficult as the spectrum changed over this time. The potential influence on the beam profile are discussed later. Due to the lower heating compared to BBO as well as more stable output conditions compared to LNB and reasonable output power, for long-term operation this configuration is most favorable and was used for the following discussion.

The output pulse spectrum is only slightly narrower at short wavelengths as compared to the DFG output, as is expected from the theoretical gain curves in Fig. 4.4(a), but still broad enough to support few-cycle pulses. The high energy stability of the OPA amplifier was achieved by saturation. This minimizes energy coupling of the previous stages to the final energy as will be discussed in the next section.

4.7 Beam characterisation

4.7.1 Saturation

To check the influence of coupling of pump and seed to the output, both parameters were intentionally reduced, and the OPA output power was monitored after amplification. By reducing the pump power and therefore also the pump intensity for very low pump powers almost no gain is seen in Fig. 4.7(a). From about 27 W the power starts to increase linearly instead of an exponential gain which would be expected from small gain calculations seen in Sec. 2.3. From that it can be inferred, that the process is highly saturated. As can be seen in Fig. 4.7(b), by reducing the seed power only small changes in output power can be observed with a scaling of roughly the 9th root. This is also indicative of a strong saturation of the process. However, if the seed was blocked, no output from parametric fluorescence (i.e. amplified virtual seed photons) could be observed. The dynamic range of this detection was at least 3 orders of magnitude as the seed without any amplification at a few mW level could be detected with the spectrometer.

If the SHG in the NOPA was blocked, although no output from the DFG could be observed, still about 30% of output power from the OPA could be seen with a spectrum shifted to the short wavelengths. Due to the strong seed in the DFG, the weak supercontinuum is strong enough to produce some weak output in the DFG. This output is then amplified in the saturated OPA. As this process originates from the supercontinuum itself and the difference is just the lack of amplification in the NOPA, it is coherent and in phase with the main pulse. This indicates, that unlike normal parametric fluorescence, this observation is not be a sign of a problematic incoherent background.

The saturation minimizes energy coupling of the previous stages to the final energy. As a result, the final stability of the mid-IR pulses was at a level below 0.9% rms, only slightly higher than the noise of the pump laser with 0.6% rms.

4.7.2 Beam profile and quality

One of the important questions is if the amplification has a negative effect on the beam profile and beam quality. For that we measured the M^2-parameter which is given as the real divergence compared to the divergence of an ideal Gaussian beam. This parameter therefore determines how well the beam can be focused.

To determine the M^2-value, the beam was focused using a spherical mirror with a focusing length of $f = 500\,\mathrm{mm}$. Two different techniques were used, a knife-edge measurement in two orthogonal directions and two photon absorption on a silicon based camera to also monitor the beam profile shape. The recorded data can be seen in Fig. 4.8 (a) and (b). The fit of

$$w = w_0 \sqrt{1 + (z - z_0)^2 (\frac{M^2 \lambda}{\pi * \omega_0^2})^2} \tag{4.1}$$

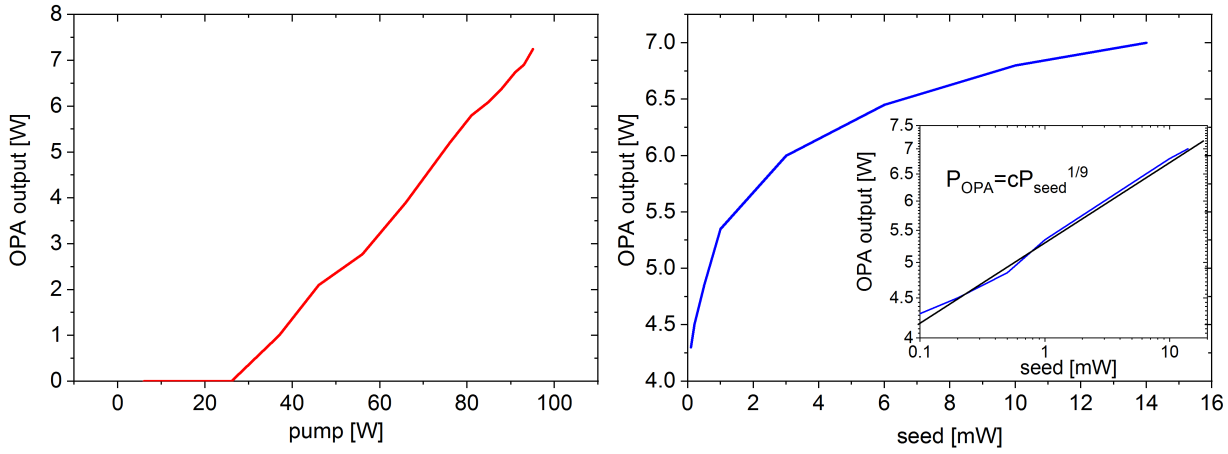

Figure 4.7: a) Dependence of the OPA power on the pump power. b) Dependence of OPA output on the seed power. The inset shows a double-logarithmic plot with a 9th root dependence.

to the beam size $w(z)$ revealed an M^2 of $M_x^2 = 1.8$ in horizontal and $M_y^2 = 1.9$ in vertical direction. A good fraction of this was observed to stem from the thermal distortion in the BiBO crystal. First, the seed beam was blocked to reduce thermal load from absorption of the amplified seed and idler beam in the crystal for a few minutes. Within a few seconds after unblocking a swift increase in size could be observed in the far field while the focus remained unaffected. From this it can be inferred that the M^2 without the thermal effect from the crystal would be in the $M^2 = 1.4$ range, which is what could be expected from an OPA system. As the thermal effect is not easily to overcome, no measures could be taken here to mitigate this effect. However as the beam is of Gaussian shape, the beam size in the experiments can be adjusted in most cases by using a shorter focusing lens.

Importantly when the pump power was reduced below saturation the beam size in the focus was only affected by less than 10%. This indicates that no significant distortions in the beam profile occurs due to back-conversion in the highly saturated OPA process.

4.7.3 Parasitic beams and their use

A lot of weak parasitic beams with a broad wavelength range could be seen as dots with equal spacing in horizontal direction, the direction in which the pump and seed had a small non-collinear angle to separate the beams. These dots were very weak with (sub-)mW level of power so that the power losses due to the parasitic beams was not a significant. The intensity of the parasitic dots was at a minimum when the crystal was oriented along the xz-axis but increased if the crystal was rotated in the mount. This behaviour is clearly linked with the non-biaxial crystal structure of BiBO. This line was not directly horizontal but at a slight angle if the pump and seed had a small angle in vertical direction, (i.e. were not directly over each other). This is due to the addition of k-vectors in the parametric processes. In this case the achievable output power was also reduced due to the spatial

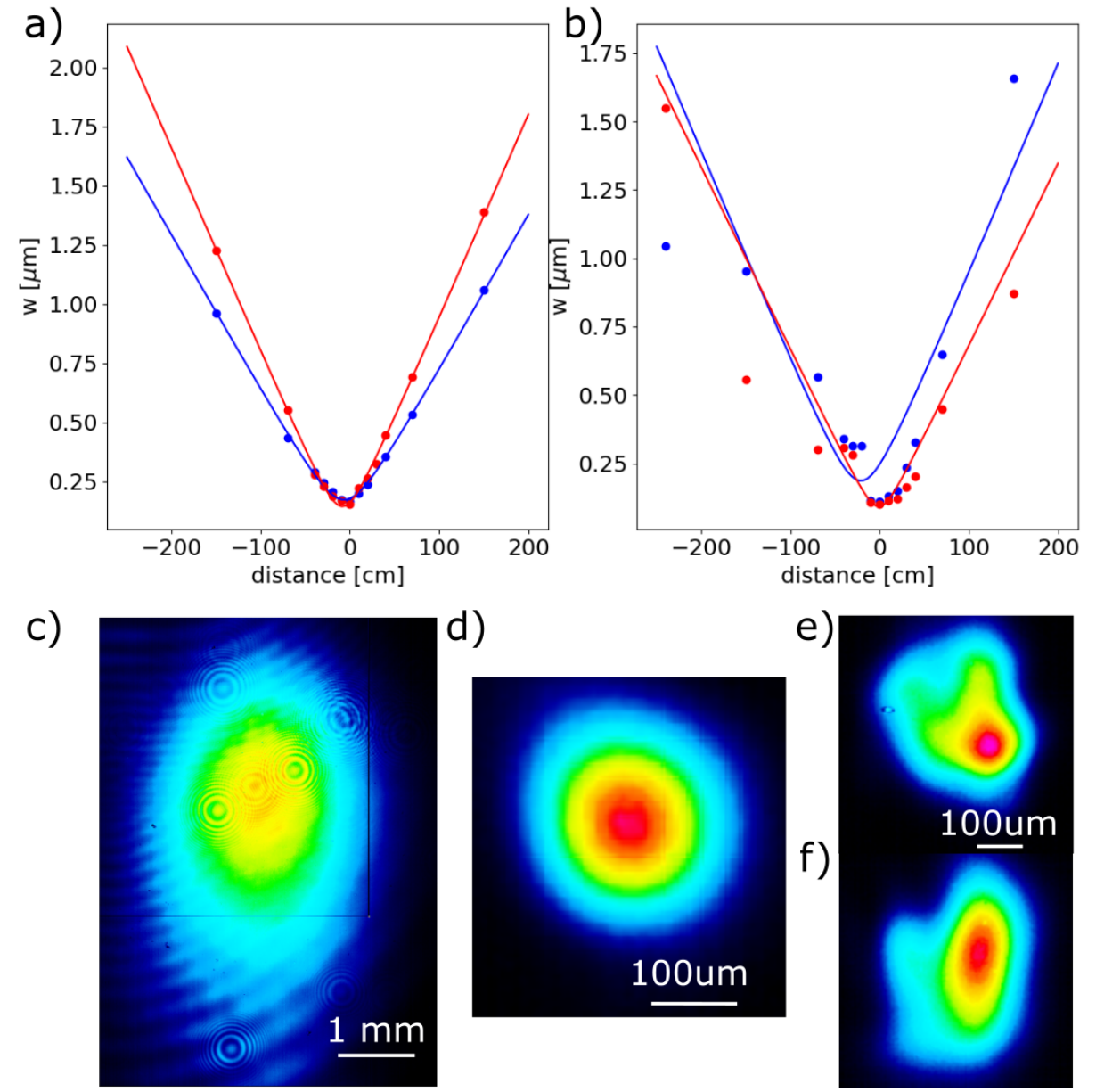

Figure 4.8: a) Beam size measurement around the focus of a $f = 500\,\text{mm}$ lens in horizontal (blue) and vertical (red) direction based on a knife-edge measurement. b) Beam sizes measured with a silicon beam-profiler based on two-photon absorption. Beam in the far field (c), in the focus (d) and 40 mm before (e) and after the focus (f), were deviations from a Gaussian profile can be seen.

overlap of the beams over the entire crystal length. Making the line horizontal could therefore be used to optimize the OPA efficiency.

Importantly, one of these parasitic dots was co-propagating very precisely with the SWIR beam so that the beams overlapped with each other over multiple meters. This dot could therefore be used as a visible guiding beam and used to e.g. fix the beam path on alignment apertures. It should however be mentioned, that the shape and color of these spots very sensitively dependent on the alignment of the OPA. If precise alignment was required as in interferometric experiments, it was therefore better to directly use the SWIR beam for alignment. However, for roughly sending the beam to the experimental setup the parametric beam was usually enough. The co-propagating spot could easily be blocked using a 1500 nm long-pass filter to avoid the parasitic beams interfering with the experiments.

4.8 Compression

One of the challenges in the SWIR spectral range is that the signal for second-harmonic generation frequency-resolved optical gating (SHG-FROG) [66] is in the range of 800-1250 nm, were no single spectrometer spanning the whole range is available, and the intensity of the uncompressed pulses is too low for higher order nonlinear characterization techniques, e.g. third-harmonic generation FROG.

To overcome these limitations, we invented a technique based on discrete dispersion scanning, which was published in [67]. This is mostly due to the limitation that commonly available wedges used in a D-scan technique are not thick enough for uncompressed pulses. The technique relies on the fact that the second harmonic efficiency for spectral chirped pulses is dependent on the spectral phase ϕ:

$$I^{SHG}(2\omega) = \left| \int_{-\infty}^{\infty} |E(\omega-\Omega)|\,|E(\omega+\Omega)| \exp\left(i\phi\left(\omega-\Omega\right) + i\phi\left(\omega+\Omega\right)\right) \right|^2 \tag{4.2}$$

When we expand the two phase terms in a Taylor series, the linear terms will cancel and result in

$$I^{SHG}(2\omega) = \left| \int_{-\infty}^{\infty} |E(\omega-\Omega)|\,|E(\omega+\Omega)| \exp\left(i\frac{\partial^2\phi(\omega)}{\partial\Omega^2}\Omega^2\right) \right|^2 . \tag{4.3}$$

This term vanishes unless $\mathrm{GDD}(\omega) = \frac{\partial^2\phi(\omega)}{\partial\Omega^2} = 0$. The second harmonic of a spectrum of a chirped pulse therefore shows a peak at frequencies at which the GDD has a zero-crossing. This allowed to use discrete material plates instead of wedges. By adding sapphire plates in the beam path before the SHG of different thicknesses with a total amount of l=0-20 mm, a shifting of the SHG peak could be observed. From each peak position we could retrieve the $\mathrm{GDD}(\omega)$ from the well-known refractive index and thereby characterise the dispersion characteristics of the beam.

While the predominant GDD could easily be compressed by material as discussed in Sec. 4.1, this left the beam with a significant amount of TOD from the material used for

compression as well as the material before the DFG stage. Based on the information from the discrete dispersion scan, chirped mirrors could be designed that mostly compensated the TOD that is left in the pulse after compressing the GDD with material. The mirrors are used in pairs at two different angles to reduce spectral fringes as can be seen in Fig. 4.6 (b). The chirped mirrors were designed and fabricated by V. Pervak.

For optimal amplification, especially in the last OPA stage, the duration of the seed needed to be stretched enough to ensure temporal overlap with the 1.1 ps long pump pulse. Different amounts of material were placed between the different nonlinear stages to achieve the overall optimal amplification. The overall best results were achieved by putting 15 mm between the supercontinuum and NOPA, but no additional material inbetween NOPA and DFG or DFG and OPA. To compress the pulses, 7 bounces of chirped mirrors and about 25 mm (20 mm of sapphire, due to a low TOD/GDD ratio and about 5 mm functional elements used for the FROG) were used. As the chirped mirrors have a quite high reflectivity and only weakly affect the pulse duration of the stretched pulse, six of the chirped mirrors placed between DFG and OPA. This improved the overall efficiency, as the OPA was saturated and therefore inclusion of the reflection losses beforehand had nearly no effect on the OPA power but reduced the losses afterwards. As the mirrors only affected the TOD, they had little effect on the temporal shape of the stretched pulse and, by this, on the temporal overlap in the OPA process.

The compressed pulses were characterized with a THG-FROG [66] measurement (see Fig. 4.6). The retrieved pulse duration for BiBO was 17.1 fs FWHM (blue line in Fig. 4.6(a)), which corresponds to 2.7 optical cycles. Similar durations were retrieved for BBO (black) with 17.3 fs and for LNB (red)with 16.3 fs. The spectra for this measurement are shown in 4.5 (b). The duration of the compressed pulse for BiBO is almost identical to the Fourier limited case, with 66% of the pulse energy contained in the main pulse for BiBO, 85% for LNB and 51% for BBO. The only differences are modified heights of the pre- and post-pulses. The modulated temporal structure is a result of the uneven shape of the amplified spectrum, as well as phase ripples from the chirped mirrors visible in Fig.4.6(b), which may be improved with revised chriped mirror designs in the future.

4.9 CEP

To measure the stability of the CEP, a home-built f-2f interferometer in collinear geometry [68] was used. As the spectrum of the pulses is less than octave spanning, they needed to be spectrally broadened, which was achieved through SC generation in a sapphire crystal using pulses with an energy of 2 μJ. Spectral interference fringes were recorded with a compact spectrometer, operating at a frequency of up to 80 Hz and an acquisition time of 4 ms. Time traces for the passively CEP-stabilized pulses are shown in Fig. 4.9 (b). Slow drift were measured on a scale of several seconds that was most likely due to the interferometric nature of the DFG process. To compensate such for slow drift, a piezo-driven mirror in the white light beam path was implemented before the DFG stage. This allowed rapid and fine tuning of the CEP phase of the generated mid-IR pulses [69]. This

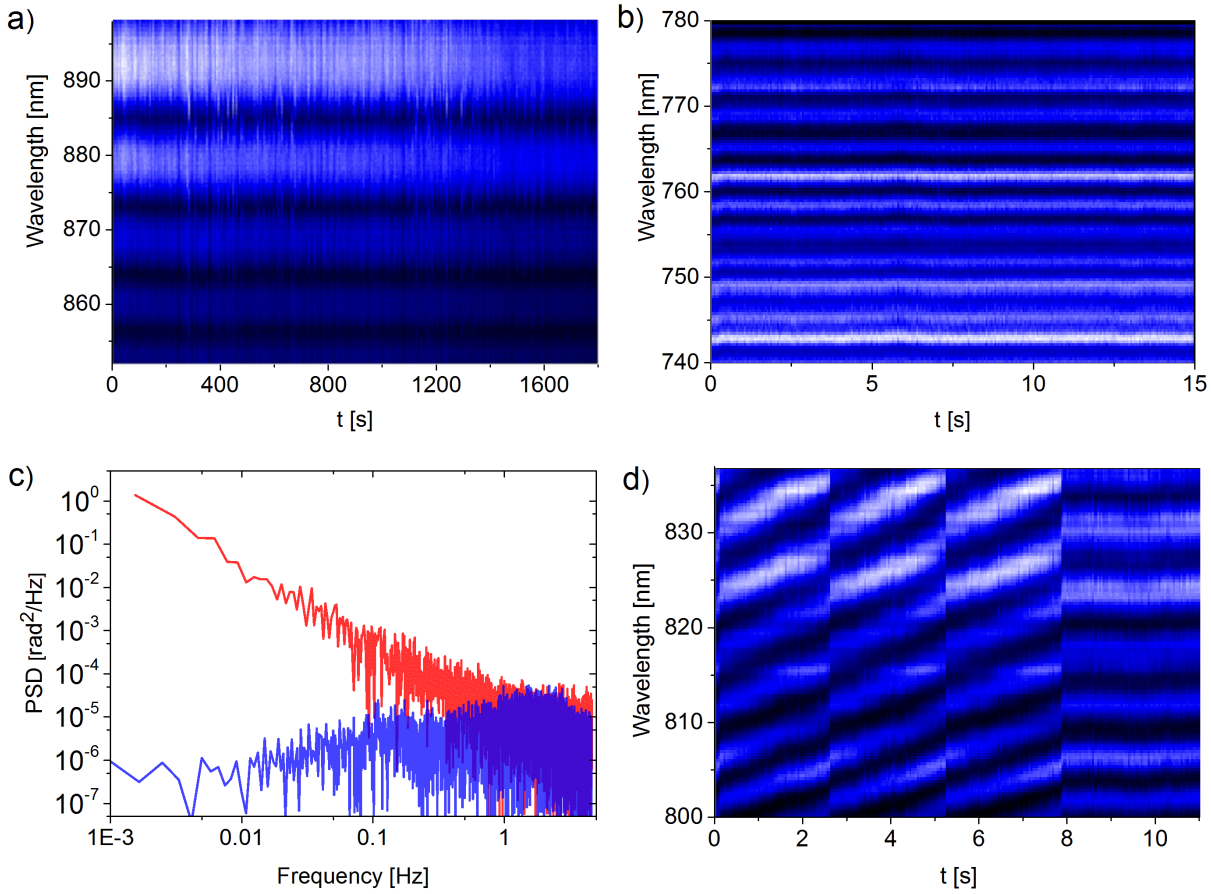

Figure 4.9: CEP phase stability: a) Interference fringes recorded with feedback-loop recorded for 30 min with 242 mrad rms b) Fringes recorded over 15 s for lower amplification and without feedback-loop show 103 mrad rms, c) comparison of the CEP noise (power spectral density) with (blue) and without (red) stabilization and d) example of the CEP phase control (0-π ramp pattern, followed by constant CEP.

way, the rms value of the CEP was measured to be 242 mrad over a time period of 30 min as seen in Fig. 4.9 (a) for an in-loop measurement. The stabilisation should mostly reduce the slow drifts as is seen in 4.9 (c). The high contrast of the measured CEP fringes implies that the relative CEP inbetween shots should stay stable, although spectra were integrated over 400 laser shots. An out-of loop measurement would help to verify these fluctuations. However, an additional f-2f spectrometer would also require a similar broadening and suffer from the same power and pointing fluctuations that are introduced in the supercontinuum and would therefore not be truly independent.

It was observed that most of these fluctuations are caused by overcompensation of the beam pointing stabilization placed behind the grating compressor that was necessary to avoid thermally induced drifts. Other causes are thermal fluctuations in either the OPA

crystal, air, or optical elements. This could be verified, as by reducing the laser pump power to about 27 W and reducing OPA pump power to 13% (and keeping the intensity in the OPA similar by adjusting the beam sizes) lower fluctuations of 136 mrad were observed over 20 minutes. Without piezo-mirror stabilization, 103 mrad fluctuations over 15 seconds were measured. Some of these fluctuations might be measurement artefacts as fluctuations in laser power and beam pointing can couple to the measured CEP [70, 71] due to position variations of the filament in SCG in the f-2f interferometer. Besides slow phase corrections, the piezo driven mirror allowed us to introduce fast CEP control as seen in Fig. 4.9(d). Thanks to the low weight of the mirror and a high strength piezo-actuator the temporal response of the system was faster than the temporal resolution of our f-2f setup (12.5 ms). This offers a faster response time than approaches based on wedge scanning or translation of a grating and could be used for fast CEP corrections or experiments for which rapid CEP scanning is necessary.

Some publications shown in 4.1 that have a seed generation mechanism that should facilitate CEP stable pulses were not able to demonstrate its stability [24, 51]. This might be due to the generation mechanism or from the complications that arise by measuring CEP for a pulse with less than an octave bandwidth. This demonstrates the difficulty to passively stabilise the CEP.

4.10 Conclusion

Here I have demonstrated an OPCPA system operating around 2μm wavelength with 10 W of output power. Compression to sub-three cycle pulse durations are shown and complemented by the CEP stability of the system. The main advancement is to push the boundaries in terms of average output power by systematically testing multiple crystals and show their respective shortcomings and advantages.This research paves the way to advance nonlinear optics with high repetition rate sources and longer wavelength ranges.

Although the system presented here operates stably on a day-to-day basis with reproducible output parameters and nearly hands-off operation during the day, one remaining issue is drifts in lab temperature over the course of the day of up to 5° C that were reproducible over the day and occurred mostly within the first 1-2 hours. Avoiding the biggest sources of scattered light could reduce these effects but not avoid them completely. The resulting pointing fluctuations are mostly compensated by the beam pointing stabilisation system placed after the compressor. The remaining drifts in beam position are in the μm-range in the seed generation setup, and are mitigated by the low coupling of the seed energy to the final output due to saturation of the OPA. In the OPA itself the beams are of larger size, around 1 mm and it is therefore not significantly affected.

The CEP stability of the system is in the range reported by similar works [41, 52]. Although the CEP is stable on short time-scales, for longer time-scales active stabilisation is required. The therefore needed measurement of the CEP by the f-2f interferometer is, unfortunatly not very robust. As the broadening by super-continuum generation in the f-2f interferometer is extremely sensitive to slight changes in the output parameters. This

makes the operation the f-2f interferometer quite labour intensive, which can cause issues for complex experiments or experiments were long measurement times are required. This limitation can be overcome by multi-color experiments [13, 72] that offer a good control over the field and are more robust.

The approach presented here will benefit from the recent and ongoing advances of high average power pump laser sources and their improved availability [60, 73, 74]. In summary, a simple and cost efficient approach to reach unprecedented average power CEP-stable mid-IR radiation is demonstrated here. The unique parameters of the system permit, amongst others, studying strong field phenomena in gases and solid media at high acquisition rates.

4.11 High harmonics from silicon

The laser system presented here has been used in many successful studies on nanotips [75], nanoparticles [76, 77], organic semiconductors [78] and light-induced currents in air [79]. In this section, I will highlight one of these applications of the laser system by showing how it was used to generate high harmonics in silicon.

High harmonics generation (HHG) from gases has been studied for many decades. In recent years, HHG from solid targets has attracted a lot of attention [80–84]. In these targets the aim is less to use the generated XUV-radiation but to extract information from the emitted radiation about the electron motion in the band structure in the present of a strong light field [84–86].

The combination of using lower order harmonics as well as longer driving wavelengths allows to use harmonics with wavelengths above 200 nm where air does not significantly absorb the emitted harmonics. These experiments can therefore be performed without the need of complex vacuum chambers. In addition the harmonics fall into a window where standard CCD or CMOS silicon-based detectors can be used, subsequently increasing the sensitivity and decreasing complexity and cost of the experiment.

4.11.1 Theoretical background

While semi-classical models exist for the gas harmonics and are known to quantitatively well describe the high harmonics from gas, harmonics from solids are more complicated to describe. Typically a full theoretical treatment based on full quantum mechanical simulations such as time-dependent density functional theory [87, 88] are necessary. These are beyond the scope of this section here. There is however a simplified way gaining partial understanding of this process based on considering charged particles in the conduction and valance band [89].

There are two processes that mainly contribute to the emitted radiation: Intraband and interband emission. Crystalline solids differ from gases by their periodic structure. The presence of a light field can transfer electrons to the conduction band by multi-photon process. When these recombine with the holes, interband emission is produced. In-between the electrons and holes are driven by the light field in the respective bands. It is beneficial to describe these in reciprocal momentum space as Bloch-waves with a wave-vector

$$k(t) = k_0 + \frac{e}{\hbar}\int_{t_0}^{t} E(\tau)d\tau \tag{4.4}$$

in the absence of scattering [90, 91]. From the semi-classical three-step model and rescattered electrons, the energy cut-off can be expressed as

$$E_{\mathrm{cut-off}} = I_p + 3.17U_p \tag{4.5}$$

where I_p is the ionisation potential (the direct band-gap energy) and

$$U_\mathrm{p} = \frac{e^2E_0^2\lambda^2}{16\pi^2 m_e c^2} \tag{4.6}$$

is the ponderomotive potential with the maximum electric field strength E_0, the electric charge e, the electron mass m_e and the wavelength λ. From the model, the maximum excursion radius of the electron can be expressed as [85]:

$$r_{\max} = \frac{eE_0\lambda}{4\pi^2 m_e c^2} \tag{4.7}$$

On the other hand, in intraband emission the excited electrons and holes are driven in the band of the material. Due to the anharmonics of the bands the carrier polarization leads to additional emission of radiation. While the harmonics originating from small perturbations in the band scale with harmonics of order n as I^n as has also been described in Chap. 2. When the fields are stronger, the harmonics are driven higher into the bands and the are charge carriers are driven into regions where the perturbation is significant and cannot longer be treated as a small perturbation. The emission of the harmonics will then deviate from the I^n scaling.

4.11.2 Harmonic generation

Here, I will describe the emission from silicon following the excitation by the previously described SWIR few-cycle laser pulses.

The highest harmonic that could be detected was the 9th due to the wavelength restrictions of the transmission in air. Therefore, a commercial silicon based spectrometer (OceanOptics USB2000) with a range from 200-1000 nm was used.

The polarisation state and excitation intensity was controlled by a combination of a wire grid polarizer, a $\lambda/2$- and a $\lambda/4$-wave plate. The beam was then focused with an $f = 100$mm focusing mirror on the sample to focus the beam to a waist radius of $w = 100\,\mu$m. Due to the short pulse duration [92], this somewhat loose focusing could be chosen resulting in a higher harmonic yield. Intensities of $3\,\mathrm{TW/cm^2}$ could be reached using just about 2 W of power from the OPA. Using more of the available output power could lead to thermal effects on optics and the high power could damage equipment. For measuring the reflected harmonics, the beam that was reflected from the sample under a small angle was then refocused using a $f = 200$ mm spherical focusing lens.

The spectrometer entrance-slit was directly placed in the focus to avoid nonlinear signals generated in the spectrometer fiber. The beam was compressed on the target by tuning the material in the beam to optimize the signal. While the 3rd and 5th harmonic where already saturating, the spectrometer leading to charges spilling to the lower wavelength, the higher 9th and 7th harmonic where typically still quite week and were buried in the noise of the spectrometer when the signal was reduced to avoid saturation. Appropriate spectral filters that let multiple harmonics pass and blocks the driver wavelength as well as the quite strong 3rd harmonic were not available, as the 9th to 5th harmonic cover nearly an octave and filters in the UV are typically quite narrow-band. We could however use, that the divergence of higher harmonics is smaller then of the lower ones. By placing an aperture between refocusing mirror and spectrometer, we could reduce the relative intensity of the lower harmonics, which enabled detection of the 3rd to 9th harmonic at the same time.

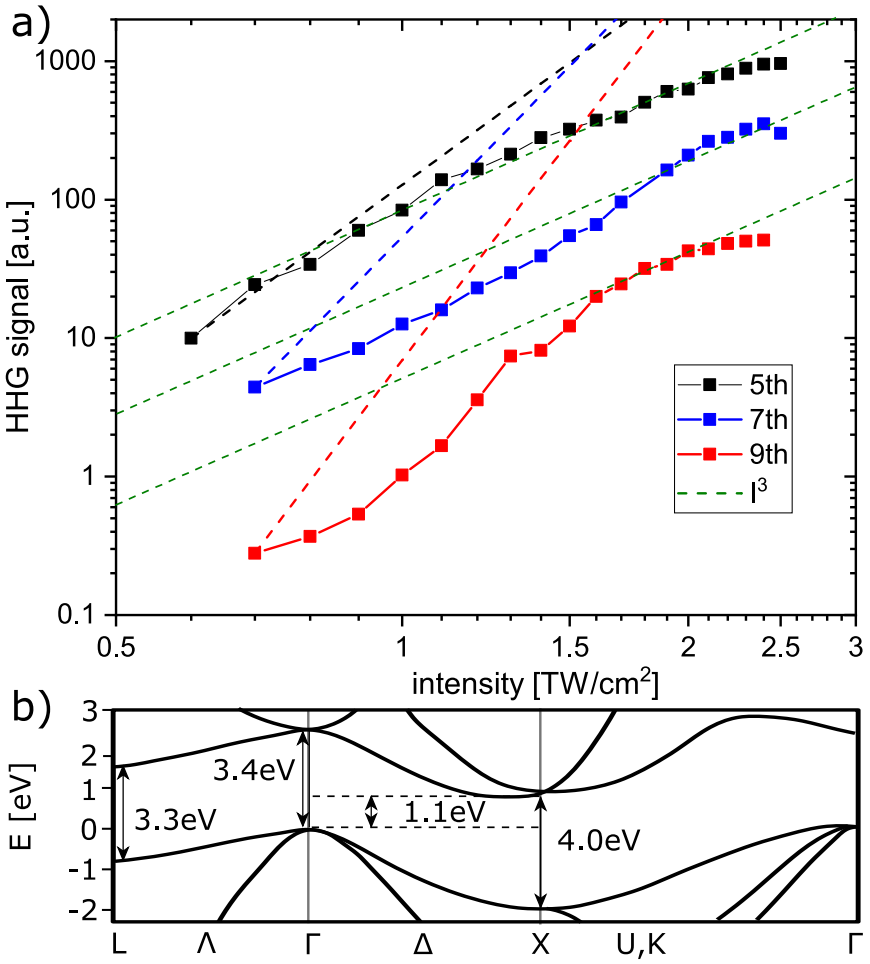

Figure 4.10: a) Intensity scaling of different harmonic orders as double logarithmic plot. Relative signal from the 5th (black), 7th (blue) and 9th (red) harmonic are shown together with the I^n (dashed line) and an I^3 scaling (green dashed line). b) Band structure of silicon [95].

A p-doped silicon plate [93, 94] cut at $< 100 >$ orientation with 300 μm thickness was placed in the beam. The beam power was varied by rotating the $\lambda/2$-waveplate in front of the polarizer. The harmonic yield of the 5th, 7th and 9th harmonic were then recorded as function of the resulting driver intensity. The results are shown in Fig. 4.10(a). The energies of the harmonics photons for a center frequency of 1.9 μm correspond to $E_5 = 3.3\,\text{eV}$, $E_7 = 4.6\,\text{eV}$ and $E_9 = 5.9\,\text{eV}$. As the direct band gap in silicon is $E_\Gamma = 3.4\,\text{eV}$, all these harmonics are higher or equal to the direct band gap of the material around the Γ-point. However, the band gap decreases towards the L-point but increases toward the X- and K-point to about 4.0 eV as can be seen in Fig. 4.10(b).

The relative intensity between the harmonic orders is only correct to some extent, as the aperture in front of the detector needed to be closed further for the higher harmonics

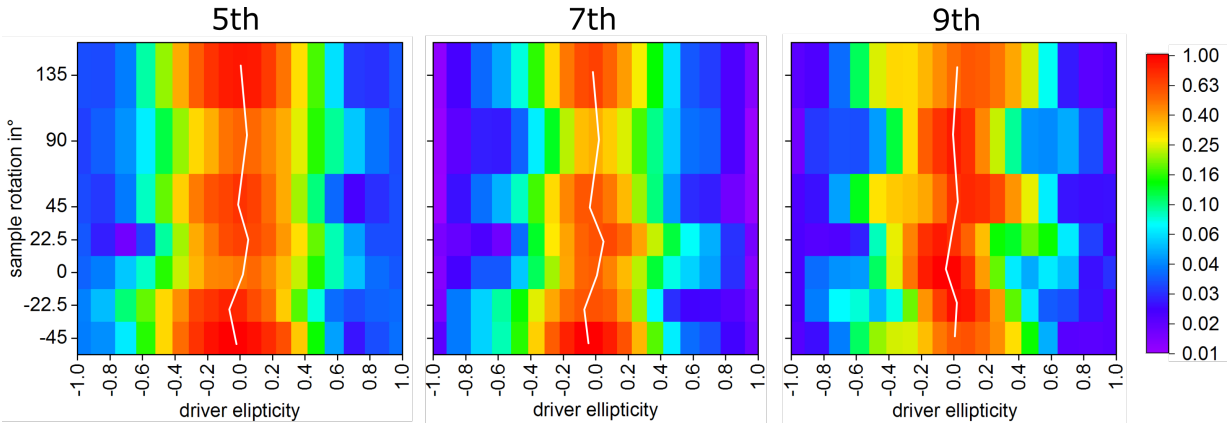

Figure 4.11: Signal of the 5th, 7th and 9 harmonic (logarithmic color-scale) as function of sample rotation and ellipticity of the driving laser. The white line makes the center of mass of the different ellipticities.

in order to avoid over-saturation of the spectrometer. While the 5th harmonic around the lower intensities up to 0.7 TW/cm^2 still somewhat follows the perturbative scaling of I^5, for higher intensities a clear perturbation from this scaling can be seen. For the 7th and 9th order deviate from the I^n scaling for all intensities. All harmonic orders follow roughly an I^3 scaling upto about 2.3 TW/cm^2, where signs of damage of the sample are visible, as the observed signal slightly starts to drop. This would correspond to a cut-off energy of $E_{\text{cut-off}} = 5.7\,\text{eV}$, very close to the energy of the 9th harmonic.

As the Keldysh parameter reaches unity at 2.1 TW/cm^2 these values agree qualitatively well with the predicted value.

4.11.3 Elliptic driver beam

In the following, the polarization was aligned by the $\lambda/2$-waveplate to give the maximal harmonic signal. This corresponds to the $< 110 >$ direction of the silicon plate as specified by the manufacturer. The intensity was set as high as possible with about 2 TW/cm^2 to be as far in the non-perturbative regime but before damage could be observed.

The polarization was rotated to 0°, 22.5°, 45°, 67.5°, 90°, 135° and 180° with respect to the $< 110 >$ direction. For each polarization, the $\lambda/4$-waveplate was rotated to scan the ellipticity of the driving laser. A positive value corresponds to right-handed polarization and negative values to left-handed polarization.

We can see that the sample orientation changes for which ellipticity the strongest harmonics can be observed, as has been observed by Klemke et al. [83]. Unlike them, we observe that the 5th and 7th harmonic show a similar behavior while the 9th harmonic shows an inverse behaviour as shown in Fig. 4.12 (a). Klemke et al. observed a difference behavior between the 5th and 7th harmonic due to the fact that they used a slightly longer driver laser of 2.1 μm with longer pulses [83]. This resulted in the 5th harmonic being below the band gap energy, while for our slightly shorter driving wavelength, the 5th harmonic

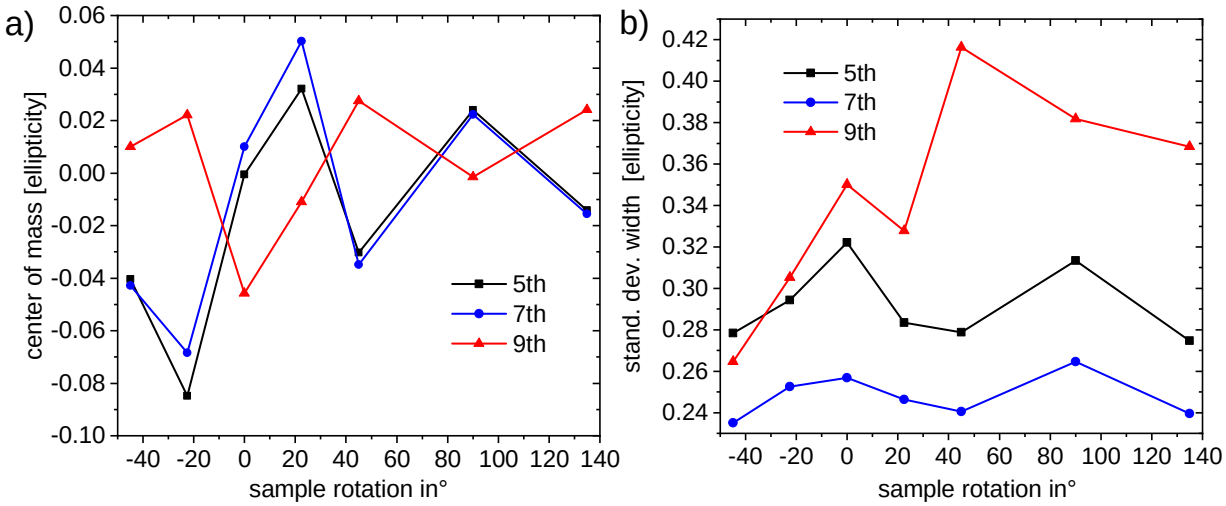

Figure 4.12: Parameters of the ellipticity for different sample rotation angles. a) center of mass of the ellipticiy scan. b) Width of the ellipticity peak given by the standard deviation.

is above the band gap and therefore behaves similar to the 7th harmonic. The reason for the opposite behavior of the 9th harmonic the might be found in the fact that the energy is much higher than the band gap. This behaviour was observed by Klemke et al. as well. This indicates the importance of the band-gap compared to the harmonic energies as is intuitive to understand for interband harmonics.

Chapter 5

Field-resolved reflectometry setup

The results presented in this chapter have been published in [96].

5.1 Introduction

We have seen in the previous chapter that parametric processes can produce phase-stable pulses. In recent years this has enabled field detection by electro-optical sampling (EOS) and pushed the application of CEP-stable pulses from the Terahertz region further toward higher frequencies and has been pushed toward the NIR and visible. Such mid-infrared femtosecond lasers have become more prevalent in recent years as they open up a variety of applications in ultrafast spectroscopy, including bio-medical imaging [8, 97], nonlinear optics [90, 98], and nanophotonics [99]. With respect to solids, such light sources permit probing charge carrier dynamics near the band edge of low-band-gap materials [100], carrier intraband absorptions [3], and the dynamics of quasiparticles, such as plasmonic or polaron excitations [101, 102].

Conventional pump-probe spectroscopy, either in transmission or reflection geometry, measures the change of the probe light amplitude before and after interacting with a sample. The phase information of the light field is thereby lost [100, 103]. Both amplitude and phase information can be obtained with field-resolved spectroscopy [104–108] which records the electric waveform of reflected or transmitted light [102]. In these methods the time resolution is not limited by the duration of the employed pump and probe pulses. Rather, the time resolution depends on the duration of the pump and gating pulses used to sample the field. Both can be in the visible range and have few-fs duration [108].

While these applications have become more commonplace in recent years for spectroscopic applications, a completely different picture emerges for time resolved studies based on pump-probe spectroscopy, as is shown in Fig. 5.1 (a). As shown in the literature overview in Fig 5.1 (b) we can see that no studies exist that study field-resolved temporal dynamics above 40 THz. Only one work claims a detection range in transient field-resolved transmission spectroscopy of up to 100 THz [108]. In this particular work, however, only very few photons in the range above 50 THz were generated, insufficient for transient field-

resolved spectroscopy. Indeed, all follow-up work by the same authors using such a setup claim a range for transient field-resolved measurements only below 40 THz [9, 109–112]. Reasons for this limitation are partially due to increased technical difficulty to produce and detect these pulses as both require a driving laser with a broader bandwidth which is not always available. Many of the mentioned NIR-EOS implementations also rely on high repetition rate oscillators. In these systems the limited available pulse energy is already required for the MIR generation and detection. It is therefore not available for pump excitation. As the pulse energy is already limited due to the high repetition rate, sufficient pulse energy to excite the sample might not be available.

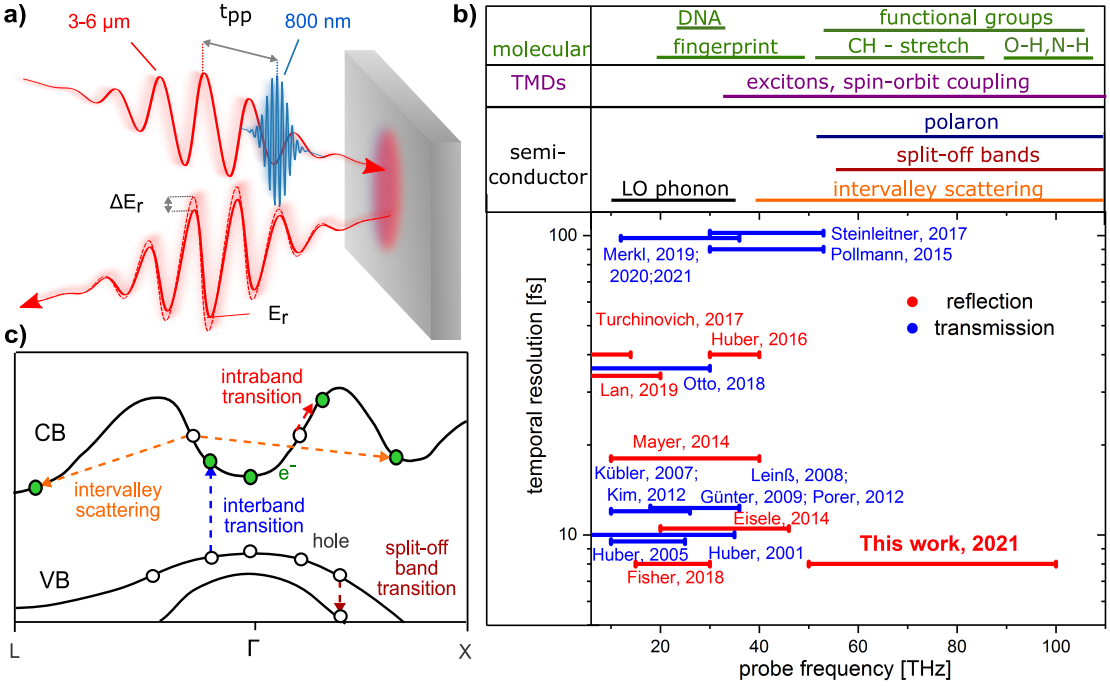

Figure 5.1: (a) Scheme for TFR reflectometry in the mid-infrared. A NIR excitation pulse induces charge carrier dynamics in the solid (depicted in gray). The unfolding dynamics leads to transient changes in the reflected waveform of the time-delayed MIR pulse. (b) Schematic of laser-induced processes in semiconductors (with exemplary valleys from Ge) that can be probed with TFR reflectometry. VB: valence band, CB: conduction band. (c) Comparison to other field-resolved, pump-probe experiments above 20 THz [3, 9, 10, 108–126]. Above are some examples of processes that can be probed in the frequency range.

Extending the detection range to 50-100 THz may enhance the measurement capabilities in many fields of science. In solid-state science it can probe excitations higher in the band and can be used to investigate the fast initial build-up dynamics of processes such as intervalley scattering [127] or transitions to the split-off bands [128] as is demonstrated in Fig. 5.1 (c). To study these processes, it can be beneficial that this spectral region is otherwise resonance-free. This allows the Drude-response of the free carriers to be investigated without background from more prominent resonances that would interfere

with the free-electron signal. The extended frequency range also enables to probe certain novel materials in new ways. For example in metal-halide perovskite , polaron excitations [129] fall within this region. In certain transition metal dichalcogenides (TMD) such as monolayer MoS_2 [130, 131], WS_2 [132, 133] and their heterostructures [134] excitons can also be probed.

This 50-100 THz range also contains the important C-Stretch, O- and N-stretch region of bio-molecules as well as the region to excite functional molecular groups. The charge separation and energy transfer processes in photosynthetic systems can also be effectively probed within the 50-100 THz window. For example charge separation in the photosynthetic reaction center can be probed in this spectral rang [135, 136], as well as CO-stretch modes that play important roles in esters, or in the study of the heme group [137]. Also the nitril group that absorbs around $2150 - 2300\,\mathrm{cm}^{-1}$, a spectral region that is free from other absorption bands, can be used as vibrational labels for proteins and DNA [137, 138].

Probing ultrafast dynamics in bio-molecules is not just important for various biomedical applications but also for organic electronics. Charge transfer dynamics at metal interfaces where an efficient transfer from the metal can be excited by the pump which often occurs on the few-fs time scale might also be a very interesting target. These processes have up to now mostly been studied by sum frequency generation spectroscopy, similar to what has been reported in [139, 140].

One should also consider the advantages of field-resolved spectroscopy compared to more conventional intensity-resolved methods. Conventional MIR spectroscopy is commonly based on so called Fourier-transform infrared spectroscopy (FTIR). The thermal MIR radiation is most commonly produced by a thermal globar source. This radiation is then detected interferometrically, by combining two beam copies on an MCT detector and varing the temporal delay of on of this beams. By placing the sample in one of the interferometer arm the absorption or emission of the sample can be obtained. While this application allows the detection of spectroscopic changes, for time resolved spectroscopy thermal sources cannot be easily used.

Therefore, other techniques based on parametric processes are sometimes used for time-resolved applications. The most common technique is based on sum frequency spectroscopy. The MIR is up-converted to convert it into the NIR range where detectors are less prone to noise and the small changes induced by a pump can be detected with higher precision. Another method commonly used in 2D-spectroscopy is to obtain the frequency information by the Fourier transformation of two laser beams in the visible or NIR spectral region.

To knowledge of the phase information in addition to the amplitude information is equivalent of obtaining the real and imaginary part of the measured quantity. Intensity-based measurements are mostly detecting the changes in the real part of the reflectivity and the small influence of the imaginary part is lost or hidden in the noise. It is often claimed, that the knowledge of the real part is sufficient as the imaginary part can be obtained using the Kramers-Kronig relation [141]:

$$Im(\chi) = -\frac{2\omega P}{\pi}\int_{-\infty}^{\infty}\frac{Re(\chi(\omega'))}{\omega'^2 - \omega^2}d\omega' \tag{5.1}$$

were P is the Cauchy principal value. As the only requirement for this relationship is causality, it is universally fulfilled. However, the Kramers-Kronig relation requires an integral over all frequencies in theory and over a broad range in practice. This is especially important if the excitation is not a sharp peak but instead a broad continuum or band, or in cases where many excitation are spectrally overlapping.

Another advantage in field-sensitive detection is that it is insensitive to thermal radiation from the sample. This is especially important in the MIR range, where the thermal emission from the sample can overlap with the investigated frequency range, especially if the samples are heated by the excitation pulse. Field-sensitive detection offers another advantage: The temporal resolution is not limited by the duration of the MIR pulse which can be difficult to compress but rather on the field-cycle duration of the detected field. While shorter delays are in principle detectable, any delay that is shorter than the frequency is interpreted as a phase shift. To obtain the shortest resolution it is therefore beneficial to push field-sensitive detection toward shorter wavelengths.

DFG requires a broadband pulse to generate, and the EOS requires a short pulse as a gate to measure the field. This short pulses, that needs to be in the sub-10fs range can then also be used as a short pump excitation beam. The short excitation pulse duration together with the field-sensitive detection, which limits a full detection to about a cycle duration of the MIR pulse, should provide a short temporal resolution in the few-femtosecond range.

Field-resolved measurements can be carried out either by transmitting or reflecting MIR pulses from the sample. While the transmission geometry is easier to perform, as the incoming and outgoing beam need not be separated and changes to the sample affect the measurement less. Some of the materials to be investigated, especially thinner samples or complex multi-layer structures might require a substrate for mechanical stability or as part of e.g. electronic control to apply a gate voltage. These materials might not be transparent to the MIR. Additionally, if thicker samples are investigated in transmission geometry, the dispersion of the material can elongate the MIR pulse. In this case using a reflection geometry is more versatile than transmission geometry.

As we have just discussed the benefits of a transient field-resolved (TFR) reflectrometry in the $50-100\,\mathrm{THz}$ or $3-6\,\mu\mathrm{m}$ range. In this chapter, I will introduce the implementation of such a system with the main purpose to detect changes in the complex electric field after excitation with a few cycle NIR pulse. First, the NIR,few-cycle, MHz laser system based on a NOPA will be introduced. Then the generation of the MIR is discussed and followed by its field-sensitive detection. This is then used in a pump-probe setup for the detection of pump-induced transient changes to the sample. The next chapter then presents some initial measurements taken with this setup on different semiconductors. These measurements serve well to illustrate both the temporal resolution of the setup as well as the broadband field-resolved nature of the detection and highlights their advantages.

5.2 NOPA laser source

5.2.1 Driving laser system

The driving laser used here is a commercial system from ActiveFiberSystems. The pulse duration can be adjusted by the length of the stretcher used for the CPA in the system which changes the GDD of the output pulse. This custom version of the laser is also equipped with a spectral filter to reduce the bandwidth. This is beneficial, as it allows the adjustment of the pulse duration without chirping the pulse which would be detrimental for the sensitive supercontinuum generation used for the OPA seed. The layout of the entire system can be seen in Fig. 5.2 (a). The system was operated at a repetition rate of 2.1 MHz and the output power was set to 50 W of which 40 W was used for the NOPA. The rest of the power was used for other purposes (other experiments as well as the in Sec. 5.5 discussed MIR-upconversion). The maximal output power at these parameters was 70-80 W but the system was run at lower powers for more stable daily operations.

5.2.2 Seed generation

The seed generation took place in a 8 mm long YAG crystal, similar to the one described in Sec. 3.6, except that the shorter pulse duration compared to the situation described in Chap. 4 allowed for a lower pulse energy of 1.7μJ to generate a stable filament and made the process less prone to damage of the crystal. No difference was observed between operating the system at 0.1 and 2.1 MHz with the same pulse energy as would be expected if the formation of colour centers takes place in the YAG crystal due to the high repetition rate.

A dichroic shortpass filter with a cut-off wavelength of 1000 nm was placed in the supercontinuum to filter out the exponentially decaying fundamental components around the 1030 nm laser wavelength. By placing the filter under a slight angle, the cut-off wavelength could be tuned to slightly downwards to about 970 nm to avoid the exponentially decaying part around the fundamental wavelength and only let the plateau pass through.

5.2.3 NOPA

The main part of the output, 1.8 μJ was used for the frequency doubled pump of the NOPA. This beam was delayed using a delay stage to match for temporal overlap. It was then focused into an 1 mm BBO crystal with an intensity of about $I = 60\,\mathrm{GW/cm^2}$ for second harmonic generation with $50-60\,\%$ of efficiency. After filtering out the remaining 1030 nm with a dichroic mirror, the beam was refocused using a $f = 200\,\mathrm{mm}$ lens into a BBO crystal with an intensity of about $I = 80\,\mathrm{GW/cm^2}$. The supercontinuum overlapped with the pump under an angle of $\alpha' = 3.8°$ outside the crystal to give an internal non-collinear angle in the crystal of $\alpha = 2.4°$. This angle has been referred to as the magic angle and is due to the dispersion of BBO. The projection of the idler on the signal beam is quite flat over a quite broad range.

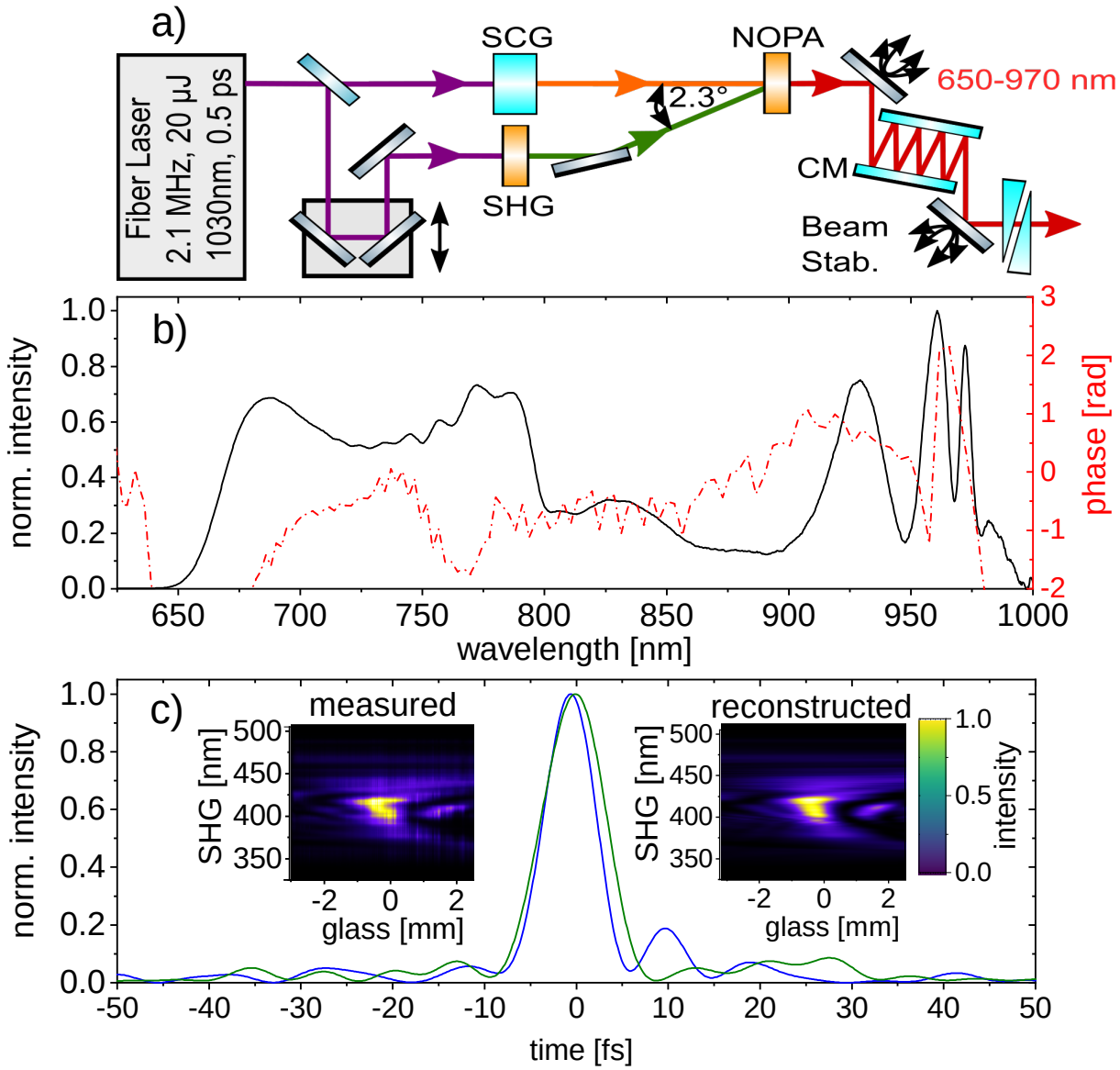

Figure 5.2: Generation of few-cycle NIR pulses: (a) Setup with the fiber-laser driven NOPA and pulse compression. (b) Spectrum of the NOPA output with 4.6 W (black). The spectral phase (red) was retrieved from a by D-scan measurement. (c) The temporal profile of the NIR pulse. The insets show the measured and reconstructed D-scan traces.

Different crystal lengths were tried. As expected from simulations, the 3.5 mm thick crystal produced the best results. A 3 mm crystal only produced half of the output power with a similar spectrum while a 4 mm BBO did not increase the available output power. This indicates that the amplification was already saturated.

Up to 2.5 μJ could be generated with a spectrum spanning from 650-970 nm, shown in Fig. 5.2(b). The shot-to-shot rms power stability of the NIR was as low as 0.4% with long-term (8 hours) power stability below 1% as can be seen in Fig. 5.3. To improve the pointing stability of the pulses, a beam pointing stabilizer (Aligna, TEM) was placed between the NOPA and the successive iDFG.

The NOPA was tested both in tangential and walk-off compensated configuration. In walk-off compensated configuration the seed is propagating with an increased phase-matching angle of $\phi_p + \alpha$ =24°+2.3°=26.3° which is close to the phase-matching angle for the second harmonic of the NOPA output. Therefore, a clear peak was observed at around 410 nm which made the output look visibly blue. This made it easy to distinguish the two phase-matching conditions. Due to the higher efficiency and the reduced parametric SHG, the tangential phase-matching condition was chosen in the following.

When adjusting the focal spot in a range from 10 cm before to about 10 cm behind the crystal by adjusting the recollimation mirror after the supercontinuum only minor changes of a few percent to the output power were observed and no changes in the spectrum. More importantly, a very similar spot size was observed in the far field that did not coincide with the focus position of the supercontinuum. This proves that the focal spot size and divergence are mostly determined by the pump beam and the OPA process and not by the seed itself, as was discussed in Chap. 2.

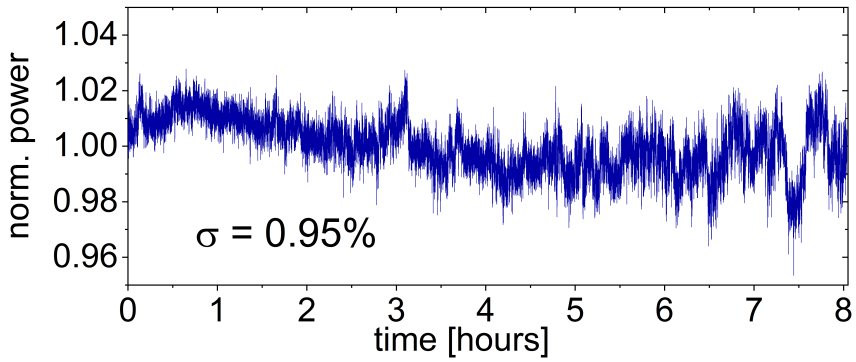

Figure 5.3: Long-term power stability measurement of the NOPA output.

5.2.4 Compression

To characterise the pulses, they were first compressed with a set of standard chirped mirrors. The phase was then characterised by a SHG d-scan. Based on the retrieved phase we could with support from V. Pervak design and fabricate a set of complementary special

chirped mirrors to compress the pulses. With 5 bounces from both chirped mirror pairs together with a pair of wedges we could compress the pulses to sub 7 fs. (see Fig. 5.2(c))

For the reflectometry setup, these pulses needed to be compressed at the iDFG, pump excitation focus and the EOS focus. To compress the pulses in all three positions, in each of these arm additional chirped mirror pairs were placed to compensate for elements in the beam as well as a pair of wedges to tune the dispersion. In the most relevant position of the EOS focus we could measure a pulse duration of 6.5 fs and in the pump excitation focus a duration of 8 fs by a d-scan measurement.

5.3 MIR generation

To generate a broadband MIR spectrum the choice of crystal is crucial as it determines the available spectrum and conversion efficiency. The most commonly used crystals in the visible and NIR region BBO and BiBO show strong absorption in the MIR region with absorption edges around 2.5 μm which renders them unusable. On the other hand, many MIR crystals such as AGS or GaSe absorb in the green part of the visible spectrum. As iDFG requires high intensities, two-photon absorption of the driving laser leads to permanent crystal damage, rendering these crystals also unusable.

For efficient MIR generation the idler needs to interacts with pump and seed components of the driving input pulse as well as and these two also need to interact with each other over the propagation length in the crystal. The temporal walk-off in the crystal between all three wavelength ranges should therefore be small. This is especially important due to the exponential build-up of the idler.

With these requirements, the choice of a ideal iDFG crystal can be considered. A commonly used crystal in this range is Lithium niobate. It is often used in OPAs can also be periodically poled which is then referred to as PPLN. A less known relative of this crystal is Lithium iodate ($LiIO_3$). Only very few, decade old publications could be found [142, 143] using this crystal for MIR generation. However, Lithium iodate offers excellent properties for the MIR range from $2-6\,\mu$m as will be discussed in the following. As the zero-dispersion point of $LiIO_3$ is at 2.1 μm the wavelengths of $\lambda_i = 4\,\mu$m and $\lambda_s = 1\,\mu$m, corresponding to pump wavelengths $\lambda_p = 800\ mathrmnm$, have the same group velocity. (The same holds true for $\lambda_i = 5\,\mu$m, λ_s800 nm and $\lambda_p = 690\,mathrmnm$.) Therefore, as discussed in Chap. 2, an input spectrum from 690-1000 nm process can produce a very broadband spectrum in an iDFG process. $LiIO_3$ also shows a very lower temporal walk-off between the beams. For example, it has a much lower temporal walk-off compared to LNB as can be seen in Fig. 5.3. This makes it an ideal crystal for the generation of low MIR wavelengths for our driving pulses.

In this crystal type-I phase matching has an order of magnitude higher effective nonlinearity $d_{\mathrm{eff,I}} \approx 1.65$ as well as broader phase-matching conditions compared to type-II phase-matching with $d_{\mathrm{eff,I}} \approx 0.08$. To use type-I phase-matching the polarization needed to be rotated to 45 degrees with respect to the optical axis of the crystal. This way, the projection of the longer wavelength components onto the ordinary axis served as the seed,

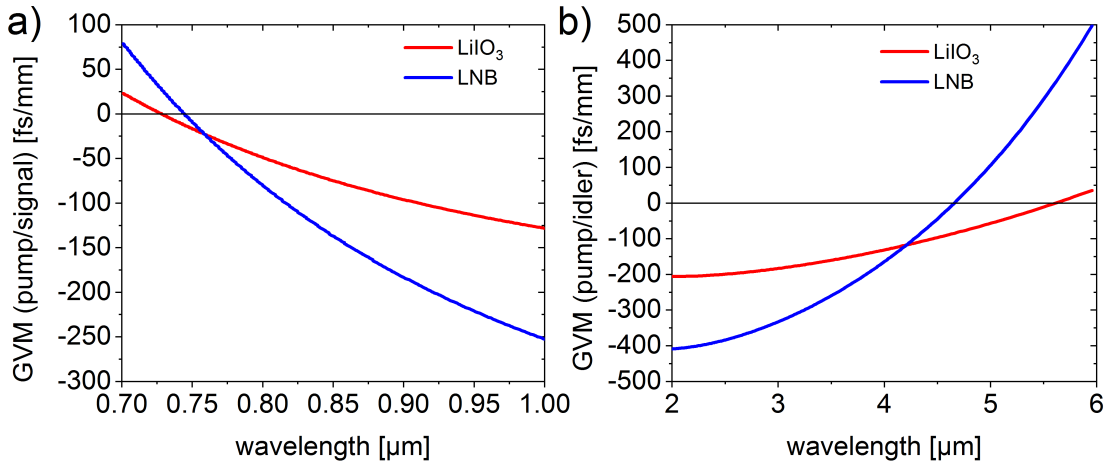

Figure 5.4: Group velocity mismatch between a pump at 700 nm and (a) the seed and (b) the idler wavelengths for Lithium iodate and Lithium niobabe.

while the projection of the shorter wavelengths components onto the extraordinary axis served as the pump beam for iDFG. Lithium iodate is also easy to commercially obtain as it was a commonly used crystal in the NIR (due to a broad amplification bandwidth from $1.2 - 1.6\,\mu$m when pumped by 800 nm Ti:Sa lasers. In this region it is now often replaced by Er:fiber lasers systems).

5.4 EOS

5.4.1 Working principle

Unlike EOS in the THz domain, the EOS in the MIR does not actually rely on the linear electro-optical Pockels effect but rather on sum frequency generation and therefor on a $\chi^{(2)}$ instead of a $\chi^{(3)}$ effect. (Alternatively, DFG could also be used for which the following points are just as valid. For reasons discussed later, in this work SFG was more beneficial.) The name of EOS is typically still kept as the rest of the technique and setup is identical to the one used in the THz domain, as is the scaling of the process with the gate and sampled beam intensities. In the EOS crystal, the sum frequency between the MIR pulse and a gate pulse with a temporally scanned delay are generated. This type-I sum frequency is orthogonally polarized to the gate pulse. Part of the sum frequency will spectrally overlap with the gate pulse. These components can be filtered with a bandpass filter and serve as a local oscillator in the next step. The gate pulse is only very weakly affected by the sum frequency with a much weaker MIR. The type-I sum frequency is orthogonally polarized to the gate pulse. The addition of the sum frequency therefore leads to a rotation of the local oscillator pulse. As the phase of the NIR is constant when temporally scanning it over MIR and the sum frequency scales as

$$E_1 exp(i\phi_1) * E_2 exp(i\phi_2) = E_1 E_2 exp(i\phi_1 + i\phi_2). \tag{5.2}$$

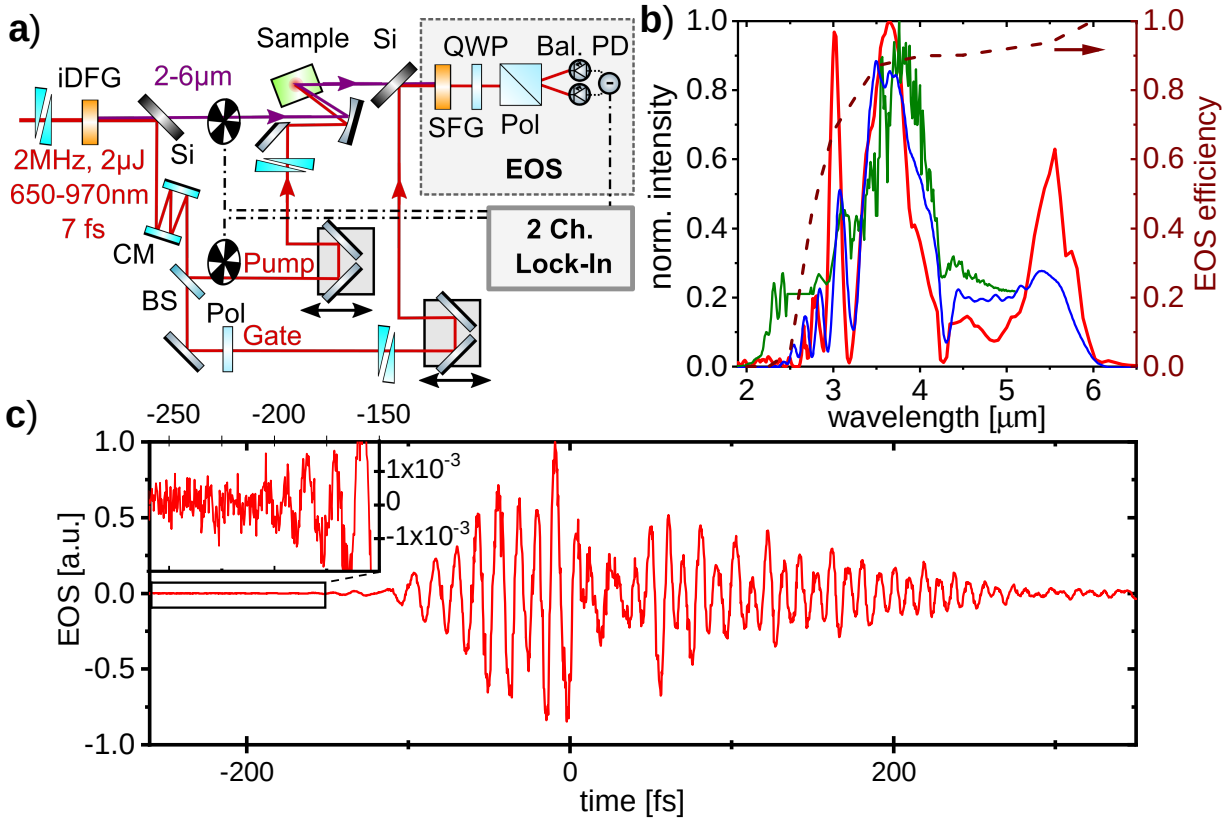

Figure 5.5: (a) Setup for transient field-resolved MIR reflectometry. HWP: half-wave plate, QWP: quarter-wave plate, BS: beam-splitter, Pol: polarizer, Si: silicon plate, CM: chirped mirrors. (b) MIR spectrum measured with EOS (red), up-conversion spectroscopy (blue) and commercial spectrometers (green; see SI for details). The dashed red line shows the simulated relative EOS response function. The dip at 4.2 μm is due to CO_2 absorption. (c) Electric field recorded by EOS. The inset shows the zoom on the field free early EOS signal to measurement the noise floor of less than 10^{-3}. Signals after 300 fs originate from the free-induction decay induced by absorption of CO_2 and $LiIO_3$.

We see that the phase of the sum frequency is proportional to the phase of the local phase of the MIR. In a simplified picture, the gate pulse needs to be shorter than at least one half-cycle of the MIR to not average over the maxima and minima of the field. As I will show later, this commonly stated requirement is not strictly true. The rotation of the local oscillator is then also proportional to the phase of the MIR. This is why this process is analogous to the electro-optic effect.

The polarization rotation can be detected by using a quarter waveplate to turn the polarization to circular when no MIR is present. The beam is then equally split into two beams by a Wollaston-prism polarizer. Each of this beams is send to one detectors of a balanced photodiode pair. The subtraction of the two photodiode signals cancels out noise sources that are common in both beams such as noise from the laser. Although it was possible to detect the rotation for strong MIR fields directly, the signal was quite weak compared to the noise. To increase the signal-to-noise ratio, a lock-in amplifier was used. For this modulation the MIR beam was chopped with a frequency f_0.

As seen in Fig. 5.5 (c) a low noise of the measurement of more than three orders on magnitude could be reached when comparing the noise of the pulse before the pulse with the field maximum. This noise essentially limits the minimal detectable changes induced by the pump and is therefore important to minimize.

5.4.2 Alignment and Optimization

To finding the temporal overlap in the EOS we could use that the excitation of charge carriers in a semiconductor changes it transmittance, similar to the effect we later studied in Chap. 5. As this effect has a much longer live-time than the MIR pulse duration it effectively offers a step-function response which made it easy to find the temporal overlap.

After the iDFG, the fundamental was filtered out with a silicon Brewster-plate of 1 mm thickness. The MIR could not be seen with silicon CCD cameras or with a non-thermal detector card. However, a beam was detected behind the silicon plate with both of these methods that was co-propagating with the MIR. This beam originated from the supercontinuum generation of the OPA described in Sec. 5.2.2. Although the main spectrum of the NOPA was blocked by the silicon plate, a weak fraction of the red side of the supercontinuum at about $1050 - 1100$ nm passed through the 1000 nm long-pass used to filter out the laser fundamental and got amplified by the NOPA as this spectral window is still within a amplification bandwidth. These components are at the absorption edge of the thin Silicon plate and therefore got partially transmitted. This could be used as a guiding beam for the MIR to establish the initial spacial overlap in the sample and EOS position with the respective NIR beam.

It was observed that the supercontinuum has a strong influence on the MIR output. By purposefully missaligning the supercontinuum position relative to the focus and thereby changing the output energy, spectral phase, a drop in MIR was observed. By changing the wedge pair in front of the setup most of this MIR power could be gained back. This however slightly increased the noise, as the increased noise of the supercontinuum coupled to the NOPA output and then to the iDFG. This indicates that the position of the filament

in the supercontinuum generation is of great importance as it influences the phase of the supercontinuum output and therefore changes the spectral phase of the pulse in the iDFG. As the filament position was strongly correlated with the noise, optimizing the supercontinuum on the point of highest stability could serve as a reproducible parameter to ensure stable parameters between and within a day.

The power over long times is quite stable as could be seen from Fig. 5.3. To improve the stability and avoid rare dips in laser power that were observed on occasion, a power stabilisation loop based on a AOM will be placed before the SCG.

5.5 Upconversion

While the EOS could reliably detect the MIR spectrum, the measurement time was to long to see fast changes. For example, to tune the spectrum and optimize different parameters affecting the iDFG, such as dispersion and spectrum of the NOPA output, a faster measurement method was beneficial.

Commercially available dispersion-based spectrometers such as PbSe spectrometers, i.e. spectrometers that do not rely on scanning like FTIR spectrometers, are limited to below 5 μm and could therefore not detect the entire spectrum. Therefore upconversion spectroscopy [144] was used as a fast method that also provided coverage of the entire bandwidth. In this nonlinear detection method the sum frequency of the MIR with parts of the narrow 1030 nm fiber laser output was generated. This shifted the spectrum in the region of 680-880 nm that could then easily be detected by a commercial Silicon-based spectrometer. The narrow-band laser provided good spectral resolution (about 15 nm in the MIR) and avoided spectral overlap of the weak upconversion with the fundamental spectrum. This technique relies on the linear scaling of the sum frequency intensity with respect to the MIR intensity $I(SFG) \propto I(MIR)$, making it well suitable to the detection. The narrow 1030 nm fundamental was reflected out by a polarizer used to regulated the power in the NOPA setup. It was delayed with a variable time difference to overlap with the MIR. A long delay of more than $6\,m$ was neede to compensate for the propagation length in the NOPA setup, the chirped mirror compressor and the propagation in the MIR setup.

Both beams were made parallel with a small separation to combine them without needing dichroic optics. THe beams were then focused by a spherical mirror with focal length of $f = 100$ mm resulting in a non-collinear angle between the beams. In the focus, a 0.2 mm thick $LiIO_3$ crystal was placed and the phase-matching angle was tuned to produce a broad spectrum that also resembled the detected EOS spectrum. The fundamental could be filtered out by a polarizer as the sum frequency is orthogonally polarized. Due to the non-collinar angle after the focusing the incoming beams and the $\vec{k}$-vector addition in the SFG, the upconversion was located between the fundamental and the MIR. This way, the SFG could be passed throug an aperture, blocking the two over beams. This was important to avoid saturation of the spectrometer by parasitic second harmonic of the fundamental that was much stronger than the upconversion.

5.6 MIR spectrum

With these techniques at hand we could now measure and compare the spectrum obtained by the EOS to the results from two commercial spectrometers. For the lower range, an extended InGaAs based spectrometer in the range of $0.9 - 2.5\mu$m was used and for the main parts of the spectrum PbSe-based spectrometer with a range of $1 - 5\,\mu$m was used. Although the latter could provide most of the spectral components, no spectrometer for the range above $5\,\mu$m was available. The PbSe-spectrometer also suffers from a quite limited dynamic range of about five. This is because the spectrometer has a noise floor under which no information about the spectrum was shown. unlike most spectrometers, this noise floor could not be subtracted. Therefore, the weaker parts of the spectrum could not be detected without saturating the spectrometer.

The EOS and upconversion show good quantitative agreement in the spectral range of $3 - 6\,\mu$m with each other and the spectrometer. This is most likely due to narrow phase-matching and the decision to tune the phase-matching bandwidth to the broadest possible output which permitted phase-matching the octave spanning spectrum. We could however tune the detection range of the upconversion to lower wavelengths and observe some components around $2\,\mu$m. The EOS could likewise be tuned to be more sensitive towards the $2\,\mu$m components. However this reaches the detection limit of the EOS due to the duration of the sampling pulse and the reduced broadband phase-matching in this spectral range. At the normal broadband condition, a small peak around $7\,\mu$m could be observed in the EOS spectrum. This peak is due to weaker absorption in this spectral range in the $LiIO_3$ crystal [145]. It also shows that the phase-matching bandwidth has not yet been fully reached, and that the long wavelength components are instead limited by the absorption in the generation and detection crystal.

5.7 Simulations

5.7.1 EOS efficiency

To better understand the limitations of the EOS efficiency, simulations for the sum frequency efficiency were performed. The results can be seen in Fig. 5.5 (b) (dashed red line, right axis). The simulations were based on the nonlinear optics simulation program SNLO. The efficiency of the EOS was calculated by comparing the relative sum frequency output for mixing the MIR frequency in question with a MIR wavelength so that the resulting SFG was at the center wavelength of the employed band-pass of $700nm$. The simulations used the k-vector miss-match calculated by a home-written program for a phase-matching angle of $\phi = 20.6$, for which the calculated small gain output spectrum agrees best with the measured spectrum. The SFG efficiency can be taken as the efficiency of the entire EOS detection, as the following projection of the polarization in the heterodyne detection scales linearly with the SFG signal. The simulation shows that the SFG efficiency is flat between the range of $3.5 - 6\,\mu$m but drops quite fast for lower wavelengths due to phase-

matching resulting in a $\Delta k > 20\frac{1}{\text{mm}}$. This shows that a lower wavelength detection range could in principle be achieved by changing the phase-matching angle of the EOS, but this would come at the cost detecting the main spectral range and would result in a lower bandwidth. Similar simulations were also performed for an EOS relying on DFG. This showed that the this process could cover the same range but with a slighly lower output of about $I_{DFG} = \frac{2}{3} I_{SFG}$, mostly due to the lower photon energy of the longer wavelength photons.

The flat spectral response function of the EOS explains the good agreement between the spectrum measured with EOS, upconversion spectroscopy and the spectrometer in the $3 - 6\,\mu$m range. It also explains that the components below $3\,\mu$m are underrepresented in the two nonlinear spectroscopy techniques due to limited phase-matching bandwidth. To extend the detection bandwidth, a thinner detection crystals could be used but would reduce the conversion efficiency and therefore the signal strength significantly, e.g. by a factor of about 3.5 in a halve as thick 0.1 mm crystal as was determined by simulations. Crystals below 0.2 mm thickness are also harder to procure and are typically not commercially available without a supporting substrate. Due to the high intensity in the detection crystal, a substrate would introduce non-linear phase distortions due to the B-integral onto the pulse. As this pulse was also used for heterodyn detection, a substrate could therefore distort the sensitive EOS detection. As we intend to measure relative changes in the experiment a quantitative agreement of the EOS measurement is sufficient. Likewise the octave broad spectral detection bandwidth is already quite remarkable, especially considering the high frequency range.

The other limitation for SFG efficiency comes from the available frequencies for the SFG what must be present for mixing and the band-pass filter used. To achieve a sum frequency in the filter wavelength of 700 nm, MIR wavelengths below $2.5\,\mu$m would require spectal componets above the red edge of the NIR spectrum of $970\,nm$ and can therefore not be converted. This range could by slightly extended to $2.0\,\mu$m by not using the filter but is then limited by the shortest wavelength in the NIR spectrum of $650\,nm$ as the gate and SFG need to interfere in the heterodyn detection. Using no filter or a filter which is on the edge of the spectrum might be more prone to fluctuations as the edge of the NOPA spectrum is less stable. As the cut-off from phase-matching and from the filtering are very similar, the detection bandwidth is not significantly affected by the chosen filter center frequency.

5.7.2 Dual lock-in technique

We have used an additional lock-in channel by also modulating the pump by a different in-commensurable frequency f_Δ, i.e. a frequency without a common denominator with respect to the MIR modulation frequency f_0. This allowed us to measure the changes to the electric field $E_\Delta(t)$ induced by the pump and at the same time measure the unaffected MIR field $E_0(t)$. This made the measurement less influenced by relative phase fluctuations originating from fluctuations in the relative path length of the beams as well as laser power fluctuations and their influence on the MIR generation.

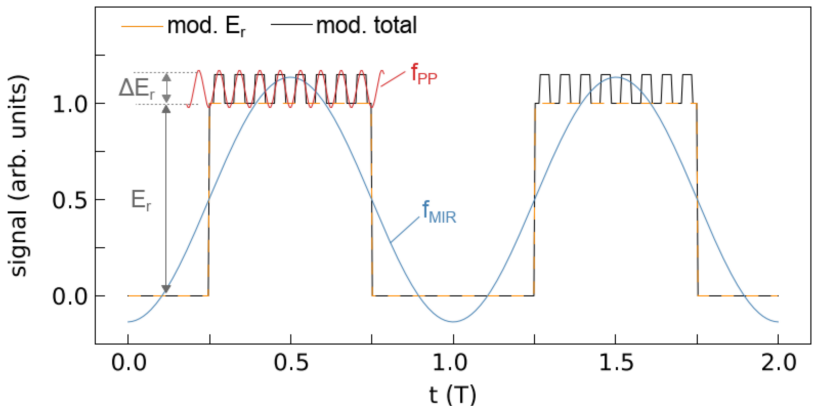

Figure 5.6: Schematic illustration of the dual-frequency demodulation approach. From [146].

The signal obtained by the dual lock-in technique can be described as

$$S(t) = a(t)\,(E_\mathrm{r} + b(t)\Delta E) \tag{5.3}$$

with the chopper modulation of the reference

$$a(t) = \frac{1}{2}\,(1 + \cos(\omega_\mathrm{MIR} t)) \tag{5.4}$$

and the pump-probe chopping

$$b(t) = \frac{1}{2}\,(1 + \cos(\omega_\mathrm{PP} t))\,. \tag{5.5}$$

We can then expand the signal to

$$\begin{aligned} S(t) = &\left(\frac{1}{2} + \frac{1}{2}\cos(\omega_{MIR} t)\right) \cdot \left(E_\mathrm{r} + \left(\frac{1}{2} + \frac{1}{2}\cos(\omega_\mathrm{MIR} t)\right) \cdot \Delta E_\mathrm{r}\right) = \\ &\frac{1}{2}E_\mathrm{r} + \frac{1}{4}\Delta E_\mathrm{r} + \underbrace{\frac{1}{2}(E_\mathrm{r} + \frac{1}{2}\Delta E_\mathrm{r})}_{S_\mathrm{MIR}} \cos(\omega_\mathrm{MIR} t) + \underbrace{\frac{1}{4}\Delta E_\mathrm{r}}_{S_\mathrm{PP}} \cos(\omega_{PP} t) \\ &+\frac{1}{4}\Delta E_\mathrm{r} \underbrace{\cos(\omega_\mathrm{MIR} t)\cos(\omega_\mathrm{PP} t)}_{\frac{1}{2}(\cos(\omega_\mathrm{MIR}-\omega_\mathrm{PP})+\cos(\omega_\mathrm{MIR}+\omega_\mathrm{PP}))} \end{aligned} \tag{5.6}$$

where the signals S_MIR and S_{PP} are filtered by the lock-in channel at the appropriate demodulation frequency, as each lock-in channel is only sensitive to signals modulated at this frequency. Then it follows that we have to adjust the measured signals slightly by $E_\mathrm{r} \propto S_\mathrm{MIR} - S_\mathrm{PP}$ and $\Delta E_\mathrm{r} \propto 2S_\mathrm{PP}$.

It is stated in the literature [147, 148], that for THz pulses longer than a single transient, artefacts might appear due to an uneven spectral response function. To better understand

this point with regards to the limitations for the dual lock-in techniques, simulations for of the sum frequency electric field used for the EOS were performed. In these simulations the ideal sum frequency between the temporally stretched MIR field and the NIR gate was calculated in the time domain. The delay of the NIR pulse was scanned to simulate the EOS delay. The temporal sum freuqency signal was transformed to the frequency domain by FFT and spectral components in a frequency range corresponding to the experimentally used band-pass filter were summed to obtain the simulated SFG signal. This signal was then plotted as a function of the NIR delay to obtain the simulated EOS trace. The actual heterodyning in the EOS was neglected in the simulations as these are mathematically trivial and would not effect the outcome. Under ideal conditions the simulated EOS reproduces the electric field perfectly.

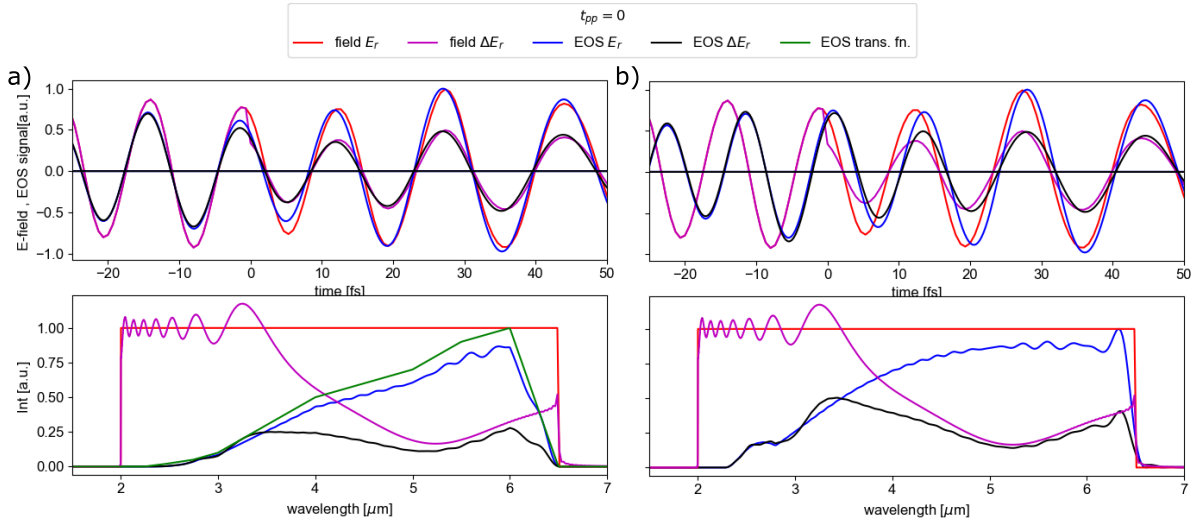

Figure 5.7: Simulations of EOS. The field for a broadband but stretched MIR spectrum (red) is shown above, the spectrum is shown below. ΔE_r (purple) shows the same field with a 0.5 reduced field for $t > 0$ to simulate an instantaneous reduction of the reflectively. The simulated sum frequency of the EOS of the $EOS\,E_\mathrm{r}$ (blue) and the of the pumped $EOS\,\Delta E_\mathrm{r}$ (black) are compared. (a) A strong EOS transfer function (green) with reduced efficiency for lower wavelengths. Only a slight difference between the real field and the EOS can be seen but the both EOS traces remain in phase. (b) EOS process with a flat transfer function but for a stretched NIR field of 40 fs^2. A temporally varying phase can be seen between MIR and EOS, while both EOS traces remain in phase.

From these simulation multiple lessons could be learned. The first effect we see is that the position of the spectral filter limits the detectable EOS wavelengths as discussed before to about 2.5 μm. Another important effect is related to the filter bandwidth. If the NIR field used as a gate is also stretched by applying a spectral phase to it, this leads to a reduced sensitivity towards higher NIR frequencies.However, the strength of this effect strongly depends on the spectral width of the filter. A more narrow filters allow a much

more elongated gate pulse. For a 680-720 nm filter (as used in the experiment) and a significantly chirped NIR pulse with a $GDD = 40fs^2$ resulting in a 20 fs pulse, only a moderate drop off could be seen that would still permit for signal to be recorded at all spectrally available MIR frequencies. This proves that the compression of the MIR pulse to a below a single cycle is not as crucial as sometimes claimed from the simple model that assumes that a pulse shorter than a half-cycle is needed to scan the NIR frequencies. It is more important that the pulse actually has the spectral bandwidth to enable the sum frequency to interfere with spectral components in the NIR pulse.

Another important lesson can be learned from this simulation regarding the benefit of dual lock-in technique for stretched MIR pulses. It is often stated in the literature [147, 148] that for THz pulses longer than a single transient, artefacts might appear due to an uneven spectral response function . Indeed we can see that if a non-flat response of the SFG is introduced: A time-dependent phase shift of the SFG with regards to the original MIR field can be seen in Fig. 5.7(b) To understand the effect of the pump on the EOS signal, I applied a instantaneous reduction reduction in MIR field (at t=0 in Fig. 5.7) to simulate a reduced reflectivity due to pump induced carriers. As can be seen in the figure, both the un-modulated $EOS\,E_{\mathrm{r}}$ and the EOS with the pump influence $EOS\,\Delta E_{\mathrm{r}}$ stay in phase. This shows that even if the MIR field is not accurately measured in the dual lock-in technique, the measurement of the phase difference between the two channels is not affected. The instantaneous response of the field is slightly smeared out. This effect however is on the order of an MIR cycle and therefore on the resolution due to the finite width of the pump pulse and therefore not of much concern. We could therefore verify that the shown comparative lock-in technique is an adequate tool to measure reflectometry data for temporally stretched MIR pulses. The technique can also work without taking the the often hard to accurately determine spectral response function of EOS into account. This lessens the requirement to compress the MIR or THz pulse to single cycle transients.

5.8 Setup improvements

The setup was constructed in two different iterations. After some initial measurements the entire setup including the laser was moved to a different lab. This offered an opportunity to implement certain improvements due to the experiences made with the setup and to discuss the differences and comparative advantages of different approaches.

During the second iteration the setup was placed in a vacuum chamber to to avoid the CO_2 absorption line around 4.2 μm in the middle of the spectrum as the absorption phase could disturb the phase-sensitive measurements.

A comparision of the setups can be seen in Fig 5.8. In the first iteration the entire laser power was focused into the generation crystal to achieve the highest MIR output. The reflected beam from the Brewster angle silicon plate was then split by a 50:50 beam-splitter. However, as the polarization of the beam was tuned to 45° for type-I phase-matching in the crystal, the beam suffered depolarization. This could be observed as the power transmitted through the polarizers for the s- polarised component required for phase-matching in the

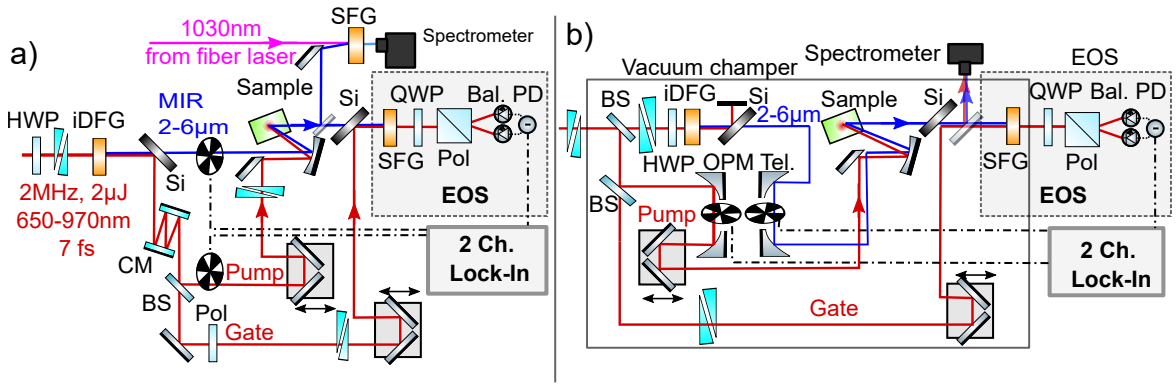

Figure 5.8: Comparison of the old setup version (a) to the improved setup (b). HWP: half-wave plate, QWP: quarter-wave plate, BS: beam-splitter, Pol: polarizer, Si: silicon plate, CM: chirped mirrors.

EOS crystal was less than the expected 50%, but rather about 10%. This most likely originated from the different phases retardation for the s- and p- components of the field occurring at the reflection on several mirrors. This can lead to a beam that is partially elliptically polarised. Additionally, the beam was affected by iDFG process in which it suffered depletion in the higher frequencies and gain in the lower frequencies as well as and some non-linear phase effects from the high intensity needed for iDFG. In the new setup we therefore decided to split the beam before rotating it to 45° by a beam-splitter which transmitted 80% for the MIR generation. The rest was then divided equally by a 50:50 beam-splitter for the sample excitation pump and the EOS gate. This also allowed for easier compression of each arm individually by a wedge pair. The compression of each beam could be measured in the focus of the sample for the pump, iDFG focus for the MIR generation pulse and the EOS crystal position for the gate pulse. We employed the D-scan method by scanning an additional common wedge pair and recording the second harmonic from a thin BBO crystal placed in the three foci.

In the first iteration the choppers for the MIR and pump needed to be placed in a collimated beam due to spatial restrictions on the setup and to keep the beam path as short as possible for better interferometric stability. The bigger beam did not just reduced the maximum chopping frequency, as blades with bigger gaps needed to be used. Maybe more importantly, the modulation was also not a perfect on-off response as the plate was moving through the beams.

Although the dynamic range of three orders of magnitude in the electric field could be still achieved in this way in the unmodified spectrum, which allowed us to perform initial measurements. We nevertheless tried to decrease the noise further. In the second iteration we therefore installed parabolic mirror telescopes in the MIR as well as in the pump arm to produce an intermediate focus. These needed to be well aligned as the off-axis parabolic mirrors can easily introduce aberrations in the beam.

The telescope for the MIR was set up with two parabolic mirrors, $f_1 = 50\,\mathrm{mm}$ and $f_2 = 150\,\mathrm{mm}$. However, as the input beam was defocused after the focus of the iDFG crystal,

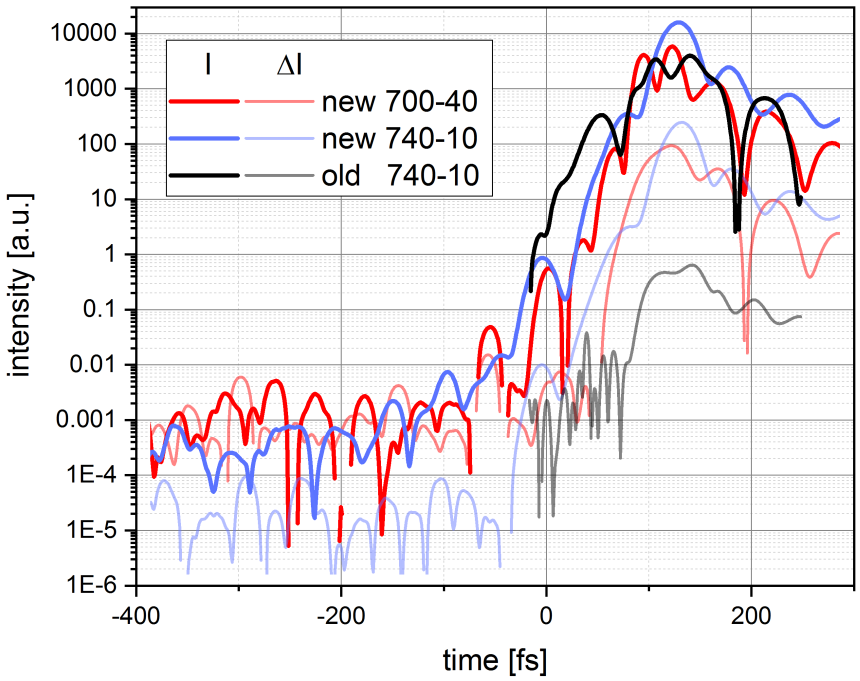

Figure 5.9: Instantanious intensity of the MIR field maxima at around t=100 fs compared to noise floor before the pulse. The bold lines indicate the reflected MIR field, the translucent curves the changes induced by the pump. EOS taken with a 10 nm broad filter around 740 nm (blue) is compared to the noise in the compared to a 40 nm broad filter around 700 nm (red) and to a measurements with the old setup (black).

the effective focal length was reduced to $f = 60\,\mathrm{mm}$, so that an effective magnification of $M = 2.5$ could be reached. The bigger MIR compared to the pump beam should lead to a reduced focus in the sample position and at least partially compensate the larger focal beam size due to the wavelength scaling of a focused Gaussian beam.

While in the first iteration the focusing on the sample was achieved by a spherical mirror. As the beams needed to still pass the sample, this required a longer focal length of $f = 100\,\mathrm{mm}$ to avoid aberrations. We first tried to avoid off-axis parabolic mirrors (OAPs) as these are very alignment sensitive. However, once the setup was properly aligned, no significant short- and long-term pointing drifts could be observed. This allowed us to align the OAPs without negative effects to be beam quality originating from beam drifts. We could then reduce the sample illuminating focal length to a 90° OAP with $f = 50\,\mathrm{mm}$ and reduce the pump beam size to $w = 20\,\mu\mathrm{m}$ which enabled a much higher pump fluence as well as a higher spatial resolution for future experiments.

In Fig. 5.9 we can see the influence of these changes. Both the maximum modulation by the pump (light blue curve) compared to the old setup (light black curve) could be increased by two orders of magnitude while the noise floor of the measurement could also be decreased by a similar amount. In the same graphic it can also seen, that the use of a more narrowband filter does decrease the noise floor of the more important pump modulated signal as was indicated by the simulations performed in the last Sec. 5.7.

5.9 Outlook and future improvements

While we have already set-up the MIR setup in a vacuum chamber to purge the setup of CO_2, not all of the measurements were performed under vacuum condition. If more pump power is needed to reach a higher fluence replacing the beam-splitter can be easily achieved by dividing the power between MIR generation or EOS gate differently. It should also be possible to frequency double the pump beam and therefore probe excitation at higher pump frequencies. In this case we could use the intermediate focus for the pump chopper wheel to reach an efficient SHG. Due to the high intensity reachable we can also potentially non-linearly excite potential targets as intensities of up to $I = 1\,\mathrm{TW/cm^2}$ could be reached with the improved setup version.

One possible way to increase the MIR signal is also to amplify the MIR by an NOPA. Simulations suggest that by using about 10W of the remaining power from the fiber laser gains in excess of a factor of 10 might be reachable in an 2 mm thick $LiIO_3$ crystal in a bandwidth of 3000-5500 nm. Using an NOPA angle of 3° coincides with the walk-off angle of the pump to ensure a good overlap between the pump and signal beams and thereby ensure efficient amplification.

However, with the current setup measurements on semiconductors could be performed, which will be the topic of the next chapter.

Chapter 6

Transient field-resolved spectroscopy of photoexcited semiconductors

The results presented in Sec. 6.2-6.4 have been published in [96].

As first demonstration of the capabilities of the reflectometry setup we performed measurements on two different semiconductors, gallium arsinide and germanuium. While gallium arsenide is a direct semiconductor, germanium is an indirect semiconductor. While in many publications the decay of the photo-excited carriers has been investigated, here we will make use of the few fs temporal resolution to focus on the lesser studied early dynamics directly following the excitation. At these times the carriers are not fully thermalized and non-equilibrium dynamics can be observed. At these early times we will see a different behavior originating from the different band-structures (direct vs. indirect.).

The spectral region of the probe light in the experiment is far away from the plasma frequency ω_{pl} associated with the free-carrier density at the employed pump intensities. Therefore, the variation of $\Delta r(\omega)$ across the spectral window of the MIR probe is smooth and does not contain the plasmon resonance peak. More importantly, our probe frequency region is also free of phonon absorption in semiconductors, which might affect the observed dynamics.

6.1 Theory

To understand the processes occurring in the sample we first need link the measured field changes from the field resolved reflectrometry to the carrier dynamics in the sample. Both the recorded EOS field traces of the unaffected field $E(t)$ and the field due to carrier excitation $\Delta E(t)$ are first transformed into the frequency domain by Fourier transformation. The complex ratio with the phase shift $e^{\mathrm{i}\Delta\phi(\omega)}$ between the two fields is directly linked to the change in reflectivity:

$$\frac{\Delta r(\omega)}{r(\omega)} = \frac{\Delta E_{\mathrm{r}}(\omega)}{E_{\mathrm{r}}(\omega)} = \left|\frac{\Delta E_{\mathrm{r}}(\omega)}{E_{\mathrm{r}}(\omega)}\right| e^{\mathrm{i}\Delta\phi(\omega)} \tag{6.1}$$

This change in reflectivity can be directly linked to the change in refractive index via the Fresnel equation for normal incidence $r = (1-n)/(1+n)$.

$$\Delta r = \frac{(n+\Delta n)-1}{(n+\Delta n)+1} = \frac{-2\Delta n}{(1+n)^2} \tag{6.2}$$

where n is the equilibrium refractive index and Δn is the change in refractive index induced by the pump. Further, the reflectivity ratio

$$\frac{\Delta r}{r} = -2\Delta n \frac{(n-1)}{(n+1)} \tag{6.3}$$

can be also linked to the change in electric permittivity $\Delta\epsilon_r$. It is linked to the refractive index by $\Delta\epsilon = (n+\Delta n)^2 - n^2 = 2n\Delta n + \Delta n^2$. We can then express the permittivity change purely as a function of the measured reflectivity and the equilibrium refractive index:

$$\Delta\epsilon_r = \frac{\Delta r}{r}\,\frac{n(n+1)}{2(n-1)} + \left(\frac{\Delta r}{r}\right)^2 \left(\frac{n+1}{2(n-1)}\right)^2 \tag{6.4}$$

For small changes in reflectivity, the second term can be neglected, and if dispersion is small, $\Delta r/r$ and $\Delta\epsilon$ are directly proportional .

The Drude model can describe the change in permittivity $\Delta\epsilon_r$ following the excitation of intraband charge carriers. Assuming the measured change in the refractive index arises from free-carrier dynamics the model is expressed as

$$\Delta\epsilon_k = \frac{-n_{\mathrm{fc,k}} \cdot e^2}{m_{\mathrm{eff,k}} \cdot \epsilon_0} \cdot \frac{1}{\omega^2 - i\omega\Gamma_k}, \tag{6.5}$$

with n_{fc} the free-carrier density, e the electron charge, m_{eff} the charge carrier effective mass, Γ the Drude scattering rate (i.e. momentum relaxation rate) in the corresponding band, and ϵ_0 the vacuum permittivity. The index k labels the band and for electrons, also the valley they are moving in. The pump induced carriers by far exceed the intrinsic carrier concentration. Then, by neglecting band gap renormalization, the total pump-induced change of the frequency-dependent dielectric function can be expressed as $\Delta\varepsilon(\omega, t_{\mathrm{PP}}) = \sum_k \Delta\varepsilon_k$, which will be dependent on the pump-probe delay t_{PP}.

We can also divide this Drude-term into real and imaginary part

$$\Delta\epsilon_k = \frac{-\omega_p^2}{\omega^2+\Gamma^2}\left(1 + i\frac{\Gamma}{\omega}\right). \tag{6.6}$$

When the scattering rate Γ is small, the real part $\mathrm{Re}(\epsilon) = -(\omega_p/\omega)^2$ and imaginary part $\mathrm{Im}(\epsilon) = -(\omega_p 2/\omega)^2(\Gamma/\omega)$ can be seperated. Using $\Delta r/r \propto \Delta\epsilon$ from the low excitation limit of Eq. 6.4, we gain the expression

$$\frac{\mathrm{Im}\big(\Delta r/r\big)}{\mathrm{Re}\big(\Delta r/r\big)} \approx \frac{\Gamma}{\omega}. \tag{6.7}$$

From this expression it can be intuitively seen how the phase of the reflected field $\phi \approx \Gamma/\omega$ is directly correlated to the scattering rate, making field resolved spectroscopy an ideal tool to observe scattering dynamics.

6.2 Results and discussion

To compare the two semiconductors, we took data consecutively with similar laser conditions and the same peak pump fluence of about $400\,\mu\mathrm{J/cm^2}$. After photoexcitation we observe a very similar decay dynamics in Ge and GaAs. By fitting a double exponential decay to the reflected intensity change $\Delta R/R \propto (1 - \exp(t_{\mathrm{rise}}) * \exp(t_{\mathrm{decay}}))$ we measure similar decay times of $t_{\mathrm{GaAs,decay}} = 16\,\mathrm{ps}$ and $t_{\mathrm{Ge,decay}} = 21\,\mathrm{ps}$. The decay time in Ge agrees to the one found by Yeh et al. [103] who have determined a decay time of $13 - 30\,\mathrm{ps}$ from bulk but $49 - 78\,\mathrm{ps}$ from the surface for a fluence of $67 - 202\,\mu\mathrm{J/cm^2}$ with a non-field sensitive measurement.

If we observe the rise time on the other hand shows an obvious difference between the two semiconductors. GaAs shows a much shorter rise time of $t_{\mathrm{GaAs,rise}} = 150\,\mathrm{fs}$ compared to $t_{\mathrm{Ge,rise}} = 1\,\mathrm{ps}$ in Ge. The origin of this as well as a more detailed investigation of these two behaviours will be discussed in the following.

6.3 Gallium Arsenide

The pump-probe delay time t_{PP} dependence of the transient reflectivity change in GaAs integrated over the spectral window $(3.5\text{-}6.4)\,\mu\mathrm{m}$, cf. Fig. 6.1 (a), displays a finite rise time of the signal with $\tau_{\mathrm{rise}} = 82\,\mathrm{fs}$ as fitted by a Fermi function. The delay shown here corresponds to a delay parallel to the diagonal $t = t_{\mathrm{pp}} - t_{\mathrm{EOS}}$ shown in Fig. 6.1(b) to compensate for the different pump arrival times for different MIR-field components [149]. A closer look at the spectral response of the signal (Fig. 6.1 (b)) at small pump delays ($t_{\mathrm{PP}} = 12\,\mathrm{fs}$) and somewhat larger delay ($t_{\mathrm{PP}} = 175\,\mathrm{fs}$), when the build-up is complete, reveals information on the temporal evolution of the response. It proceeds from an initially rather flat spectral response at short times to a Drude shape in the homogeneous approximation (Eq. 6.5). Overall, both spectra exhibit a smooth shape, as expected, with the exception of the sharp peak at $4.2\,\mu\mathrm{m}$ due to CO_2 absorption. The finite time response (Fig. 6.1(a)) directly reflects the buildup of a Drude-type free-carrier response upon NIR photoexcitation with an excited carrier density of $1.2 \cdot 10^{18}\mathrm{cm}^{-3}$ as determined from the Drude fit (cf. Fig. 6.1(b)).

The finite rise time of the Drude-type response in GaAs [150] has previously been reported by Huber et al. [108] in optical-pump-terahertz-probe (OPTP) experiments by monitoring the appearance of a plasmon resonance peak at different time delays in the THz region. They interpreted the rise as the buildup of dressed particles and the formation of Coulomb correlations in the photoexcited electron-hole plasma on a timescale of $70 - 100\,\mathrm{fs}$. This correlation time τ_{cor} was found to be somewhat larger than the plasmon oscillation period T_{pl}, $\tau_{\mathrm{cor}} \approx 1.6\,T_{\mathrm{pl}}$ and was theoretically explored using a non-equilibrium Green's function approach [109]. Our result for the rise time $t_{\mathrm{rise}} \approx 82\,\mathrm{fs}$ is slightly smaller than the reported value of τ_{cor}. Invoking the theory for the time-resolved build-up of structured

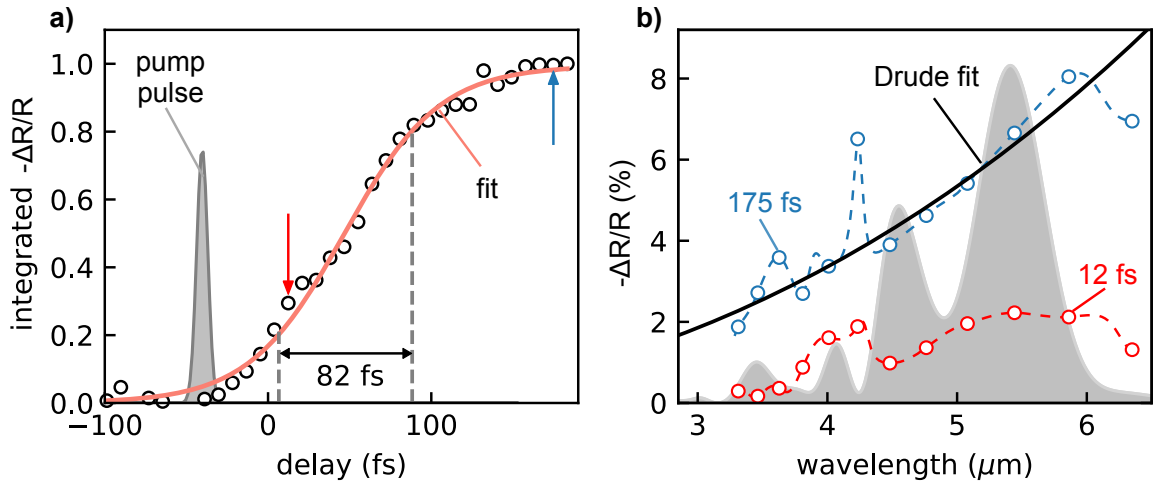

Figure 6.1: Buildup of the reflectivity from GaAs: (a) Normalized real part of the experimentally measured relative reflectivity change (dots) integrated over the wavelength range 3.5-6.4 μm and fitted to a Fermi function (red). Dashed lines indicate the rise time of 82 fs from 20% to 80% of the saturation level. (b) Wavelength-resolved real part of $\Delta r/r$ for a delay of 12 fs (red dots and dashed line) and 175 fs (blue dots and dashed line). For the latter delay the calculated Drude expression is also shown (black solid line) which yields an excited carrier density of $1.2 \cdot 10^{18}\mathrm{cm}^{-3}$ and a plasma oscillation period of $\sim$60 fs.

continua [151, 152] with frequency dependent probabilities

$$P(\omega,t)=\left|1+(i-q)\frac{\Gamma}{2}\frac{\exp[i(\omega_{\mathrm{pl}}-i\Gamma/2-\omega)t]-1}{\omega-(\omega_{\mathrm{pl}}-i\Gamma/2)}\right|^2 \tag{6.8}$$

(q: Fano asymmetry parameter), the rise time t_{rise} should, in the present case, be determined by the total decay width (or scattering rate Γ), $t_{\mathrm{rise}}=1/\Gamma$, rather than the plasmon period. Our result is, indeed, consistent with the Drude scattering time $\tau_s=85\,\mathrm{fs}$ found in [108]. We thus interpret the results of Fig. 6.1 as an experimental verification of the time resolved build-up of a structured continuum involving free carriers in a solid. Previously, the build-up of Fano-type resonances was only observed for atomic helium in the gas phase [153, 154].

6.4 Germanium

Different from GaAs, we observe the build-up of the changes in the reflectivity of Ge on a much longer time scale extending to ~ 3 ps (Fig. 6.2(a)). This can be understood in terms of the different band structures and, subsequently, the different charge carrier dynamics of the two samples. GaAs has a direct band gap where the NIR pump, in the range of $1.2-1.9\,\mathrm{eV}$, excites charge carriers from the top of the valence band into the bottom of the conduction band around the Γ-point. The photo-induced charge carriers are expected to scatter and to relax within this Γ-valley before recombining with the hole since other valleys, e.g. the L- and X-valleys lie at much higher band energies.

By contrast, Ge has an indirect band gap and the interband transition occurs away from the high symmetry valleys (Fig. 6.2(b)). Intervalley scattering of photo-excited electrons in the conduction band plays therefore a major role in the carrier dynamics on the femto- to picosecond time scale. Indeed, Monte-Carlo simulations [155, 156] reveal the contributions of scattering between Γ-, X- and L-valleys to the build-up of the reflectivity. The long rise time of the signal corresponds mostly to the conduction band filling of the L-valley within $(4-5)\,\mathrm{ps}$.

We could reproduce the rise of transient reflectivity by inserting the extracted time-dependent conduction band valley populations (Fig. 6.2(c)) with their transverse effective masses (see SI) into a sum of Drude terms (Eq. 6.5) of the Γ-, X- and L-valleys (Fig. 6.2(d)). Results agree qualitatively well with measured traces, except for the sharp peak at around 50 fs which results from the strong contribution of Γ-valley scattering. Overall, the different buildup behavior observed for GaAs and Ge can well be explained using the Drude-model when accounting for the different electrons' effective masses in different valleys. On much longer time scales, the relaxation processes in both GaAs and Ge behave identically, exhibiting a typical time constant of 20 ps for the data fitted up to 80 ps (inset of Fig. 6.2(a)).

Additional interesting insights can be gained from the separate observation of the time evolution of the imaginary and real parts of the relative reflectivity change $\Delta r/r$ as shown in Fig. 6.2(e). The magnitude of the real part (blue open dots) keeps rising after a sharp initial increase around $t_{\mathrm{pp}}=0$, while the imaginary part (red open dots) quickly flattens and even

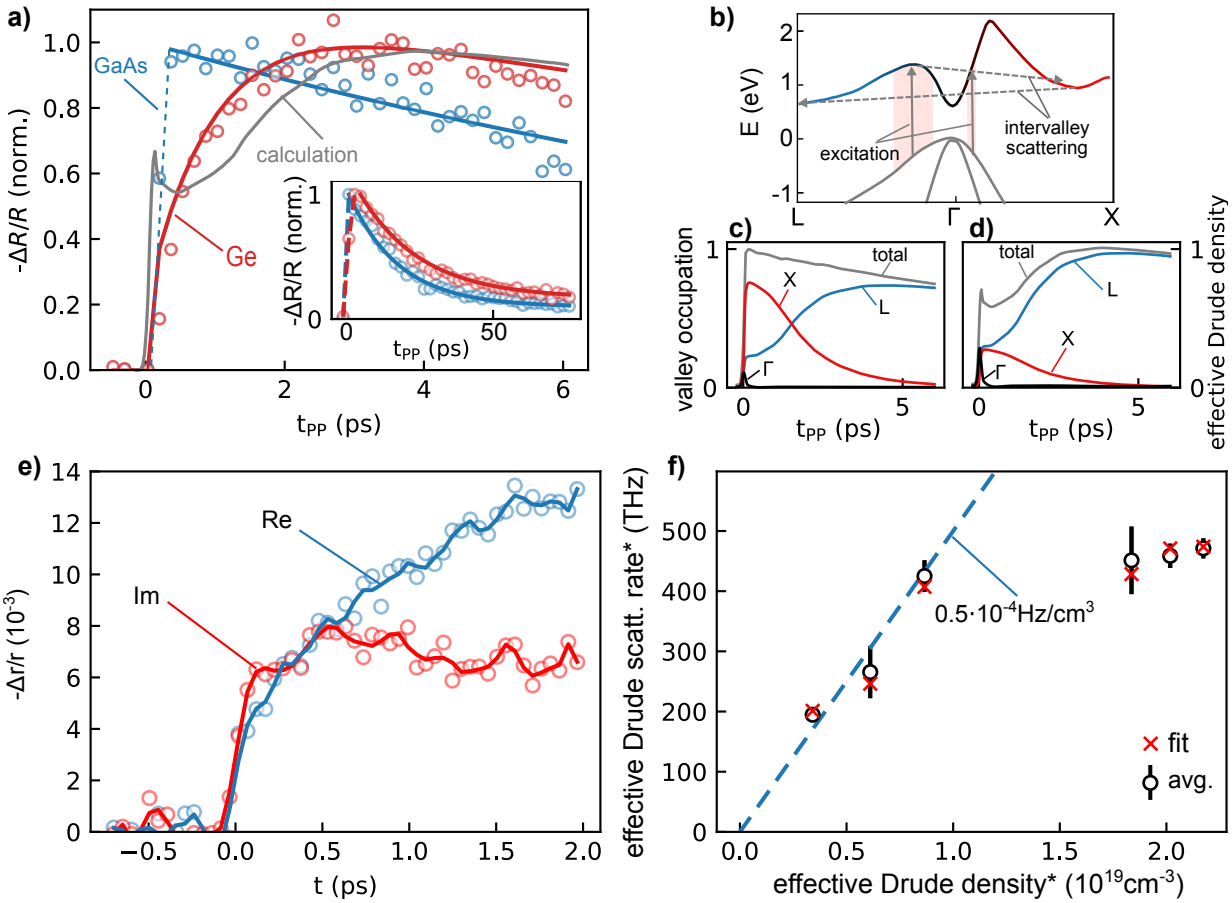

Figure 6.2: Intervalley scattering in Ge: (a) Normalized rise in reflectivity in Ge (red dots) compared to GaAs (blue dots). The black line shows the calculated Drude reflectivity change based on the evolution of the conduction band valley occupations simulated in Ref. [155] for an excitation with $\hbar\omega = 1.5\,\mathrm{eV}$ and the effective masses from Ref. [156]. Inset: long-term evolution with double-exponential fit. (b) Schematic overview of the excited electron dynamics in the band structure after photo-excitation. (c) Occupation of the individual conduction band valleys, extracted from Ref. [155] assuming a recombination time constant of 20 ps. (d) Individual valley contribution to the effective Drude density (carrier density divided by relative transverse effective mass) calculated from the valley occupation in (c). (e) Exemplary evolution of the real (blue) and imaginary parts (red) of the reflectivity change in Ge at 5 μm. (f) Dependence of effective Drude scattering rates on the Drude density obtained for individual wavelengths between $4.5 - 5.5\,\mu m$ (black bars) and from a Drude fit (red crosses).

starts to decrease after 500 fs of delay. Within the Drude model ratio between the imaginary and real parts of the reflection amplitude is according to to Eq. 6.7 proportinal to the scattering rate Γ. While the effective Drude density defined as the carrier density divided by the relative transverse effective mass n_k/m_k, and thus $\Delta r/r$, increases through intervalley scattering, the ratio in Eq.6.7 is initially approximately constant until the time-dependent effective scattering rate Γ starts to decrease after about 200 fs. At the high excitation densities of our experiment, carrier-carrier scattering is the major contribution[157, 158]. However, the scattering time also depends on the carrier distribution, since for carriers excited far above the band valley, carrier-phonon scattering is significantly increased[159]. The subsequently reduced Drude scattering rate arises from the decreased carrier-carrier interactions when the electrons are scattered into different valleys as well as the reduction of the carrier-phonon scattering as the excited carrier distribution thermalizes and relaxes.

The dependence of the Drude scattering on the excited carrier density and thus the carrier-carrier scattering rate can be probed by measurement of the pump-intensity dependence of Γ for varying pump-probe delays. The extracted Drude scattering rate for different free-carrier densities, evaluated at $t_{\mathrm{pp}} = 1.5\,\mathrm{ps}$, when most of the density is in the L-valley, is shown in Fig. 6.2(f). The Drude scattering rate increases linearly with the free-carrier density for densities $0.5 - 1 \cdot 10^{19}\mathrm{cm}^{-3}$, as indicated by the blue dashed line. At higher excitation density Γ appears to saturate which may be an indication of the reduced available final states for e-e, e-h, and h-h scattering [160]. The high scattering rates of the order of $\sim$ 100 THz, corresponding to a Drude scattering time of $\tau_s \approx 10$ fs, have also important implications for ultrafast strong-field processes in solids. Most prominently, the efficient generation of high-harmonics [90] in dielectrics involves the acceleration of a coherently driven electronic wavepacket in the conduction band and its eventual recombination with the hole. Electron-phonon and electron-electron (and hole) scattering is the main source for the decoherence of this process [161, 162]. Independent determination of Drude scattering rates from the complex reflection and transmission amplitudes thus promises novel insights into such decohering processes on the femtosecond scale.

6.5 Pump-fluence increase

As described in Sec. 5.8, the improved version of the reflectometry setup allowed for a smaller excitation beam diameter on the sample and therefore a 2 orders of magnitude higher pump fluence. Due to this fluences in the $20\,\mathrm{mJ/cm^2}$ range could be reached, by which a change into a different regime could be observed. By measuring the temporal reflection change in Ge on the ps time-scale for fluences from $4 - 22\,\mathrm{mJ/cm^2}$ can be seen in Fig.6.3. These data could also be taken with a purged setup so that the CO_2 absorption line was not present in the measured spectrum.

At the peak of the excitation at around 3 ps it can be seen in Fig. 6.4 that with increasing the fluence, at first both real and imaginary part become more negative as is expected from the Drude model. However, with even higher excitation, the real part changes behavior. First the real part for higher probing frequencies starts to increase

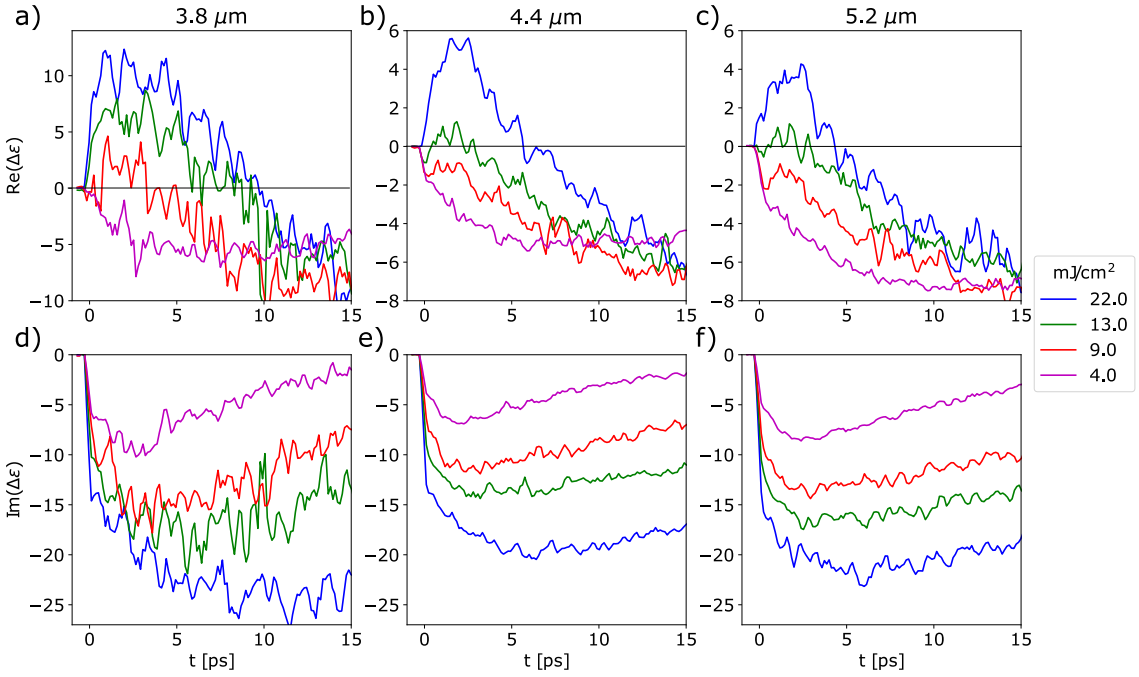

Figure 6.3: Temporal evolution of the real (a)-c)) and imaginary (d)-f)) part of $\Delta\epsilon$ for different probe wavelengths: 3.8 μm (a),(d); 4.4 μm (b),(e)) and 5.2 μm (c),(f)).

and become positive. For even higher fluences this then also happens for the lower probe energies. The imaginary part on the other hand just becomes more negative with increased fluence. This behavior is at odds with the Drude model, that according to Eq. 6.7 predicts a negative real and imaginary part that are proportional to the scattering rate Γ.

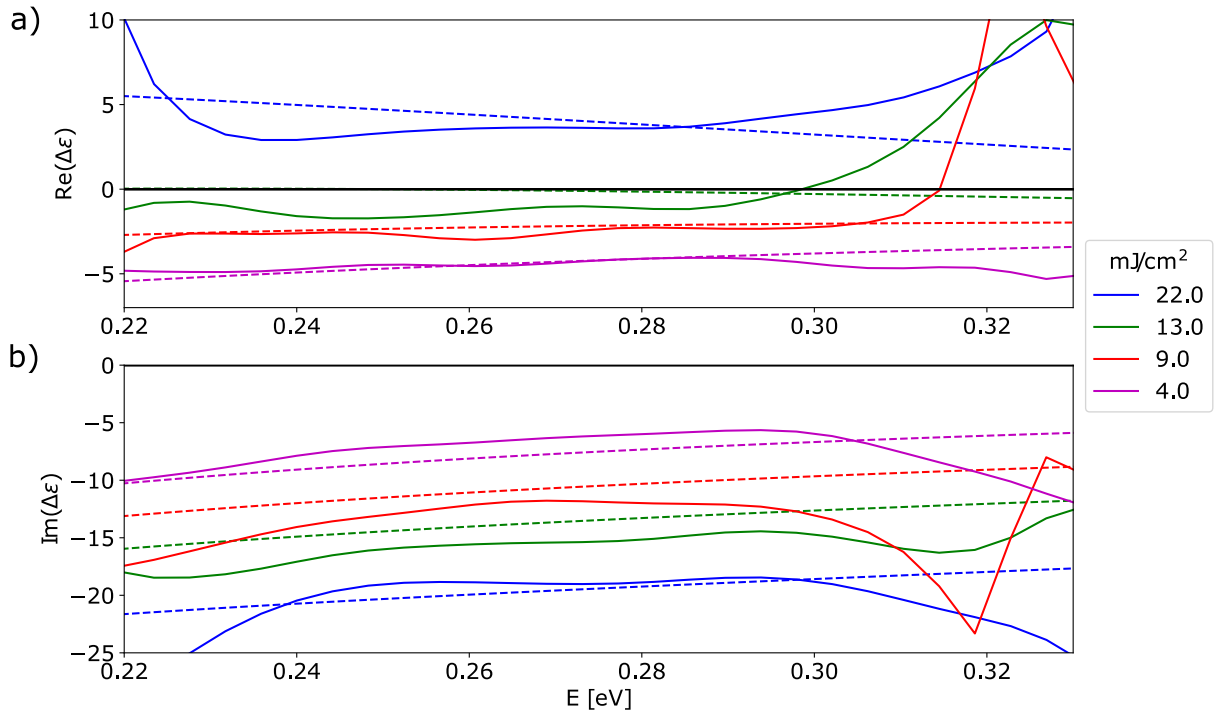

Figure 6.4: Measured real (a)) and imaginary (b)) part of $\Delta\epsilon$ (solid lines) dependent on the MIR photon energy $E = \hbar\omega_{\mathrm{MIR}}$ for different pump fluences for a pump delay of 3 ps. The dotted lines show the Drude-Lorenz model with $\hbar\omega_p = 0.85\,\mathrm{eV}$, $\hbar\omega_0 = 0.55\,\mathrm{eV}$, $\hbar\Gamma = 0.2\,\mathrm{eV}$, $\Gamma_L = 1.2\,\mathrm{eV}$. The coupling strength G_s of the Lorenz term is scaled linearly with the pump fluence.

However, extending the Drude model by adding a Lorenz-transition in a so called Drude-Lorenz model [103]

$$\Delta\epsilon = -\frac{\omega_p^2}{\omega^2 + i\omega\Gamma} - \frac{G_s\omega_p^2}{(\omega^2 - \omega_0^2) + i\omega\Gamma_L}, \tag{6.9}$$

can explain this behaviour, where G_d is the Lorenz coupling strength, ω_p the plasma freqency, ω the MIR-probe frequency, ω_0 the Lorenz-resonance frequency, Γ and Γ_L the free and Lorenz damping terms. This model can quantitatively explain the observed behavior as is shown in 6.4. Good agreement with the data could be achieved by assuming that the

oscillation strength of the Lorenz term is proportional to the pump fluence but keeping the other parameters including the plasma frequency and scattering rate constant for a certain pump-probe delay. This indicates that the excited electron number might be saturated as we have already seen signs of in Fig. 6.1 (f). A similar behavior could be observed for all time points. The Lorenz resonance frequency seams to decrease from $\hbar\omega_{0,3ps} = 0.55\,\mathrm{eV}$ at $t = 3\,\mathrm{ps}$ towards the later times around $t = 15\,\mathrm{ps}$ to about $\hbar\omega_{0,15ps} = 0.3\,\mathrm{eV}$ which is within the observed spectral range. This explains that $\mathrm{Re}(\Delta\epsilon)$ is independent of the pump fluence at these later times.

Carrier diffusion effects are neglected here. Due to the short timescales at which the initial rise of the real part is observed, these effects should not play a dominant role for this behavior, but might affect the measurement in some way. This might explain why the model only describes the observed behavior in a quantitative fashion.

An additional feature that can be observed is the appearance of a fast rising component, on a few fs time-scale, much shorter timescale than observed in Fig. 6.2. To better understand this, a scan of the first few hundred picoseconds was performed at different fluences. For the highest pump fluence this is shown in Fig. 6.5 (a) and (b). After adjusting for the pump moving through the probe pulse, as described for the GaAs-Data, a short rise-time of about 30 fs can be observed.

Above an energy of 0.3 eV or below 4200 nm, oscillations in the real and imaginary reflectivity curves can be seen in Fig. 6.5 (c) and (d). A Fourier-transformation of the reflectivity along the adjusted pump-probe delay τ revealed oscillation frequencies of 80, 50,33 and 26 fs. These correspond to energies of 50, 80, 125 and 160 meV . For lower fluences similar oscillation frequencies can be seen, but with reduced oscillation strength. A first candidate for these oscillations are phonons. However, phonon energies in Ge are typically reported to be below 40 meV [163]. The interpretation is however complicated, as multi-photon excitation by the pump beam into higher bands become possible due to the high intensity of the pump beam approaching the $\mathrm{TW/cm^2}$ range. The origin of these oscillations is therefore not yet understood.

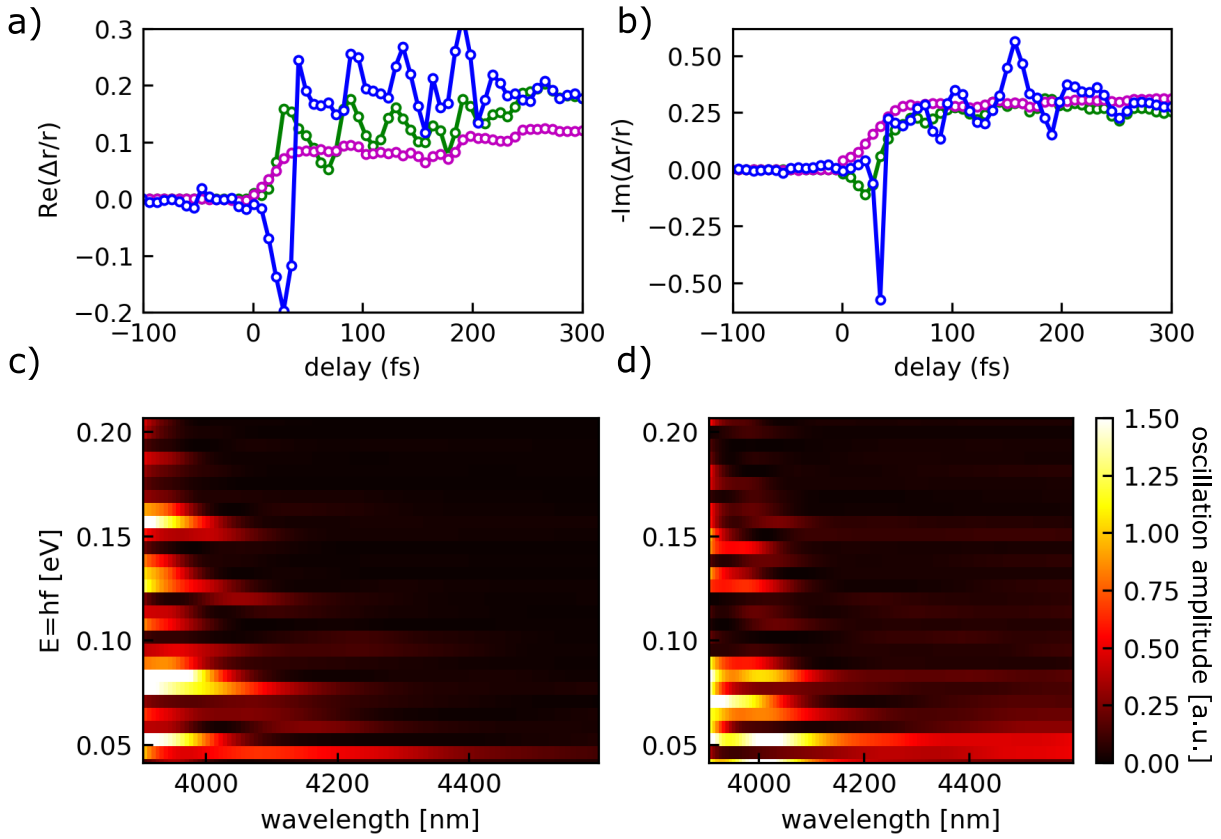

Figure 6.5: The measured temporal evolution of the first femtosecond of the real (a)) and imaginary (b)) part of relative reflectivity change. The data is taken at a high pump fluence of 22mJ/cm^2. The lines correspond to different spectral ranges: 3.8-4.0 μm (blue); 4.0-4.2 μm (green) and 4.3-5.0 μm (magenta). For the real (c) and imaginary part (d) for each probed wavelength (x-axis) the Fourier-transformation is performed along the pump-probe delay.

Chapter 7

Conclusion

In this thesis I have demonstrated how OPCPA systems can be used to generate CEP-stable MIR pulses with up to octave wide spectra or multiple Watts of output power. I also showed how these can be used to probe solid state systems in novel ways, among other applications.

First, I introduced the theory of OPA and DFG processes, to then discuss different methods to amplify a broadband spectrum in an OPA. I pointed out some often neglected aspects of OPA systems, such as how the pump predominantly affects the output beam profile and how longer crystals do not limit the bandwidth as much as often stated. I also discussed design considerations for an OPCPA system for these broadband pulses. We could thus see how narrowband lasers and OPAs can be used together with other parametric processes to transform a (sub-)picosecond pulse into a broadband femtosecond pulse in the NIR, SWIR or MIR which was used as described in the following chapters.

I have then demonstrated how these principles can be implemented in a state-of-the art SWIR laser system with a half-octave spanning spectrum around $2\,\mu$m for strong-field applications. This CEP-stable system reached down to 16 fs pulses. The high average power of the system required a careful testing and discussion of multiple crystals. We could see that BiBO resulted in the most stable output conditions and reach pulse energies in the $100\,\mu$J range corresponding to average powers of 10 W.

We have seen, that the high intensity of the resulting pulses could generate HHGs in silicon and drive up to the 9th harmonic within the non-perturbative regime. The high repetition rate of the system enabled to perform multi-dimensional scans of the harmonic which was used to study the driver ellipticity and sample orientation dependence of the harmonics. This highlighted the difference between harmonics below and above the semiconductor band gap.

The increased repetition rate has two consequences. On the one hand we have seen that the increased statistics helped in many experiments, where the improved statistics made it possible to perform them in the first place. If the data collection takes multiple hours, an order of magnitude in signal-to-noise ratio would then require to keep the conditions not just of the laser but also the sample identical over the span of days. This however is not always possible. On the other hand, for some applications higher intensity would

be beneficial, such as HHG in gases. In such applications either more laser power or a lower repetition rate and therefore a higher pulse energy is needed. As the systems developed within this thesis are pushing the limits in terms of high average powers, for such applications a lower repetition rate would be beneficial. Due to the inherent pulse energy scalability of OPCPA systems, the here presented system can be a stepping-stone for such systems with higher pulse energies.

To make better use of the CEP-stability of the SWIR system, one of the most challenging aspects was to run the f-2f interferometer on a reliable basis. This is mostly due to the sensitive nature of the broadening required for the less than octave wide spectrum. This might be overcome in the future by using higher harmonic orders such as in a 3-4f interferometer. In some applications we found out, that a combination of the laser with its second harmonic [76] provides good control over the field so that CEP-control is not always needed for field-controlled measurements.

The second system was able to generate an octave spanning spectrum in the lower MIR range from 3-6 μm or 50-100 THz. In this case, the system provided inherently CEP-stable MIR pulses from the iDFG process. We used the short near-infrared pulses to measure the MIR field by electro-optical sampling. This field-sensitive measurement enabled measuring the changes induced by an ultrashort NIR pulse in semiconductors. The setup offered few femtosecond temporal resolution combined with the ability to separate changes to real and imaginary part of the reflectivity and thereby also changes in the dielectric properties of the material.

Using two choppers for a double-login detection scheme proved very beneficial at these higher MIR frequencies. It enabled simultaneous detection of MIR fields and the changes induced to the field simultaneously. This made the measurement more reliable as it reduced the effects of slow drifts that occur over the recording time of the two-dimensional scans necessary for spectral-temporal measurements. Furthermore, while in the THz domain single cycle transients are commonly created, for an octave wide spectrum in the MIR, this is more challenging due to higher order phases from materials and the technical necessity to avoid long beam paths, that a compression by multiple chirped mirrors would introduce. The presented method however made it possible to record changes in the 10 fs range by avoiding field distortion effects from an uneven spectral response of the EOS. As both signals could be measured by the same EOS setup such effects could be avoided, as could also be confirmed by simulations.

I could show that with these new capabilities, we could gain new insights into photo-excited semiconductors, materials that have been studied for a long time. In one of the applications, transient reflectometry could be pushed to higher frequencies, enabling direct access to the early scattering dynamics under high carrier densities. I could also make use of the state-off-the art temporal resolution to study fast initial termalization in these systems. Due to the lower repetition rate compared to oscillator systems, we could make use of the increased pump fluence and thereby investigate Ge in a previously not accessible regime. All of these features will be quite useful when using the system in probing novel materials, such as TMDs, materials with quantum confinement or organic materials for which the extended wavelength range might be very promising.

In the future, it should also be possible to further amplify the broadband spectrum in the mid-infrared. This could enable to simultaneously measure the strong-field effects by techniques such as HHG or electron spectroscopy and simultaneously record the changes to the driving pulse in a field-resolved manner and thereby combining the advantages of the different techniques.

Appendix A

FLIM microscopy

The NOPA laser system introduced in Sec. 5.2 was also intended to be used for multi-modal microscopy for which it has the correct wavelengths and bandwidth. It can be used for two-photon excited fluorescence (TPEF) in many biological autofluorophores such as the metabolic cofactors NADH and FAD [164] as well as for samples with fluorescence labels. It also is broad enough to serve as both pump and Stokes beam in coherent Raman techniques, such as coherent anti-Stokes Raman spectroscopy (CARS) or stimulated Raman scattering (SRS). In these, it could be used for the detection of C-H stretch modes around $3000\,\mathrm{cm}^{-1}$ as well as the lower frequency fingerprint region [165]. The laser would therefore be an useful excitation source for multi-modal microscopy.

Two M.Sc. thesis projects under my co-supervision were performed to advance the microscopy setup [166, 167]. An Olympus IX 73 microscope with costum build optical paths was used. Using a 100x air objective with a $NA = 0.85$ we could achieve a diffraction limited spot size $1.2\,\mu$m while a vertical resolution around $2\,\mu$m could be reached. Using TPEF by the NOPA output, signal from fluorescent nanobeads were recorded. To gain a better signal-to-noise ratio, a custom built detection system based on PMTs (photo multiplier tubes) was set up as well as a fast galvanic-mirror scanning system.

However, as the microscopy setup was not fully operational until the end of this thesis, I performed microscopic experiments using fluorescence lifetime imaging (FLIM) [168–170] in collaboration with the Popp group in Jena. These experiments focused on X-ray radiation effects on cancer cells.

Fibroblast cells are reported to have an effect on irradiation therapy [171] in cancer treatment. To better understand these effects, we studied the effects of x-ray irradition on the metabolism of cancer and fibroblast cells and the related effects of oxidative stress.

A.1 OPO and microscopy setup

The laser used for these experiments at the University Jena was a Ti:Sa oscillator at 832 nm (Mira HP) at a repetition rate of 76 MHz and a pulse duration of 2-3 ps. Parts of the Ti:Sa oscillator were frequency doubled and used to pump an optical parametric oscillator

(OPO). The output can in principle be tuned between 500-1600 nm. For our experiments, this served as excitation TPEF and CARS pump beam, whereas the Ti:Sa fundamental was used as the Stokes beam. It was therefore tuned to a wavelength around 672 nm for an energy difference to the Ti:Sa laser 2850 cm^{-1}. This energy difference is resonant with the C-H stretch mode. The resulting CARS signal can then be detected around 564 nm. Here, CARS was primarily used to detect the presence of cells. More importantly for the results presented here, the OPO served as a TPEF excitation for NADH and FAD as the doubled frequency/half wavelength of 366 nm overlaps with the excitation for these two metabolic cofactors. For the FLIM images therefore only the OPO beam was used.

The beams were focused onto the sample with a 40x oil immersion apo-chromat objective with an numerical aperture of NA = 1.1. For the FLIM metabolic imaging data we used $150 * 150\,\mu m$ large images with 0.29 μm (512*512 pixel).

A.2 Cell preparation

The cell line preparations was performed by Jia Mei [172]. The following description of cell preparation is taken from her PhD thesis:

"2D cultures were passaged 1-3 x per week to keep, depending on growth rate. After a microscopic check of the cell status, old medium was removed and cells were washed with PBS. Then 1 mL Trypsin/ EDTA was added to T25 flasks and 2 mL to cell culture dishes. Samples were incubated in a 37°C incubator for 5 minutes to detach the cells and complete detachment was verified microscopically after knocking sharply against the side of the dish or flask, respectively. To stop trypsinization, a 10-fold volume of fresh medium + FBS was added and cell clusters were dispersed by pipetting the cells up and down several times with a glass pipet. Then, according to the split ratio (mostly 1:5 or 1:3), a fraction of the cell suspension was transferred to a new labeled flask or dish. Culture medium was added up to 10 mL for dishes and 5 mL for T25 flasks. Dishes and flasks were gently moved to evenly distribute the cells before they were moved to the CO2 incubator (5 % or 10 % CO2, depending on cell lines).

...

To generate cell line MCF-7 (HGMU) pMcc-GFP-53BP1-PN #L, one day before transfection, 180 000 cells/ well were seeded in 2 mL medium without Pen/Strep into 6-well plates to ensure 50 % to 70 % confluence for transfection. On the next day, 7.5 μl lipofectamineTM 2000 was added to 125 μl Opti-MEM in a safe- lock tube and mixed by pipetting. 5 μg plasmid pMcc-GFP-53BP1-PN was added to 125 μl Opti-MEM in another safe-lock tube, mixed by pipetting and incubated for 5 min. The DNA-lipid complex was prepared by mixing both vials and incubating at room temperature for 15 min. The DNA-lipid-complex was then pipetted on top of the medium and the sample was incubated overnight in a CO_2 incubator. On the next day, the medium was removed and the cells were gently washed with PBS buffer. The 500 μl Trypsin/ EDTA were added to each well and samples were incubated for 5 minutes at 37 °C to detach the cells. After washing and counting, 1 % and 10 % of the cells, respectively, were transferred to new 100 mm x 20

mm dishes with 10 mL fresh RPMI-1640 + 10 % FBS containing 0.3 μg/ mL puromycin for selection. Cells were incubated for at least two weeks in order to kill untransfected cells, with refreshing the puromycin-containing medium every 3-4 days. After colonies of puromycine- resistant cells have formed, they are individually harvested by adding a small drop of trypsin on the top of colony and incubating for 5 min. By pipetting up and down with 10 μl cell culture medium each colony was transferred to one single well of a 24-well plate. After adding 1 mL cell culture medium with 0.3 μg/ mL puromycin, the colonies were incubated to expand and finally tested by fluorescence microscopy for expression of the fluorophore-tagged transgene. Three successful clones were generated, of which #L was used in the experiments."

A.3 Image analysis

As the oxidized form of NADH does not fluoresce, nor does the reduced form of FAD, the comparision of these two components is taken as a proxy for the redox state of these metabolic cofactors and thereby allows to infer the metabolic state of the cell [164, 173, 174].

The cells show two distinctly separate areas, the nucleus and the cytoplasma. While the nucleus is important for radiation induced cell damage to DNA, here we focus on the metabolic cofactors NADH and FAD which are linked to mitochondria which are placed inside the cytoplasma. Due to this fact, the cytoplasma also showed a stronger signal from NADH and FAD. This fact could also be used to differentiate between the two areas by applying a 2D Fourier filter to the images and filtering for stronger signal. The threshold was set to rather slightly under-represent the cytoplasm but to make sure that the selected areas are in the cytoplasma. This method is much less subjective then using custom selected areas.

From the data taken, we could retrieve three different parameters. The first is the metabolic ratio [173–175], which we can express as the relative signal from the 458 ± 20 nm filter for NADH S_{NADH} and the signal through the 525 ± 20 nm filter for FAD S_{FAD} which can then be calculated as

$$R = \frac{S_{\mathrm{NADH}}}{S_{\mathrm{NADH}} + S_{\mathrm{FAD}}} = 1 - \frac{S_{\mathrm{FAD}}}{S_{\mathrm{NADH}} + S_{\mathrm{FAD}}}. \tag{A.1}$$

As part of the signal from FAD is emitted in the NADH filter range, it does not provide an absolute but qualitative value quantifying the relative abundance of reduced cofactors. An increase in this factor can be linked to an increase in metabolic activity.

The other parameters originate from the FLIM retrieval. The images here analysed with a FLIM image software SPCimage from Becker+Hickel [176]. Within this software, the lifetime of the fluorescence was fitted with a double-exponential decay convoluted with the instrument response function. Using more than two exponentials showed signs of over-fitting as the third component varied significantly with different fitting parameters.

It is known that by recording NADH the long lifetime component corresponds to protein bound NADH and the short lifetime component to free NADH [175]. From the longer lifetime, the lifetime of the not protein bound NADH can be linked to the ratio of NAD(P)H that is phosphorylated. This ratio of NADPH to NADH was reported by Blacker et al. [177] to be linked to the longer livetime T_2 by

$$\frac{\text{NADPH}}{\text{NADH}} = \frac{t_2 - 1.5\,\text{ns}}{4.4\,\text{ns} - t_2}. \tag{A.2}$$

Similar to the procedure described in [177, 178] we fitted a double exponential decay to the data. To increase the reliability of this fit, multiple pixels needed to be binned together.

Sample pictures of the retrieved parameters can be seen in Fig. A.1. We could observe, that the variation of the parameters within sample was quite homogeneous. However, the deviation between different samples or sample positions was much pronounced. To compare the values between irradiated samples and unirradiated control samples, all pixel values from different sample positions were averaged and the standard deviation of these values was calculated. The predominant part of the standard deviation originated from the difference between different sample positions rather than from the variation within the cells or one sample position.

A.4 Results

By analysing the data, we see that the three previously mentioned parameters change over time. We observe that the parameters change in the non-irradiated control group shown in Fig. A.2 (a)-(c). However the samples that were irradiated by 15 Gy of x-rays show changes that significantly deviate from the control group. The behaviour in the cytoplasma agrees very well with the behaviour of the entire cell. This is not surprising, as the cytoplasm is the place where most metabolic reactions occur. By analysing the difference between the irradiated cells to the control samples in A.2 (d), we observe a very similar behavior in the two cell lines. The metabolic ratio, fraction of protein bound and phosphorylated NADH also show that all ratios change in a correlated way. After short timescales of 10 min only a slight decrease is observed. After 2 hours an increase in the parameters is visible but reverses after about 24 hours. The data after 48 hours is somewhat unreliable, does not show a continuation of this trend. In all cases, the relative changes are much stronger in the phosphorylation ratio than in the other two measurements.

A.5 Discussion

The combination of the behaviour of the three metabolic parameters indicates that the change is predominantly in phoshorilated NADP. NADPH is a major factor of the cell to battle reactive oxygen species by glutathione [177, 179]. The increase after few hours is an

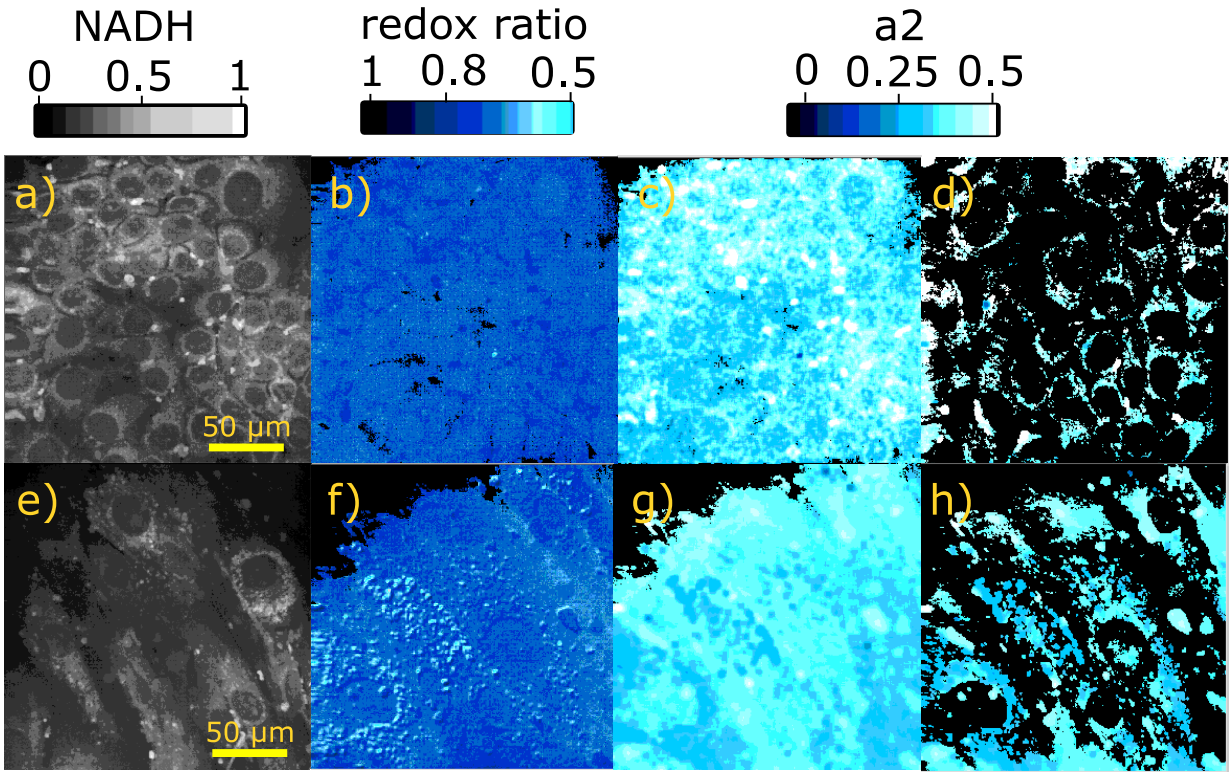

Figure A.1: Sample pictures from multimodal microscopy. a)-d) MCF7 cells and e)-h) BJ1 fibroblast cells, both 2h after irradiaiton with 15 Gy. a),e) NADH flourescence signal, b),f) NADH redox ratio ,c),g) protein bound ratio and d),h) filtered for cytoplasm for the protein bound ratio.

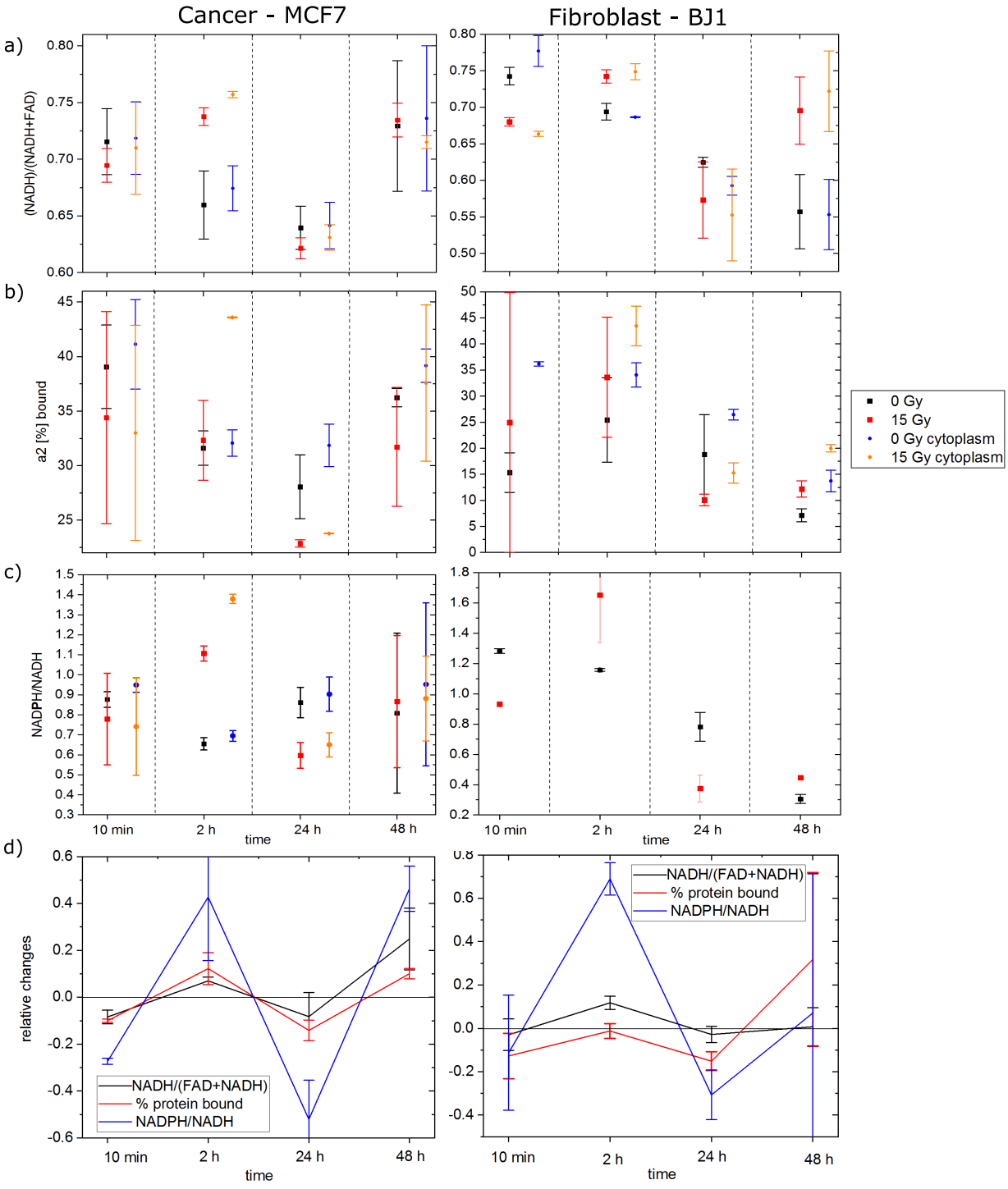

Figure A.2: a) Changes in metabolic parameters for unirradiated cells (0 Gy) and after 15 Gy of irradiation after different time points of irradiation. Results from MCF7 are on the left, from BJ1 on the right. Results averaged over the whole cell and just the cytoplasm are shown with left/right offset. a) Metabolic ratio. b) Percentage of protein bound NAD(P)H from percentage of the long lifetime component a_2. c) Phosphorisation ratio of NAD(P)H from the lifetime of the protein bound components. d) Relative changes $S_{15Gy} - S_{0Gy}$ for all three metabolic parameters for entire cell.

indicator, that the cell is undergoing a battle against these reactive species. This however seems to be concluded at around 24 hours and some over-reaction might have taken place after 24 h, either due to damage to the cell or other pathways that are too complex to deduce here. Strong changes in bound life-time compared to the other parameters have also been observed by Sharick et al. [175], but was found to be dependent on the pathway of the glucose carbon and the changes in the activity of enzymes. They therefore concluded that a distinction between glycolysis or oxidative phosphorylation based on the here used metabolic parameters is not possible without a knowledge of the metabolic pathways. In addition, different behaviours are often observed in different cell lines so that a comparison to literature is not straightforward.

Although the findings here are statistically significant, some questions regarding errors remain. The cells within one image showed nearly the same behavior. The variance between the samples was quite big and as only 2-3 samples per parameter set were investigated. In the future, observing smaller sample sizes but more samples might be beneficial. Additionally as the cells needed to be prepared beforehand and needed to be fixed before being transported all cells observed were killed, it was not possible to check the change of metabolism of the cells continuously. This might be achieved in the future, by using the microscopy setup built after the detectors are upgraded to fast FLIM detection units.

Bibliography

1. Baltuška, A. *et al.* Attosecond control of electronic processes by intense light fields. *Nature* **421,** 611–615 (2003).
2. Ammosov MV Delone, N. & Krainov, V. Tunnel ionization of complex atoms and of atomics ions in an alternating electromagnetic field. *Soviet Physics JETP* **74,** 1191 (1987).
3. Steinleitner, P. *et al.* Direct observation of ultrafast exciton formation in a monolayer of WSe_2. *Nano Lett.* **17,** 1455–1460 (2017).
4. Huber, R., Brodschelm, A., Tauser, F. & Leitenstorfer, A. Generation and field-resolved detection of femtosecond electromagnetic pulses tunable up to 41 THz. *Appl. Phys. Lett.* **76,** 3191–3193 (2000).
5. Keiber, S. *et al.* Electro-optic sampling of near-infrared waveforms. *Nature Phot.* **10,** 159–162 (2016).
6. Krausz, F. & Ivanov, M. Attosecond physics. *Reviews of Modern Physics* **81,** 163–234 (2009).
7. Uiberacker, M. *et al.* Attosecond real-time observation of electron tunnelling in atoms. *Nature* **446,** 627–632 (Apr. 2007).
8. Pupeza, I. *et al.* Field-resolved infrared spectroscopy of biological systems. *Nature* **577,** 52–59. ISSN: 1476-4687 (2020).
9. Kim, K. W. *et al.* Ultrafast transient generation of spin-density-wave order in the normal state of BaFe2As2 driven by coherent lattice vibrations. *Nature Materials* **11,** 497–501. ISSN: 1476-4660 (2012).
10. Poellmann, C. *et al.* Resonant internal quantum transitions and femtosecond radiative decay of excitons in monolayer WSe2. *Nature Materials* **14,** 889–893. ISSN: 1476-4660 (2015).
11. Kracht, D. *et al.* Innovative Laser Sources Operating Around 2m. *Physics Procedia* **83,** 1184–1195. ISSN: 1875-3892 (2016).
12. Pires, H., Baudisch, M., Sanchez, D., Hemmer, M. & Biegert, J. Ultrashort pulse generation in the mid-IR. *Progress in Quantum Electronics* **43,** 1–30. ISSN: 0079-6727 (2015).

13. Fattahi, H. *et al.* Third-generation femtosecond technology. *Optica* **1,** 45–63 (2014).

14. Tian, K., He, L., Yang, X. & Liang, H. Mid-Infrared Few-Cycle Pulse Generation and Amplification. *Photonics* **8,** 290. ISSN: 2304-6732 (2021).

15. Homann, C. *Optical parametric processes to the extreme: From new insights in first principles to tunability over more than 4 octaves* PhD thesis (LMU, 2012).

16. Homann, C., Bradler, M., Förster, M., Hommelhoff, P. & Riedle, E. Carrier-envelope phase stable sub-two-cycle pulses tunable around 1.8um at 100 kHz. *Optics Letters* **37,** 1673–1675 (2012).

17. Russbueldt, P. *et al.* 400 W Yb:YAG Innoslab fs-amplifier. *Optics Express* **17,** 12230–12245 (2009).

18. Müller, M. *et al.* 1 kW 1 mJ eight-channel ultrafast fiber laser. *Optics Letters* **41,** 3439–3442 (2016).

19. Metzger, T. *et al.* High-repetition-rate picosecond pump laser based on a Yb:YAG disk amplifier for optical parametric amplification. *Optics Letters* **34,** 2123–2125 (2009).

20. Armstrong, J. A., Bloembergen, N., Ducuing, J. & Pershan, P. S. Interactions between Light Waves in a Nonlinear Dielectric. *Phys. Rev.* **127,** 1918–1939 (6 Sept. 1962).

21. Cerullo, G., De Silvestri, S. & Manzoni, C. in *Encyclopedia of Modern Optics (Second Edition)* (eds Guenther, B. D. & Steel, D. G.) Second Edition, 290–301 (Elsevier, Oxford, 2018). ISBN: 978-0-12-814982-9.

22. Stegeman George I.and Stegeman, R. A. *Nonlinear Optics* (Wiley, 2012).

23. Boyd, R. *Nonlinear Optics, 3rd Edition* (Academic Press, 2008).

24. Pupeikis, J. *et al.* Water window soft x-ray source enabled by a 25W few-cycle 2.2 µm OPCPA at 100kHz. *Optica* **7,** 168–171 (2020).

25. Shestaev, E. *et al.* High-power ytterbium-doped fiber laser delivering few-cycle, carrier-envelope phase-stable 100 uJ pulses at 100 kHz. *Optics Letters* **45,** 97–100 (2020).

26. Dudley, J. M., Genty, G. & Coen, S. Supercontinuum generation in photonic crystal fiber. *Reviews of Modern Physics* **78,** 1135–1184 (2006).

27. Zhu, X., Zhang, X., Peng, J., Chen, X. & Li, J. Photonic crystal fibers for supercontinuum generation. *Frontiers of Optoelectronics in China* **4,** 415–419. ISSN: 1674-4594 (2011).

28. Gonzalo, I. B., Vestergaard, T. & Bang, O. *All-Fiber-Based All-Normal Dispersion Supercontinuum Source Using a Femtosecond Fiber Laser with Hollow-Core Fiber Pulse Compression* in *Advanced Photonics 2018 (BGPP, IPR, NP, NOMA, Sensors, Networks, SPPCom, SOF)* (Optica Publishing Group), NpTh2I.3.

29. Mei, C. & Steinmeyer, G. Space-time focusing and coherence properties of supercontinua in multipass cells. *Physical Review Research* **3,** 013259 (2021).
30. Weitenberg, J. *et al.* Multi-pass-cell-based nonlinear pulse compression to 115 fs at 7.5 uJ pulse energy and 300 W average power. *Optics Express* **25,** 20502–20510 (2017).
31. Budriūnas, R., Stanislauskas, T. & Varanavičius, A. Passively CEP-stabilized frontend for few cycle terawatt OPCPA system. *Journal of Optics* **17,** 094008. ISSN: 2040-8978 2040-8986 (2015).
32. Budriūnas, R. *et al.* 53 W average power CEP-stabilized OPCPA system delivering 5.5 TW few cycle pulses at 1 kHz repetition rate. *Optics Express* **25,** 5797–5806 (2017).
33. Kretschmar, M. *et al.* Thin-disk laser-pumped OPCPA system delivering 4.4 TW few-cycle pulses. *Optics Express* **28,** 34574–34585 (2020).
34. Rossi, G. M. *et al.* Sub-cycle millijoule-level parametric waveform synthesizer for attosecond science. *Nature Photonics* **14,** 629–635. ISSN: 1749-4893 (2020).
35. Schmidt, B. E. *et al.* Frequency domain optical parametric amplification. *Nature Communications* **5,** 3643. ISSN: 2041-1723 (2014).
36. Bradler, M., Homann, C. & Riedle, E. Broadband difference frequency mixing between visible and near-infrared pulses for few-cycle pulse generation with stable carrier-envelope phase. *Applied Physics B* **113,** 19–25. ISSN: 1432-0649 (2013).
37. Calendron, A.-L., Çankaya, H., Cirmi, G. & Kärtner, F. X. White-light generation with sub-ps pulses. *Optics Express* **23,** 13866–13879 (2015).
38. Ishii, N., Maruyama, M., Nagashima, K., Ochi, Y. & Itakura, R. Generation and compression of an intense infrared white light continuum in YAG irradiated by picosecond pulses. *Opt. Express* **29,** 17069–17076 (May 2021).
39. Galinis, J. *et al.* Filamentation and supercontinuum generation in solid-state dielectric media with picosecond laser pulses. *Phys. Rev. A* **92,** 033857 (3 Sept. 2015).
40. Bradler, M., Kasmi, L., Baum, P. & Riedle, E. *Pushing the NOPA to New Frontiers: Output to below 400 nm, MHz Operation and ps Pump Duration* in *19th International Conference on Ultrafast Phenomena* (Optical Society of America, 2014), 08.Tue.D.4.
41. Thiré, N. *et al.* Highly stable, 15 W, few-cycle, 65 mrad CEP-noise mid-IR OPCPA for statistical physics. *Opt. Express* **26,** 26907–26915 (Oct. 2018).
42. Fattahi, H. *et al.* Near-PHz-bandwidth, phase-stable continua generated from a Yb:YAG thin-disk amplifier. *Optics Express* **24,** 24337–24346 (2016).
43. Kolesik, M., Katona, G., Moloney, J. V. & Wright, E. M. Theory and simulation of supercontinuum generation in transparent bulk media. *Applied Physics B* **77,** 185–195. ISSN: 1432-0649 (2003).

44. Lee Rodgers, J. & Nicewander, W. A. Thirteen Ways to Look at the Correlation Coefficient. *The American Statistician* **42,** 59–66. ISSN: 0003-1305 (1988).

45. Neuhaus, M. *et al.* 10 W CEP-stable few-cycle source at 2 μm with 100 kHz repetition rate. *Opt. Exp.* **26,** 16074–16085 (June 2018).

46. Fuest, H. *High repetition rate, phase-stable, infrared OPCPA for strong-field experiments* PhD thesis (LMU, 2017).

47. Neuhaus, M. *Generation of passively CEP stable pulses at high repetition rates for strong field photoionization* 2016.

48. Liu, Y. *et al.* Fiber-amplifier-pumped, 1-MHz, 1-uJ, 2.1-um, femtosecond OPA with chirped-pulse DFG front-end. *Opt. Express* **27,** 9144–9154 (Mar. 2019).

49. Bigler, N. *et al. High-Average-Power Few-Cycle Pulses at 2.5 m* in *Laser Congress 2018 (ASSL)* (Optical Society of America), AW4A.7.

50. Chevreuil, P.-A. *et al.* Water-window high harmonic generation with 0.8-µm and 2.2-µm OPCPAs at 100 kHz. *Opt. Express* **29,** 32996–33008 (Oct. 2021).

51. Feng, T. *et al.* 27 W 2.1 µm OPCPA system for coherent soft X-ray generation operating at 10 kHz. *Optics Express* **28,** 8724–8733 (2020).

52. Mero, M., Noack, F., Bach, F., Petrov, V. & Vrakking, M. J. J. High-average-power, 50-fs parametric amplifier front-end at 1.55 um. *Opt. Express* **23,** 33157–33163 (Dec. 2015).

53. Mero, M. *et al.* 43 W, 1.55 mum and 12.5 W, 3.1 mum dual-beam, sub-10 cycle, 100 kHz optical parametric chirped pulse amplifier. *Opt Lett* **43,** 5246–5249. ISSN: 1539-4794 (Electronic) 0146-9592 (Linking) (2018).

54. Elu, U. *et al.* High average power and single-cycle pulses from a mid-IR optical parametric chirped pulse amplifier. *Optica* **4,** 1024–1029 (Sept. 2017).

55. Butler, T. P. *et al.* Watt-scale 50-MHz source of single-cycle waveform-stable pulses in the molecular fingerprint region. *Opt. Lett.* **44,** 1730–1733 (Apr. 2019).

56. Popmintchev, D. *et al.* Near- and Extended-Edge X-Ray-Absorption Fine-Structure Spectroscopy Using Ultrafast Coherent High-Order Harmonic Supercontinua. *Physical Review Letters* **120,** 093002 (2018).

57. Leshchenko, V. E. *et al.* High-power few-cycle Cr:ZnSe mid-infrared source for attosecond soft x-ray physics. *Optica* **7,** 981–988 (Aug. 2020).

58. Wang, H., Alismail, A., Barbiero, G., Ahmad, R. N. & Fattahi, H. High Energy, Sub-Cycle, Field Synthesizers. *IEEE Journal of Selected Topics in Quantum Electronics* **25,** 1–12 (2019).

59. Yakovlev, I. Stretchers and compressors for ultra-high power laser systems. *Quantum Electronics* **44,** 393 (May 2014).

60. Russbueldt, P., Mans, T., Weitenberg, J., Hoffmann, H. D. & Poprawe, R. Compact diode-pumped 1.1 kW Yb:YAG Innoslab femtosecond amplifier. *Opt. Lett.* **35,** 4169–4171 (Dec. 2010).

61. Puppin, M. *et al.* 500 kHz OPCPA delivering tunable sub-20 fs pulses with 15 W average power based on an all-ytterbium laser. *Opt. Express* **23,** 1491–1497 (Jan. 2015).

62. Silva, F., Bates, P. K., Esteban-Martin, A., Ebrahim-Zadeh, M. & Biegert, J. High-average-power, carrier-envelope phase-stable, few-cycle pulses at 2.1 μm from a collinear BiB3O6 optical parametric amplifier. *Opt. Lett.* **37,** 933–935 (Mar. 2012).

63. Lingxiong, H., Xiang, L., Ge, Z., Chenghui, H. & Yong, W. The accurate refractive indices of BIBO crystal at different temperatures. *Journal of Physics D: Applied Physics* **42,** 225109 (Nov. 2009).

64. Kato, K., Umemura, N. & Mikami, T. *Sellmeier and thermo-optic dispersion formulas for Beta-BaB[sub]2[/sub]O[sub]4[/sub] (revisited)* in *Nonlinear Frequency Generation and Conversion: Materials, Devices, and Applications IX* (ed Powers, P. E.) **7582** (SPIE, 2010), 396–401.

65. Umemura, N., Matsuda, D., Mizuno, T. & Kato, K. Sellmeier and thermo-optic dispersion formulas for the extraordinary ray of 5 % MgO-doped congruent LiNbO3 in the visible, infrared, and terahertz regions. *Appl. Opt.* **53,** 5726–5732 (Sept. 2014).

66. Trebino, R. *et al.* Measuring ultrashort laser pulses in the time-frequency domain using frequency-resolved optical gating. *Review of Scientific Instruments* **68,** 3277–3295 (1997).

67. Wnuk, P. *et al.* Discrete dispersion scanning as a simple method for broadband femtosecond pulse characterization. *Opt. Express* **24,** 18551–18558 (Aug. 2016).

68. Kakehata, M. *et al.* Single-shot measurement of carrier-envelope phase changes by spectral interferometry. *Optics Letters* **26,** 1436–1438 (2001).

69. Thai, A., Hemmer, M., Bates, P. K., Chalus, O. & Biegert, J. Sub-250-mrad, passively carrier–envelope-phase-stable mid-infrared OPCPA source at high repetition rate. *Optics Letters* **36,** 3918–3920 (2011).

70. Li, C. *et al.* Determining the phase-energy coupling coefficient in carrier-envelope phase measurements. *Optics Letters* **32,** 796–798 (2007).

71. Stanislauskas, T. *et al. Carrier-envelope phase control of Yb:KGW laser and parametric amplifiers* in *2013 Conference on Lasers Electro-Optics Europe International Quantum Electronics Conference CLEO EUROPE/IQEC* (2013), 1–1.

72. Burger, C. *et al.* Compact and flexible harmonic generator and three-color synthesizer for femtosecond coherent control and time-resolved studies. *Optics Express* **25,** 31130–31139 (2017).

73. Ueffing, M. *et al.* Direct regenerative amplification of femtosecond pulses to the multimillijoule level. *Optics Letters* **41,** 3840–3843 (2016).

74. Nubbemeyer, T. *et al.* 1 kW, 200 mJ picosecond thin-disk laser system. *Optics Letters* **42,** 1381–1384 (2017).

75. Schötz, J. *et al.* Nonadiabatic ponderomotive effects in photoemission from nanotips in intense midinfrared laser fields. *Phys. Rev. A* **97,** 013413 (1 Jan. 2018).

76. Zhang, W. *et al.* All-optical nanoscopic spatial control of molecular reaction yields on nanoparticles. *Optica* **9,** 551–560 (2022).

77. Rosenberger, P. *et al.* Imaging elliptically polarized infrared near-fields on nanoparticles by strong-field dissociation of functional surface groups. *The European Physical Journal D* **76,** 109. ISSN: 1434-6079 (2022).

78. Saleh, A. *et al.* Fifth-order nonlinear optical response of Alq3 thin films. *Results in Physics* **37,** 105513. ISSN: 2211-3797 (2022).

79. Kubullek, M. *et al.* Single-shot carrier–envelope-phase measurement in ambient air. *Optica* **7,** 35–39 (Jan. 2020).

80. Ghimire, S. *et al.* Observation of high-order harmonic generation in a bulk crystal. *Nature Physics* **7,** 138–141. ISSN: 1745-2481 (2011).

81. You, Y. S., Reis, D. A. & Ghimire, S. Anisotropic high-harmonic generation in bulk crystals. *Nature Physics* **13,** 345–349. ISSN: 1745-2481 (2017).

82. Higuchi, T., Stockman, M. I. & Hommelhoff, P. Strong-Field Perspective on High-Harmonic Radiation from Bulk Solids. *Physical Review Letters* **113,** 213901 (2014).

83. Klemke, N. *et al.* Polarization-state-resolved high-harmonic spectroscopy of solids. *Nature Communications* **10,** 1319. ISSN: 2041-1723 (2019).

84. Luu, T. T. *et al.* Extreme ultraviolet high-harmonic spectroscopy of solids. *Nature* **521,** 498–502. ISSN: 1476-4687 (2015).

85. Ghimire, S. & Reis, D. A. High-harmonic generation from solids. *Nature Physics* **15,** 10–16. ISSN: 1745-2481 (2019).

86. Luu, T. T. & Wörner, H. J. Measurement of the Berry curvature of solids using high-harmonic spectroscopy. *Nature Communications* **9,** 916. ISSN: 2041-1723 (2018).

87. Otobe, T. First-principle description for the high-harmonic generation in a diamond by intense short laser pulse. *Journal of Applied Physics* **111,** 093112. ISSN: 0021-8979 (2012).

88. Tancogne-Dejean, N., Mücke, O. D., Kärtner, F. X. & Rubio, A. Impact of the Electronic Band Structure in High-Harmonic Generation Spectra of Solids. *Physical Review Letters* **118,** 087403 (2017).

89. Kemper, A. F., Moritz, B., Freericks, J. K. & Devereaux, T. P. Theoretical description of high-order harmonic generation in solids. *New Journal of Physics* **15,** 023003. ISSN: 1367-2630 (2013).

90. Ghirmire, S. & Reis, D. High-harmonic generation from solids. *Nature Phys.* **15,** 10–16 (2019).

91. Vampa, G., McDonald, C. R., Orlando, G., Corkum, P. B. & Brabec, T. Semiclassical analysis of high harmonic generation in bulk crystals. *Physical Review B* **91,** 064302 (2015).

92. Schubert, O. *et al.* Sub-cycle control of terahertz high-harmonic generation by dynamical Bloch oscillations. *Nature Photonics* **8,** 119–123. ISSN: 1749-4893 (2014).

93. Tancogne-Dejean, N., Mücke, O. D., Kärtner, F. X. & Rubio, A. Ellipticity dependence of high-harmonic generation in solids originating from coupled intraband and interband dynamics. *Nature Communications* **8,** 745. ISSN: 2041-1723 (2017).

94. Vampa, G. *et al.* Plasmon-enhanced high-harmonic generation from silicon. *Nature Physics* **13,** 659–662. ISSN: 1745-2481 (2017).

95. Chelikowsky, J. R. & Cohen, M. L. Electronic structure of silicon. *Physical Review B* **10,** 5095–5107 (1974).

96. Neuhaus, M. *et al.* Transient field-resolved reflectometry at 50–100 THz. *Optica* **9,** 42–49 (2022).

97. Türker-Kaya, S. & Huck, C. W. A Review of Mid-Infrared and Near-Infrared Imaging: Principles, Concepts and Applications in Plant Tissue Analysis. *Molecules* **22.** ISSN: 1420-3049 (2017).

98. Pupeikis, J. *et al.* Water window soft x-ray source enabled by a 25 W few-cycle 2.2 µm OPCPA at 100 kHz. *Optica* **7,** 168–171 (Feb. 2020).

99. Guo, H. *et al.* Nanophotonic supercontinuum-based mid-infrared dual-comb spectroscopy. *Optica* **7,** 1181–1188 (Sept. 2020).

100. Aytac, Y., Mittendorff, M. & Murphy, T. E. Probing the free-carrier absorption in multi-layer black phosphorus. *Applied Physics Letters* **113,** 031108 (2018).

101. Zhong, Y., Malagari, S. D., Hamilton, T. & Wasserman, D. M. Review of mid-infrared plasmonic materials. *Journal of Nanophotonics* **9,** 1–21 (2015).

102. Cinquanta, E. *et al.* Ultrafast THz Probe of Photoinduced Polarons in Lead-Halide Perovskites. *Phys. Rev. Lett.* **122,** 166601 (16 Apr. 2019).

103. Yeh, T.-T. *et al.* Ultrafast carrier dynamics in Ge by ultra-broadband mid-infrared probe spectroscopy. *Sci. Rep.* **7,** 1–10 (2017).

104. Leitenstorfer, A., Hunsche, S., Shah, J., Nuss, M. C. & Knox, W. H. Detectors and sources for ultrabroadband electro-optic sampling: Experiment and theory. *Applied Physics Letters* **74,** 1516–1518. ISSN: 0003-6951 (1999).

105. Hwang, H. Y. *et al.* A review of non-linear terahertz spectroscopy with ultrashort tabletop-laser pulses. *J. Mod. Opt.* **62,** 1447–1479 (2015).

106. Ulbricht, R., Hendry, E., Shan, J., Heinz, T. F. & Bonn, M. Carrier dynamics in semiconductors studied with time-resolved terahertz spectroscopy. *Rev. Mod. Phys.* **83,** 543 (2011).

107. Pashkin, A., Kempa, M., Němec, H., Kadlec, F. & Kužel, P. Phase-sensitive time-domain terahertz reflection spectroscopy. *Review of Scientific Instruments* **74,** 4711–4717 (2003).

108. Huber, R. *et al.* How many-particle interactions develop after ultrafast excitation of an electron-hole plasma. *Nature* **414,** 286–289 (Nov. 2001).

109. Huber, R. *et al.* Femtosecond formation of coupled phonon-plasmon modes in InP: Ultrabroadband THz experiment and quantum kinetic theory. *Phys. Rev. Lett.* **94,** 027401 (2005).

110. Leinß, S. *et al.* Terahertz Coherent Control of Optically Dark Paraexcitons in Cu_2O. *Physical Review Letters* **101,** 246401 (2008).

111. Kübler, C. *et al.* Coherent Structural Dynamics and Electronic Correlations during an Ultrafast Insulator-to-Metal Phase Transition in VO_2. *Physical Review Letters* **99,** 116401 (2007).

112. Porer, M. *et al.* Nonadiabatic switching of a photonic band structure: Ultrastrong light-matter coupling and slow-down of light. *Physical Review B* **85,** 081302 (2012).

113. Eisele, M. *et al.* Ultrafast multi-terahertz nano-spectroscopy with sub-cycle temporal resolution. *Nature Photonics* **8,** 841–845. ISSN: 1749-4893 (2014).

114. Fischer, M. P. *et al.* Optical Activation of Germanium Plasmonic Antennas in the Mid-Infrared. *Physical Review Letters* **117,** 047401 (2016).

115. Grupp, A. *et al.* Broadly tunable ultrafast pump-probe system operating at multi-kHz repetition rate. *Journal of Optics* **20,** 014005. ISSN: 2040-8978 2040-8986 (2017).

116. Günter, G. *et al.* Sub-cycle switch-on of ultrastrong light–matter interaction. *Nature* **458,** 178–181. ISSN: 1476-4687 (2009).

117. Huber, M. A. *et al.* Ultrafast Mid-Infrared Nanoscopy of Strained Vanadium Dioxide Nanobeams. *Nano Letters* **16,** 1421–1427. ISSN: 1530-6984 (2016).

118. Huber, R., Brodschelm, A., Tauser, F. & Leitenstorfer, A. Generation and field-resolved detection of femtosecond electromagnetic pulses tunable up to 41 THz. *Applied Physics Letters* **76,** 3191–3193 (2000).

119. Kaindl, R. A., Carnahan, M. A., Hägele, D., Lövenich, R. & Chemla, D. S. Ultrafast terahertz probes of transient conducting and insulating phases in an electron–hole gas. *Nature* **423,** 734–738. ISSN: 1476-4687 (2003).

120. Lan, Y. *et al.* Ultrafast correlated charge and lattice motion in a hybrid metal halide perovskite. *Science Advances* **5,** eaaw5558 (2019).

121. Mayer, B. *et al.* Sub-cycle slicing of phase-locked and intense mid-infrared transients. *New Journal of Physics* **16,** 063033. ISSN: 1367-2630 (2014).

122. Merkl, P. *et al.* Ultrafast transition between exciton phases in van der Waals heterostructures. *Nature Materials* **18,** 691–696. ISSN: 1476-4660 (2019).

123. Merkl, P. *et al.* Twist-tailoring Coulomb correlations in van der Waals homobilayers. *Nature Communications* **11,** 2167. ISSN: 2041-1723 (2020).

124. Merkl, P. *et al.* Proximity control of interlayer exciton-phonon hybridization in van der Waals heterostructures. *Nature Communications* **12,** 1719. ISSN: 2041-1723 (2021).

125. Otto, M. R. *et al.* How optical excitation controls the structure and properties of vanadium dioxide. *Proceedings of the National Academy of Sciences* **116,** 450–455 (2019).

126. Turchinovich, D., D'Angelo, F. & Bonn, M. Femtosecond-timescale buildup of electron mobility in GaAs observed via ultrabroadband transient terahertz spectroscopy. *Applied Physics Letters* **110,** 121102 (2017).

127. Yu, T. & Lu, Y. Intervalley scattering in GaAs(111)-supported silicene. *Physical Chemistry Chemical Physics* **22,** 26402–26409. ISSN: 1463-9076 (2020).

128. Ganikhanov, F., Burr, K. C. & Tang, C. L. Ultrafast dynamics of holes in GaAs probed by two-color femtosecond spectroscopy. *Applied Physics Letters* **73,** 64–66 (1998).

129. Wong, W. P. D. *et al.* Large Polaron Self-Trapped States in Three-Dimensional Metal-Halide Perovskites. *ACS Materials Letters* **2,** 20–27 (2020).

130. Cha, S. *et al.* 1s-intraexcitonic dynamics in monolayer MoS2 probed by ultrafast mid-infrared spectroscopy. *Nature Communications* **7,** 10768. ISSN: 2041-1723 (2016).

131. Wang, Y. *et al.* Screening effect of graphite and bilayer graphene on excitons in MoSe 2 monolayer. *2D Materials* **4,** 015021. ISSN: 2053-1583 (2016).

132. Eroglu, Z. E. *et al.* Ultrafast dynamics of exciton formation and decay in two-dimensional tungsten disulfide (2D-WS2) monolayers. *Physical Chemistry Chemical Physics* **22,** 17385–17393. ISSN: 1463-9076 (2020).

133. Hsu, W.-T. *et al.* Dielectric impact on exciton binding energy and quasiparticle bandgap in monolayer WS 2 and WSe 2. *2D Materials* **6,** 025028 (Mar. 2019).

134. Chen, H. *et al.* Ultrafast formation of interlayer hot excitons in atomically thin MoS2/WS2 heterostructures. *Nature Communications* **7,** 12512. ISSN: 2041-1723 (2016).

135. Di Donato, M. & Groot, M. L. Ultrafast infrared spectroscopy in photosynthesis. *Biochimica et Biophysica Acta (BBA) - Bioenergetics* **1847,** 2–11. ISSN: 0005-2728 (2015).

136. Walker, G. C. *et al.* Time Resolution of Electronic Transitions of Photosynthetic Reaction Centers in the Infrared. *The Journal of Physical Chemistry* **98,** 5778–5783. ISSN: 0022-3654 (1994).

137. Baiz, C. R. *et al.* Vibrational Spectroscopic Map, Vibrational Spectroscopy, and Intermolecular Interaction. *Chemical Reviews* **120,** 7152–7218. ISSN: 0009-2665 (2020).

138. Lindquist, B. A., Furse, K. E. & Corcelli, S. A. Nitrile groups as vibrational probes of biomolecular structure and dynamics: an overview. *Physical Chemistry Chemical Physics* **11,** 8119–8132. ISSN: 1463-9076 (2009).

139. Xiang, B., Li, Y., Pham, C. H., Paesani, F. & Xiong, W. Ultrafast direct electron transfer at organic semiconductor and metal interfaces. *Science Advances* **3,** e1701508 (2017).

140. Bakulin, A. A. *et al.* Mode-selective vibrational modulation of charge transport in organic electronic devices. *Nature Communications* **6,** 7880. ISSN: 2041-1723 (2015).

141. De L. Kronig, R. On the Theory of Dispersion of X-Rays. *J. Opt. Soc. Am.* **12,** 547–557 (June 1926).

142. Kato, K. High-power difference-frequency generation at 5-11 µm in $AgGaS_2$. *IEEE J. Quant. El.* **20,** 698–699 (1984).

143. Zentgraf, T., Huber, R., Nielsen, N. C., Chemla, D. S. & Kaindl, R. A. Ultrabroadband 50-130 THz pulses generated via phase-matched difference frequency mixing in LiIO(3). *Opt Express* **15,** 5775–81. ISSN: 1094-4087 (Electronic) 1094-4087 (Linking) (2007).

144. Tidemand-Lichtenberg, P., Dam, J. S., Andersen, H. V., Høgstedt, L. & Pedersen, C. Mid-infrared upconversion spectroscopy. *J. Opt. Soc. Am. B* **33,** D28–D35 (Nov. 2016).

145. Yelisseyev, A. P., Isaenko, L. I. & Starikova, M. K. Optical study of defects in lithium iodate -LiIO3. *J. Opt. Soc. Am. B* **29,** 1430–1435 (June 2012).

146. Schötz, J. *Field-resolved studies of ultrafast light-matter interaction* PhD thesis (LMU, 2021).

147. Bakker, H. J., Cho, G. C., Kurz, H., Wu, Q. & Zhang, X.-C. Distortion of terahertz pulses in electro-optic sampling. *Journal of the Optical Society of America B* **15,** 1795–1801 (June 1998).

148. Beard, M. C., Turner, G. M. & Schmuttenmaer, C. A. Subpicosecond carrier dynamics in low-temperature grown GaAs as measured by time-resolved terahertz spectroscopy. *Journal of Applied Physics* **90,** 5915–5923 (2001).

149. Beard, M. C., Turner, G. M. & Schmuttenmaer, C. A. Transient photoconductivity in GaAs as measured by time-resolved terahertz spectroscopy. *Physical Review B* **62,** 15764–15777 (2000).

150. Klingshirn, C. & Haug, H. Optical properties of highly excited direct gap semiconductors. *Physics Reports* **70,** 315–398. ISSN: 0370-1573 (1981).

151. Wickenhauser, M., Burgdörfer, J., Krausz, F. & Drescher, M. Time Resolved Fano Resonances. *Phys. Rev. Lett.* **94,** 023002 (2 2005).

152. Argenti, L. *et al.* Photoionization of helium by attosecond pulses: Extraction of spectra from correlated wave functions. *Phys. Rev. A* **87,** 053405 (5 2013).

153. Gruson, V. *et al.* Attosecond dynamics through a Fano resonance: Monitoring the birth of a photoelectron. *Science* **354,** 734–738. ISSN: 0036-8075 (2016).

154. Kaldun, A. *et al.* Observing the ultrafast buildup of a Fano resonance in the time domain. *Science* **354,** 738–741. ISSN: 0036-8075 (2016).

155. Bailey, D. W. & Stanton, C. J. Calculations of femtosecond differential optical transmission in germanium. *Journal of Applied Physics* **77,** 2107–2115 (1995).

156. Dargys, A. & Kundrotas, J. *Handbook on physical properties of Ge, Si, GaAs and InP* (Science and Encyclopedia Publ., 1994).

157. Meng, F., Thomson, M. D., Sernelius, B. E., Jörger, M. & Roskos, H. G. Ultrafast dynamic conductivity and scattering rate saturation of photoexcited charge carriers in silicon investigated with a midinfrared continuum probe. *Phys. Rev. B* **91,** 075201 (7 Feb. 2015).

158. Sernelius, B. E. Intraband relaxation time in highly excited semiconductors. *Phys. Rev. B* **43,** 7136–7144 (9 Mar. 1991).

159. Bernardi, M., Vigil-Fowler, D., Ong, C. S., Neaton, J. B. & Louie, S. G. Ab initio study of hot electrons in GaAs. *Proceedings of the National Academy of Sciences* **112,** 5291–5296 (2015).

160. Terashige, T. *et al.* Temperature and carrier-density dependence of electron-hole scattering in silicon investigated by optical-pump terahertz-probe spectroscopy. *Physical Review B* **91,** 241201 (2015).

161. Floss, I. *et al.* Ab initio multiscale simulation of high-order harmonic generation in solids. *Phys. Rev. A* **97,** 011401 (1 Jan. 2018).

162. Floss, I., Lemell, C., Yabana, K. & Burgdörfer, J. Incorporating decoherence into solid-state time-dependent density functional theory. *Phys. Rev. B* **99,** 224301 (22 June 2019).

163. Nilsson, G. & Nelin, G. Phonon Dispersion Relations in Ge at 80 K. *Physical Review B* **3,** 364–369 (1971).

164. Huang, S., Heikal, A. A. & Webb, W. W. Two-Photon Fluorescence Spectroscopy and Microscopy of NAD(P)H and Flavoprotein. *Biophysical Journal* **82,** 2811–2825. ISSN: 0006-3495 (2002).

165. Camp Jr, C. H. & Cicerone, M. T. Chemically sensitive bioimaging with coherent Raman scattering. *Nature Photonics* **9,** 295–305. ISSN: 1749-4893 (2015).

166. Srivastava, A. S. *Broadband optical parametric amplifier for multimodal microscopy* 2018.

167. Wei, C.-H. *Multimodal Nonlinear Label-free Scanning Microscopy* 2020.

168. Berezin, M. Y. & Achilefu, S. Fluorescence Lifetime Measurements and Biological Imaging. *Chemical Reviews* **110,** 2641–2684. ISSN: 0009-2665 (2010).

169. Ouyang, Y., Liu, Y., Wang, Z. M., Liu, Z. & Wu, M. FLIM as a Promising Tool for Cancer Diagnosis and Treatment Monitoring. *Nano-Micro Letters* **13,** 133. ISSN: 2150-5551 (2021).

170. Shirmanova, M. *et al.* in *Multiphoton Microscopy and Fluorescence Lifetime Imaging: Applications in Biology and Medicine* (ed Karsten, K.) 189–208 (De Gruyter, 2018).

171. Koontongkaew, S. The tumor microenvironment contribution to development, growth, invasion and metastasis of head and neck squamous cell carcinomas. *Journal of Cancer* **4,** 66–83. ISSN: 1837-9664 (2013).

172. Mei, J. *Effect of radiation and co-culture with fibroblasts on growth characteristics and invasiveness of 3D breast cancer models* (2021).

173. Alhallak, K., Rebello, L., Muldoon, T. J., Quinn, K. P. & Rajaram, N. Optical redox ratio identifies metastatic potential-dependent changes in breast cancer cell metabolism. *Biomedical optics express* **7 11,** 4364–4374 (2016).

174. Xiao, W., Wang, R.-S., Handy, D. E. & Loscalzo, J. NAD(H) and NADP(H) Redox Couples and Cellular Energy Metabolism. *Antioxidants redox signaling* **28,** 251–272. ISSN: 1557-7716 1523-0864 (2018).

175. Sharick, J. T. *et al.* Protein-bound NAD(P)H Lifetime is Sensitive to Multiple Fates of Glucose Carbon. *Scientific Reports* **8,** 5456. ISSN: 2045-2322 (2018).

176. *SPCImage* `https://www.becker-hickl.com/products/spcimage/`. Accessed: 2022-06-28.

177. Blacker, T. S. *et al.* Separating NADH and NADPH fluorescence in live cells and tissues using FLIM. *Nature Communications* **5,** 3936. ISSN: 2041-1723 (2014).

178. Blacker, T. S., Berecz, T., Duchen, M. R. & Szabadkai, G. Assessment of Cellular Redox State Using NAD(P)H Fluorescence Intensity and Lifetime. *Bio-protocol* **7,** e2105. ISSN: 2331-8325 (2017).

179. Mailloux, R. J., Lemire, J. & Appanna, V. D. Metabolic networks to combat oxidative stress in Pseudomonas fluorescens. *Antonie van Leeuwenhoek* **99,** 433–442. ISSN: 1572-9699 (2011).

Acknowledgements

First of all, I would like to thank Matthias Kling for his supervision and guidance, his continued patience and trust in me. I thank Ferenc Krausz for providing the lab space and hosting me within the Laboratory of Attosecond Physics.

I owe much gratitude to Pawel Wnuk, who taught me from his deep fountain of knowledge. I am grateful for his patient teaching and his great supervision. I also thank Harald Fuest, who taught me the basics of OPCPA development and helped me with the first steps along this Journey.

I especially thank Johannes Schötz, who among other thinks helped very much with the reflectometry setup, measurements and interpretation. His deep understanding and cheerful work style was a great help during many challenging hours. I thank Jia Mei for helping with the microscopy experiments and for providing the cells used in them.

I would like to thank the colleagues with whom I had the pleasure of working closely together with: Maximilian Seeger, Philipp Rosenberger, Sambit Mitra, Shubadeep Biswas, Ritika Dagar, Zilong Wang, Weiwei Liu, Wenbin Zhang just to name a few. I am thankful for all their unique knowledge, from which I could learn much, their trust in me and their help on many occasions. Among them are also students I had the pleasure of supervising: Anchit Srivatava, Mario Aulich, Chi-Hsun Wei, Lina Hedewig and Dominik Kammerer. Their curiosity led me to deeper understand many topics. I thank them for their valuable help and the opportunity to grow together.

For his valuable aid with technical questions, moving labs and many other challenges I would like to thank the LMU technicians, especially Florian Saran, for his invaluable help and advice.

I also like to thank all the other colleagues of the group of Matthias Kling as well as from the wider chair of Ferenc Krausz. They not only provided a friendly and productive work environment, but also helped with advice, gladly lent equipment, had time for many fruitful discussions, and always had an open ear. I am thankful for the many joyful hours we shared together not just at work, but afterwards as well.

I especially have to thank Tobias Meyer and his team at the chair of Jürgen Popp at the IPHT in Jena who provided us with the microscopy setup and helped operating it. They not just graciously hosted us but also provided a great working atmosphere.

I am grateful to my parents, who have always supported me and raised me into the person I am today. I also thank all my many friends who helped take my mind off work and kept me grounded over these years.